# RESEARCH

# Mechanistic Modeling of Unbound Granular Materials

**LRRB**
LOCAL
**ROAD RESEARCH**
BOARD

Take the steps...

Research...Knowledge...Innovative Solutions!

**Transportation Research**

# Technical Report Documentation Page

| 1. Report No.<br>MN/RC 2009-21 | 2. | 3. Recipients Accession No. | |
|---|---|---|---|
| 4. Title and Subtitle<br>Mechanistic Modeling of Unbound Granular Materials | | 5. Report Date<br>June, 2009 | |
| | | 6. | |
| 7. Author(s)<br>Bereket Yohannes, Kimberly Hill, and Lev Khazanovich | | 8. Performing Organization Report No. | |
| 9. Performing Organization Name and Address<br>Department of Civil Engineering<br>University of Minnesota<br>500 Pillsbury Drive S.E.<br>Minneapolis, Minnesota 55455 | | 10. Project/Task/Work Unit No. | |
| | | 11. Contract (C) or Grant (G) No.<br>(c) 89261    (wo) 8 | |
| 12. Sponsoring Organization Name and Address<br>Minnesota Department of Transportation<br>395 John Ireland Boulevard Mail Stop 330<br>St. Paul, Minnesota 55155 | | 13. Type of Report and Period Covered<br>Final Report | |
| | | 14. Sponsoring Agency Code | |
| 15. Supplementary Notes<br>http://www.lrrb.org/PDF/200921.pdf | | | |

16. Abstract (Limit: 250 words)

Several tests are used for characterizing unbound granular materials for pavement applications. The California Bearing Ratio (CBR), resilient modulus (MR), Dynamic Cone Penetrometer (DCP) tests are three of the most common tests used for this purpose. The objective of this research is twofold. The first is to develop numerical models for these three tests. The second is to investigate relationship between basic material properties, boundary conditions, and test results, ultimately, to develop a physics-based correlation between these tests. A 3-D discrete element method (DEM) based model is adapted to simulate these tests. Good agreement is observed between the results of the simulations and sample numerical and experimental studies on granular materials. The DEM code is used to determine effects of aggregate shape, coefficient of friction, gradation, stiffness and other details on test results. The model is also used to investigate statistics of inter-particle interaction between the granular particles.

| 17. Document Analysis/Descriptors<br>Discrete Element Method, Dynamic Cone Penetrometer, Resilient Modulus, California Bearing Ratio, Mechanistic Pavement Design, Granular Material | | 18. Availability Statement<br>No restrictions. Document available from: National Technical Information Services, Springfield, Virginia  22161 | |
|---|---|---|---|
| 19. Security Class (this report)<br>Unclassified | 20. Security Class (this page)<br>Unclassified | 21. No. of Pages<br>109 | 22. Price |

# Mechanistic Modeling of Unbound Granular Materials

## Final Report

*Prepared by*

Bereket Yohannes
Kimberly Hill
Lev Khazanovich

Department of Civil Engineering
University of Minnesota

## June 2009

# Acknowledgements

# Table of Contents

**Appendix A:  User's Manual**

**Appendix B:  Modeling Unsaturated Granular Materials**

**Appendix C:  List of Symbols**

# List of Tables

# List of Figures

# Executive Summary

Several tests are used for the characterization of unbound granular materials for pavement applications. The California Bearing Ratio (CBR) test and the resilient modulus (MR) test have been two of the most common tests for laboratory characterization of mechanistic properties of unbound materials. The Dynamic Cone Penetrometer (DCP) test is a more common test for *in-situ* quality assessment and quality control of the unbound materials. There are a number of empirical correlations between the results of these tests. However, as results from different tests depend on different factors, it would be helpful to have a reliable, repeatable and well-defined mechanistic method for correlating test results. The objective of this study is to develop numerical models that can be used to investigate relationships between basic material properties and boundary conditions which, ultimately, can be used to develop a mechanistic based correlation between different types of granular materials tests.

To develop a mechanistic based correlation between tests, understanding the details of particle interaction in the granular ensemble is essential. A 3-D discrete element method (DEM) based model is used to simulate the MR, the CBR, and the DCP tests. The DEM is preferred to other methods because of its capacity to track detailed interaction between individual particles in a granular material. This method is primarily used to investigate the effect of basic physical properties of granular particles on test results.

The code is capable of accounting for aggregate shape, coefficient of friction, gradation, stiffness and other properties. Good agreement was observed between the results of the simulations and previous numerical and experimental studies on granular materials. It was found that the penetration depth of the DCP is highly affected by the shape of the particles, while the MR test is affected by the stiffness of the particle and the applied stresses. The model was also used to investigate the inter-particle interaction in the granular material. It was found that granular materials respond differently when subjected to different loading conditions from these tests.

Overall, the code shows promise for development of mechanistic-based correlations between test results and perhaps a more comprehensive mechanistic understanding of the test results. These results are presented, along with some limitations of the current model and the challenges for the future.

# Chapter 1
# Introduction

The pavement foundation that lies beneath the flexible or rigid paved surface is component of the entire structure. The aggregate base transmits heavy traffic load from the surface layer to subgrade, and its design is crucial to the performance of the pavement. A common practice is to make it from unbound aggregates. The design includes the choice of granular material and the required thickness and level of compaction of the base layer [1]. The design should ensure strong and economical layers. Strong implies that the distresses do not occur due to the traffic load. Economical implies that the minimum cost is incurred during transporting, placing and compacting the granular materials.

Good design requires detailed understanding of the behavior of granular materials. To design pavements, the granular materials that are used in the base should be characterized using tests designed to measure the material response during loading. To ensure a well engineered pavement, a designer should know what a particular test result implies about mechanical properties that determine the performance of the granular material.

There are many interesting scientific questions associated with these tests, primarily involved with understanding how the granular materials respond to specific types of stresses. Specific questions involve how granular materials resist deformation due to uniform pressure and how they deform under different shearing stresses. A careful analysis of physical tests for granular materials is necessary for understanding the subsequent behavior of granular materials; however, this is not sufficient. One also needs information from within the bulk of a granular system. Granular materials are opaque which makes visual analysis difficult, and currently there is no physical way of obtaining detailed local stress within a fully 3-D system. Computer models provide complementary information for these physical tests. With computer models a detailed qualitative and quantitative analysis of the mechanics of unbound materials tests can be performed.

The objectives of this research are three-fold: The first objective is to modify a computer code to model some of the common tests that are used to characterize granular materials. The second objective is to compare the results with existing laboratory and field data and calibrate the simulation to best represent real results. The third objective is to use the calibrated simulation to determine the physical similarities between results from commonly used tests of granular materials in pavement design. Towards this, the simulation will be used to find a mechanistic relationship between particle material properties and behavior of the bulk materials when materials are subjected to different types of loading specific to these tests.

This chapter serves as an introduction to the problem of modeling granular materials for pavement design and provides background specific to models used for unbound materials. To begin, the problem is placed in the context of a document entitled "The Mechanistic Empirical Pavement Design Guide," which includes a set of procedures aimed toward describing best

practice for pavement design. The design guidelines include interpretation of different tests for characterizing granular materials that are used in the aggregate base layer. The Design Guide and its relevance for the research described in this report are briefly discussed in the next section.

## 1.1 Practical Need: The Mechanistic Empirical Pavement Design Guide

Almost every civil engineering design for public works is based on a set of design procedures and regulations. The need for these procedures is especially apparent in issues associated with pavement design. Several design guidelines have been developed through out the history of pavement design. These include guidelines by the American Association of State Transport and Highway Officials (AASHTO) (AASHTO 1972 [2], AASTHO 1986 [3], AASHTO 1993 [4]). Historically, the practice and design recommendations have been empirically based. In other words, they have been based largely on experience rather than mechanistic principles.

Recently, there has been an effort to increase the use and application of mechanistic principles into the pavement design. This is particularly apparent in the most recent pavement design guideline: the Mechanistic Empirical Pavement Design Guide (MEPDG). Part of MEPDG provides guidelines for the design of base layer [5].

The MEPDG requires the provision of resilient moduli for all unbound layers and subgrade for each design period. First and foremost, the MEPDG recommends the use of the resilient moduli of material in the pavement design. As will be detailed shortly, the resilient moduli may be obtained directly through measurement in the laboratory, or estimating them through the use of correlations with other material properties and other tests results, or estimating them based on soil classification. Several testing procedures are available for this purpose. The next section details some of the most common tests for unbound granular material. As will be discussed in this report, different tests are used in different circumstances and there is a need in the pavement community for reliable correlations between the tests.

## 1.2 Tests for Characterization of Unbound Granular Materials

Several tests and techniques have been used to characterize unbound materials that are used in the base and subgrade layers. The coarse-grained granular materials can be characterized by their physical properties - by using the size distribution and moisture content of the granular materials, the associated bearing capacity or stiffness can be estimated. This is the fastest and the easiest way to characterize unbound materials. However, this is not reliable, as the particle size and the moisture content alone are not sufficient to describe the mechanical properties of the granular materials. To measure the mechanical properties of the granular materials some tests are required. Historically, tests have included laboratory tests where a specimen is carefully prepared and tested under very controlled conditions. The tests have also included *in-situ* tests where the actual characteristic of the granular material is measured in the field.

The MEPDG offers an option to use different approaches for determining the stiffness of granular materials for appropriate pavement design. These include the resilient modulus test, the

2

California bearing ratio test and the dynamic cone penetrometer. The details of these tests are presented in the following sub-sections.

### 1.2.1  California Bearing Ratio Test

The California Bearing Ratio (CBR) test is a laboratory penetration test used for the evaluation of base layer strength of roads and pavements. The CBR was developed in the 1950's by the California Department of Transportation, and since then it has been used extensively for pavement design purposes. Originally it was intended to characterize granular aggregates with sizes ranging between 4.75 mm and 20 mm. More recently it has been used for of soil materials. It is still one of the most popular tests used by the military, especially for design of air fields [6].

This test is described in the American Society of Testing Materials (ASTM) Standard D1883-07 [7]. The main components of this equipment are the cylindrical steel container and the plunger (Figure 1.1). The container has a diameter of 150 mm and height of 175 mm. A granular materials specimen is placed into the cylindrical container and then compacted to the desired level. The 50 mm diameter plunger is pushed up to the depth of 15 mm through the sample at a constant speed of 1mm/min. The resisting force is measured for every 0.5 mm penetration of the plunger. A gauge measures the amount of the applied stress that is required to push the plunger at a constant speed.
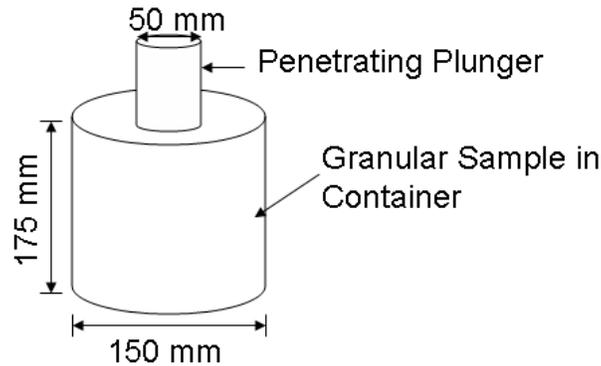


**Figure 1.1:**  Schematics of CBR.  The container has a diameter of 150 mm and height of 175 mm.  The plunger which has a diameter of 50 mm penetrates at a constant rate of 1mm/min.

To determine the bearing capacity of the sample, the measured resisting force is compared to a 'standard load'. The standard load is the resisting force of a well graded crushed rock. The resisting force of a granular sample is expressed as a ratio of the measured load and the standard load. Specifically, the CBR(%) is defined as

$$CBR(\%) = \frac{Measured\,Load}{Standard\,Load} \times 100\%$$

(1.1)

3

In other words, a CBR(%) of 100% means that the aggregate has equivalent bearing capacity as the standard crushed rock. The standard loads for a well graded crushed rock are shown in Table 1.1. The standard load increases with depth of penetration.

**Table 1.1:** Standard load for CBR test. The table shows the force that is measured in the CBR test for well graded crushed rock. The standard load is given for different penetration depths of the plunger. The penetration depths are given in mm and standard load is given in kN.

| Penetration (mm) | Standard Load (kN) |
|---|---|
| 2.5 | 13.44 |
| 5.0 | 20.16 |
| 7.5 | 25.80 |
| 10.0 | 31.20 |
| 12.5 | 35.32 |

Usually, a single CBR value is reported, specifically the CBR (%) at penetration depth of 2.5 mm. Sometimes the CBR (%) at 5.0 mm is reported if it is greater than the CBR (%) at 2.5 mm. For well graded gravel with a less than 50% content of fine particles less than size 4.75 mm the CBR (%) may range between 40 – 80 %. For poorly graded gravel with more than 50% content of fine particles the CBR(%) can be between 20-40%.

The CBR test does not represent the actual dynamic loading from traffic load on the base layer. With the development of modern and better tests for characterization of unbound materials, the popularity of the CBR test is diminishing [6]. However, many of the design guidelines and procedures, such as the MEPDG, still include the CBR results as one of the input options for obtaining an estimate of the resilient modulus of a material. Some variations of the CBR tests have been developed through time. One such example is the field CBR test, where the CBR is used to measure the bearing capacity of base aggregate on site [8]. Another recent development on the CBR is introduction of cyclic loading of the plunger, instead of a constant speed of 1 mm/min.

*1.2.2   Triaxial Resilient Modulus Test*

The triaxial resilient modulus test, or more commonly, the resilient modulus (MR) test, is used to measure the 'bulk' modulus of elasticity of unbound materials when that material is subjected to cyclic loading. The triaxial cyclic loading test, referred throughout the rest of this document as either the resilient modulus test or MR test, is the most widely used test for determination of the resilient modulus of unbound pavement materials. The 1986 AASHTO [3] design guide introduced the use of MR for characterization of base and subgrade materials.

The procedures for the MR test are described in AASHTO T307 and NCHRP 1-28A [9, 10]. The MR test apparatus consists of pressure chamber, a cylindrical container with flexible rubber

lateral membrane (that resides within the pressure chamber), and a loading cap. Figure 1.2 shows the schematics of the triaxial test apparatus. In the MR test a granular material sample fills the cylindrical chamber and is subjected to a three dimensional confining pressure and a cyclic application of deviator stress in the axial direction.

Before performing the test the granular material is put inside a cylindrical container that has a flexible side membrane and compacted to a desired level. The standard sample size for granular materials is 150x300 mm. A smaller sample size of 100x200 mm can be used for fine soils. The rule of thumb for selecting the size is that the maximum particle size should not exceed one-fifth of the sample diameter [10]. The top and bottom surfaces of the container are covered by a porous stone plate. This container is placed inside the pressure chamber and uniform triaxial confining pressure is applied. Usually air is used to apply the confining pressure. Then a cyclic deviator stress is applied in the axial direction through the loading cap. The deviator stress is applied at a rate of one application per second. Every application of deviator stress involves a loading and unloading phase followed by a rest period. Each loading and unloading phase lasts for 0.05 seconds each followed by 0.9 seconds of rest period, where no deviator load is applied. In laboratory cyclic triaxial tests the loading and unloading follows haversine ($\sin^2(\theta/2)$) impulse (Figure 1.3(a)). Figure 1.3(b) shows a typical stress-strain curve during application of deviator stress. The granular material deforms during loading phase of the deviator stress and some of the strain is recovered during the unloading phase. This recovered strain in usually referred as resilient strain.
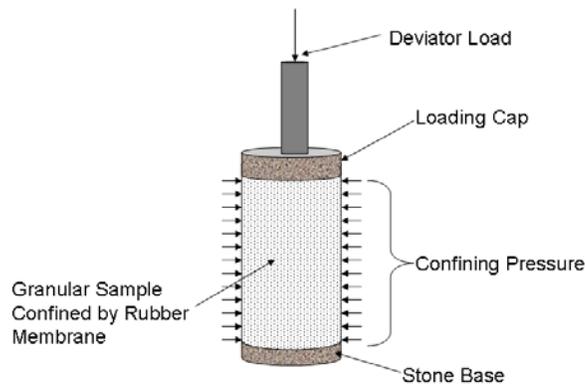


**Figure 1.2:** Schematics of MR test apparatus. The granular material is confined in a cylindrical rubber membrane. The rubber membrane has a diameter of 150 mm and height of 300 mm. The specimen is covered by stone plates at the top and bottom. The confining pressure is applied in all directions. The deviator stress is applied in the axial direction through the loading cap.

(a)　　　　　　　　　　　　　(b)
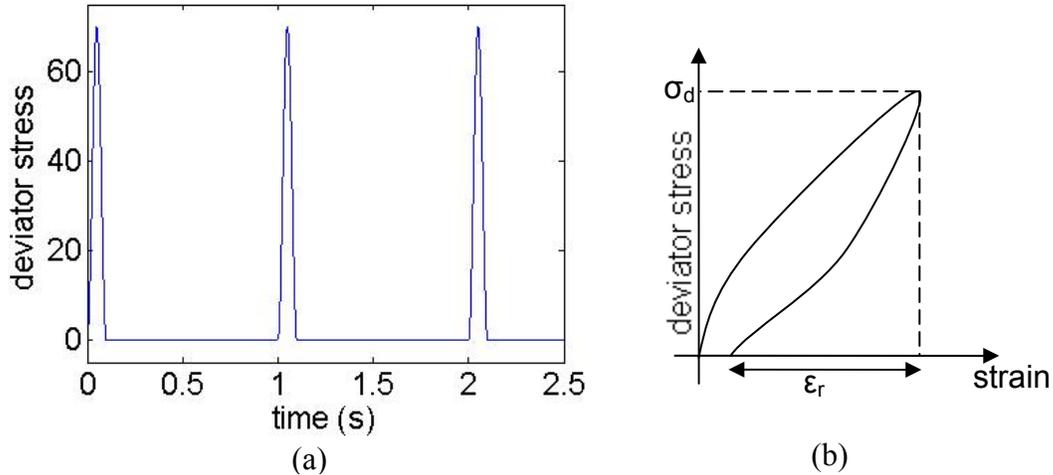
**Figure 1.3:** Application of cyclic deviator stress. (a) The cyclic deviator stress is applied at intervals of 1 s: 0.05 s loading, 0.05 s unloading and 0.9 s rest period. The loading and unloading impulse follows a haversine function. (b) The figure shows typical stress-strain curve. During loading the specimen deforms and during unloading some of the strain is recovered.

The resilient modulus of the specimen is calculated for every application of deviator load. The resilient modulus (MR) is defined as the ratio of the deviator stress and the resilient strain:

$$MR = \frac{\sigma_d}{\varepsilon_r}$$

(1.2)

where $\sigma_d$ is the deviator stress (maximum stress applied as indicated in Figure 1.3(b)) and $\varepsilon_r$ is the recovered or resilient strain (the strain recovered during the unloading period of the deviator stress, as indicated in Figure 1.3(b)). The experiment is terminated when the resilient modulus approaches a constant value after, typically, a few hundreds of cyclic application of deviator stress. At this point, the resilient modulus is calculated using the last 5 cycles.

The MR test is a well controlled laboratory test, and as such, test results are consistent from test to test. However this test is expensive and very difficult to perform which can discourage its use for every project design. In addition, the sample preparation and the test procedure are time consuming. Finally, it is not necessarily true that the specimen preparation for the laboratory test will produce the same material state as the material in the field. In other words, some way of measuring the material properties in the field and relating those field test results would be helpful, preferably with some consideration placed into their preparation methods in the field.

### 1.2.3 Dynamic Cone Penetrometer Test

The Dynamic Cone Penetrometer (DCP) is an *in-situ* test used to estimate the bearing capacity of granular materials. It was developed in the mid 1950's in response to a need for a simple and rapid method to characterize granular material. It is primarily used to characterize the granular

aggregates that are used in the base layer of an asphalt pavement. It is a fast and inexpensive way of investigating strength of granular materials [11]. There are different specifications for the DCP apparatus. This report discusses the DCP apparatus as specified by Minnesota Department of Transportation (Mn/DOT) [12].

The details of the DCP test are described in ASTM D6951-03 [13]. The DCP is a manually operated apparatus. The main components of the DCP are the cone at the tip, hammer, and anvil (Figure 1.4). The cone has a base diameter of 20 mm and apex angle of 60°. The cone needs to be tough; it is usually made from usually made tempered steel. This allows the DCP to penetrate through granular materials easily. The hammer weighs 8kg and the total mass of the DCP is 13 kg. The 8 kg hammer is raised and dropped (free fall) from a height of 0.575 mm onto the anvil. The measure of the strength of the soil is reported in terms of the amount of penetration per blow, also called the Dynamic Penetrometer Index (DPI). Usually a reading meter is attached to the apparatus to determine the amount of penetration for each blow. The lower rod is 1 m long. Therefore, penetration data can be collected up to depth of 1m.
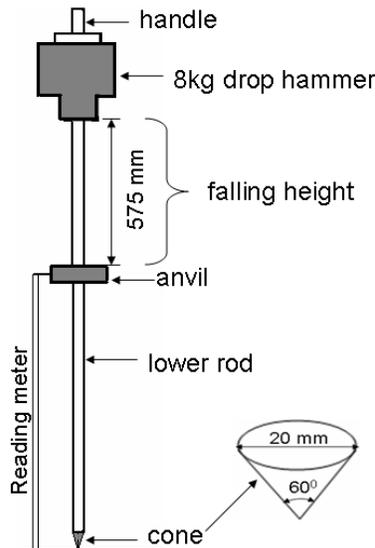


**Figure 1.4:** Schematics of DCP apparatus. The schematics show the DCP according to the specification of the Mn/DOT. The hammer weighs 8 kg and is dropped on the anvil from height of 575 m. The cone has apex angle of 60°. The lower rod has length of 1 mm.

The DCP test requires great care for proper implementation and interpretation of the test results. When taking measurements, the penetration during placement of the DCP on the granular material due to its weight should not be included in the DPI. Usually, the penetration depth for the first three hammer drops is also not considered in the DPI. This is standard procedure which is intended to avoid measurements at the top granular material. The top part is usually disturbed and not a good representative of the true characteristics of the granular material. The operator must make sure that the DCP is penetrating perpendicular to the ground. Otherwise, a higher resistance to penetration – therefore high shear strength - may be assumed. After the DCP test the area close to the DCP might get disturbed and loose.  Therefore, it is recommended that the

7

DCP test locations should be at least 60 mm apart from each other. According to some standards the operator must wait at least for 1 second between consecutive hammer drops. This ensures that DPI is recorded for every hammer drop and the DCP has come to rest.

This test is a rapid and economical way of assessing the in-situ bearing capacity. It can be also be used to assess the thickness and sequence of underlying granular material. The DCP is capable of penetrating asphalt concrete and base coarse materials, though it is not recommended to use DCP to penetrate asphalt.

Table 1.2 shows results from DCP test conducted by Ford and Eliason [14]. The test was performed on open graded granular material for subsurface drainage trench. The penetration depths (in mm) for granular material with different level of compaction during placement and first hammer drop are shown. The DCP penetrated to the bottom of the trench during placement for the specimen where no compaction applied. It penetrated to the full depth for the poorly compacted specimen during the first hammer drop. The penetration depth for the well compacted granular material was 100 mm during the first hammer drop.

**Table 1.2:** Sample penetrations for DCP. The table shows penetration depths from a DCP test during placement and hammer drop from experiments conducted by Ford and Eliason [14]. The penetrations depths are given in mm. The test was conducted on granular materials, which have different compaction levels. The granular materials have a $D_{50} = 1.2$ mm and $D_{90} = 5$ mm. The trench has a depth of 300 mm.

| Trench Depth (mm) | DCP Test | No Comp | Poorly Comp | Well Comp |
|---|---|---|---|---|
| 300 | Placement | 300 | 50 | 60 |
|  | 1st Drop | - | 300 | 100 |
| 600 | Placement | 600 | 50 | 60 |
|  | 1st Drop | - | 600 | 100 |
| 900 | Placement | 900 | 75 | 75 |
|  | 1st Drop | - | 900 | 110 |

## 1.3 Relationship between Tests

As discussed in the previous section, there are several advantages and disadvantages for each test. To summarize some of the advantages: The DCP is simple and inexpensive field test. It is the fast way of investigating the granular material's bearing capacity and the stratification of the underlying layers. The CBR test is very simple test and many straight forward design standards are readily available. The MR test provides a better mechanistic interpretation of granular material characteristics under dynamic loading. Each testing procedure also has some disadvantages or drawbacks. There is no clear mechanistic interpretation of the DCP and CBR tests that relate them to the actual dynamic loading in the base layers. The CBR test is more of a

static load test than a dynamic one. Though the MR test is a better representative of the periodic loading scenario due to traffic loading, it is very expensive and time consuming experiment. Further, it is not necessarily a good representation of the field conditions. However, given that the results are relatively reproducible; this may be the best test for characterizing material properties in their ideal state for pavement applications. The choice of method to characterize granular aggregates depends on these factors.

The MEPDG recommends the use of MR values as a primary input. However, MR test results might not be always available. In this case, the design guide allows input from other tests, such as the CBR and DCP test, and converts the results into 'equivalent' MR values. However, correlations between the tests are not unique. Several researchers have attempted to come up with the correlations. All the correlation developed up to now are based on experimental results and all are empirical. Some of the widely used correlations are shown below.

The following empirical relationship developed by Heukelom and Klomp [15] is used in the 1993 AASHTO Guide.

$$MR(psi) = 1500(CBR(\%))$$ (1.3)

This equation usually works for materials where the CBR (%) value is less than 10%. Another empirical relationship that is widely used to interpret CBR(%) values to MR is the one developed by Powell et al [16]

$$MR(psi) = 2555(CBR(\%))^{0.64}$$ (1.4)

This equation was found to work well for CBR (%) ranging between 2% and 12%.

There are also empirical equations that correlate test results from the CBR and DCP tests. One that is developed by the Corps of Engineers [17] and widely used is

$$CBR(\%) = \frac{292}{DPI\_avg^{1.12}}$$ (1.5a)

$$CBR(\%) = \frac{1}{(0.017019 * DPI\_avg)^2}$$ (1.5b)

where DPI_avg is the average dynamic cone penetrometer index in mm/blow and CBR is the in percent. Equation 1.5a is used for CBR values greater than 10% and equation 1.5b is used for CBR values less than 10%. Liveneh [18] also developed another correlation between the DCP and CBR test results.

$$\log(CBR(\%)) = 2.20 - 0.71(\log(DPI\_avg))^{1.5}$$ (1.6)

9

They have observed that this relationship applies for wide range of fine and coarse granular material.

The difference in these equations suggests that there is no clear link or correlation between test results. In addition, some researchers were not able to find any correlation between these tests [19]. It is also important to note that correlations developed for one type of soil are not necessarily applicable for other types of soils. The MEPDG encourages development of locally calibrated models to convert average DPI to CBR or to MR. This calls for extensive research in the area of modeling unbound granular materials. This task is urgent and very important for efficient implementation of the MEPDG design guide. Towards this, this report describes a method for modeling the tests of unbound materials. The next section provides some background including previous attempts for modeling unbound materials.

## 1.4    Modeling Techniques

The correlations described in the previous section indicate that there is an opportunity to improve interpretation of the tests for pavement unbound materials through the use of modeling techniques. A mechanistic physics-based understanding of the test results may help in development of reliable correlations between tests. Two families of numerical methods that are commonly used for modeling of unbound granular materials are discussed briefly in the next subsections.

### 1.4.1   Continuum Numerical Methods

Continuum numerical methods consider the granular material as a continuum medium occupying the entire volume. These methods do not model individual grains. An example of one of these methods includes the finite element method.

The finite element method has been used to analyze different geomechanics problems and tests of unbound granular materials. Sukumaran et al [20] used finite element method to determine the resilient modulus of granular materials from CBR test.   This model demonstrated that the prediction by Heukelom and Klomp (Equation 1.3) overestimates the resilient modulus of granular soil. Kim and Siddik [21] used the finite element method to model the MR test. They showed that results from the model are similar to physical experiments. These two finite element based models were carried out using the commercial software ABAQUS [22]. Limits in the finite element method for modeling granular materials behavior include the inability of this method to take into account variable particle gradation and also the empirical manner in which bulk material properties are determined.  The Distinct Element Method described in the next section offers a method for determining bulk material properties directly from individual particle interactions.

### 1.4.2   Distinct Element Method

Another way of modeling the soil or granular particles is the distinct element method (also known as the discrete element method, or DEM). This method treats individual particles

separately. Due to the discrete and heterogeneous nature of granular materials, the DEM provides a more direct link to true granular behavior. Since the macroscopic behavior depends on the microscopic interaction of particles, this method is more relevant than the continuum method. In this method the bulk properties may be obtained rather than input. DEM methods model inter-particle interactions (based on basic physical properties of the particles) and from these obtain the bulk properties. It has special advantage over other methods for modeling behavior of granular materials under a sudden impact or instantaneous large displacements as in the DCP test.

## 1.5 Distinct Element Method (DEM) Modeling of Subgrade Tests

The DEM was first proposed by Cundall and Strack [23]. The first model was used to study the interaction between granular rock particles when they subjected to stresses. This model was a 2-D model that used circular disks to represent rock particles. Qualitative comparison of the test observations with experimental studies showed that the DEM can be used as a tool to investigate detailed interaction between particles. Since then models based on the DEM have been applied in various fields of soil and rock mechanics, granular flow and powder mechanics.

The DEM has also been used to model several soil characterization tests. These models include a variety of penetration tests. Most of the penetration models were performed for quasi-static penetration of a plunger or a cone. Quasi-static penetration tests are tests where a cone or plunger is pushed through a specimen at a constant speed, as in the CBR test. Most of the DEM analysis focused on simulation of the resistance during penetration of the plunger or cone.

Tanka et al [24] used a 2-D DEM to model bar penetrometer test. Bar penetrometer test is a test where a rod that has a conical tip is pushed through a soil sample at a constant rate. As in the case of the CBR test, the resistance to penetration is measured as the rod penetrates. They compared the simulation results with physical experiments on soil. The resistance increased with the depth of penetration of the cone for both the simulation and the experiment. However, while the resisting force in the physical experiments increased smoothly and continuously, it force showed some fluctuations in the DEM simulation. The magnitude of the resisting force measured from DEM simulation was much less than that of the physical experiments. Tanka et al. also conducted physical experiments on specimen comprising spherical steel 'balls'. The resisting force from this experiment showed similar fluctuation as that of the simulations. But the magnitude of the resisting force was much higher than the simulation results. Other static penetrometer simulations include models by Ke and Bray [25] and Jiang and Yu [26]. Thomas et al used what they call 'Discontinuous Deformation Analysis' (DDA), which is a slight variation of the DEM. Jiang and Yu assumed that the geometry of the problem is symmetrical in radial direction from the DCP and considered only half of the ground and half of the penetrometer in the analysis. Both studies showed the DEM is capable of representing real physical experiments qualitatively.

The triaxial compression test is by far the most modeled test using the DEM. This is a very common test used to determine the shear strength of soils in foundation design and other types of problems that involve quasi-static loading. The triaxial compression test is similar to the resilient

modulus test, except that in the triaxial compression test the axial deviator stress is increased until the specimen fails. The specimen is considered failed if the specimen continues to deform without further increase in the deviator stress. In DEM simulations, the application of axial deviator stress can be strain controlled or stress controlled. In strain controlled systems the upper platen is pushed at a very low constant speed, while in the stress controlled systems the load at the upper platen is gradually increased.

These DEM models have used different approaches to model the physical properties of particles [27, 28] and the boundary conditions, such as the confining pressure and the flexible rubber membrane [29, 30, 31, 32]. The details of some of these models are described in Chapter Three of this report. Most of these DEM models were used to study the effect of physical properties of individual particles on the bulk behavior of the specimen. Ullidtz [33] have used biaxial DEM models that incorporate the cohesive behavior of soils. Tensile stress was applied in the soil by decreasing the axial load continuously. This model was able to capture the tensile cracks that are commonly observed in cohesive soils.

Zeghal [34] used a 2-D DEM to model the resilient modulus test. His model was capable of predicting that the resilient modulus of granular materials increases with both the deviator stress and confining pressure. The MR increased more with the confining pressure than it did with the deviator stress. Similar trends have been observed in early physical experiments by Hicks and Monismith [35]. Another report by Khogali and Zeghal [36] concluded that the predicted resilient modulus from the simulations is within 10% of the actual laboratory tests. Compared to other DEM models the error margin looks very small [24, 31].

Most of the DEM models discussed above are 2-D models. The particles are assumed to be cylindrical rods or circular disks, which do not represent well real life situations. This restricts the motion of particles such that they are restricted to translate only in a 2-D plane and rotate only about one axis. These models are used mainly for their simplicity, less computation time and computer memory size requirements. Detailed comparison between these simulations and actual experimental cannot be made as 2-D models give over-stiff behaviors. They can only be used to for a limited qualitative analysis of few applications [31].

In this report, the possibility of simulation of unbound materials tests using a fully 3-D model is investigated. A 3-D DEM code [37, 38] is adapted for the specific boundary condition of the CBR, MR and DCP. The DEM method is described in detail in Chapter 2. This includes step by step description of the DEM models and the basic physics used to determine the interaction force between particles and the displacement of particles. Then the feasibility of using DEM for the CBR, MR and DCP test is examined, in terms of computational requirements associated with each test. Detailed test results and their implication on the existing norms and observation are presented in Chapters 3 and 4. The computational results are compared with physical test results for granular materials and adapted for maximum applicability as described in Chapters 3 and 4. Finally, the relationships between the three tests are examined in detail for certain particle properties as discussed in Chapter 5. Chapter 6 summarizes and includes some challenges and limitations of numerical models and future plans.

# Chapter 2
## Distinct Element Method for Modeling of Tests of Unbound Material

The Distinct Element Method (DEM) (also know as Discrete Element Method) offers a rigorous flexible framework to develop mechanistic models of tests of unbound granular materials. As detailed subsequently, the method is almost akin to a physical experiment performed on a computer. Each element is treated distinctly throughout the simulation. Forces between elements are based on realistic physical models validated through physical experiments. Then the displacement and rotation of all elements are calculated from the Newton's and Euler's law of motion. While use of the DEM is computationally time intensive, it mimics analogous physical experiments almost perfectly for modeling granular materials. The output from DEM simulations provides details that are not accessible through experiments.

While physical experiments are a necessary component of research on physical systems, there are many physical details that experiments cannot provide. For example, in physical experiments it almost impossible to detect the kinematics of individual particles, unless the particles are at the surface. There are some methods for measuring properties of particles covered by other particles such as Nuclear Magnetic Resonance Imaging (MRI) [39] but they are expensive and are often limited in terms of sample size and type of material. It is also nearly impossible to measure all details of the forces between particles in physical experiments. As will be described in Chapter 5, photoelastic disks provide some information but to this point it is limited to qualitative details, except in strictly 2-D systems. Force sensors provide another alternative, but they are generally limited to reporting forces in one direction and over a specific surface region. Finally, it is not easy to vary one material property at a time in physical experiments; particle properties-based investigation depends on the type of available granular particles.

In contrast, as will be described shortly, DEM modeling provides many details that are not attainable through experiments. As DEM tracks individual particles, it can provide information on position, velocity, displacement and rotation of each particle, regardless of its position in the granular material. DEM modeling also provides information about the contact forces between particles as well as the contact forces between particles and walls throughout an entire simulation. DEM modeling allows for complete flexibility of variation of physical parameters such as size and density of particles; further, these individual physical properties can be varied independently from other parameters to investigate the impact of varying each parameter on the behavior of the system. This provides efficient way of investigating the relationship between particular physical properties of the particles and response of the bulk granular materials to various forms of forcing and excitations. Finally, DEM modeling also provides a method for determining internal energy and various forms of energy dissipation, though this last tool is not used for the work in this report.

A 3-D DEM code was adapted to model the CBR, MR and DCP tests. The code was written by Zhang and Hill [37]. The code was originally used to study different types of granular flows,

13

such as granular flow inside a rotating drum. The code simulated spherical particles only. The code was validated by comparing the results from simulation and physical experiments in a rotating drum. For the research described in this report, some modifications were made in the existing code in order to develop a mechanistic modeling of CBR, MR and DCP tests. First, the contact algorithm was improved and, ultimately, these improvements were incorporated into the code used to generate the results reported in [37]. Second, new subroutines were written to adapt the code for the different boundary conditions that are associated with each of the CBR, MR and DCP tests. Third, new subroutines were written to account for different particle shapes.

This Chapter will provide some background on the 'basic' DEM formulation and the details of the modifications made to adapt the code for mechanistically modeling the tests of unbound materials. Finally, for some of the tests, the code was parallelized so that it could run on several computers at the same time. This will be described in section 2.3.

## 2.1    Background

Modeling granular materials using the DEM method was first proposed by Cundall and Strack in 1979 [23]. The DEM method is in many ways similar to Molecular Dynamics (MD), first introduced in the 1950's [40]. In the latter case, MD is used for simulating interaction between molecules. Atoms and molecules are tracked individually in MD simulations and are made to interact via molecular forces. The resulting force on each molecule due to all external forces such as those exerted by other molecules is calculated, and this resulting force is used to determine the acceleration of each molecule. The velocities and displacements are then calculated using numerical integration.

DEM and MD simulations are similar but have few key differences. In DEM simulation, in contrast to MD simulation, individual macroscopic particles rather than molecules are treated as distinct objects; in other words, the interaction between two particles is modeled as a single force (rather than a sum of all the molecular forces associated with atoms and molecules composing each particle). Additionally, in DEM simulation of macroscopic dry granular systems, only particles in direct contact with one another interact, while in MD simulations, forces such as van der Waals are significant and act at a distance. Finally, unlike the MD simulation which does not consider the rotation of molecules, particle rotation is typically included in the DEM simulation and is considered significant for modeling the dynamics of granular materials.

Based on how the interaction between two particles is treated, the DEM can be classified into two broad categories: a hard sphere model and a soft sphere model [41]. The hard sphere model assumes that the particles are rigid. The force and response of particles, during collision between particles, is dictated only by the exchange of momentum. The soft sphere model, takes into consideration the deformation that occurs over time during collision of particles. The soft sphere model reflects the reality during collision better than the hard sphere model. While this detail is not always important for relatively sparse granular materials where interparticle interactions are relatively rare and typically binary, the details of interparticle interaction are of critical importance for dense granular systems where typically multiple particles are in contact for an

extended period of time. Therefore, the DEM model for this research is based on the soft sphere model as described subsequently.

In the soft sphere DEM model when two particles come into contact, their deformations are modeled with an effective *overlap* between the particles (Figure 2.1). In other words, the two particles would deform during a real collision – in DEM the deformation is modeled by allowing the particles overlap with one another and by keeping track of that overlap. The force exerted on the particles is estimated based on the effective deformation or overlap of each particle in contact. Figure 2.1 depicts the basic principle of DEM in a 2-D coordinate system. Figure 2.1(a) shows two circular particles, particle$_1$ and particle$_2$, approaching each other at a velocity of $V_1$ and $V_2$. The particles also have a rotational speeds $\omega_1$ and $\omega_2$. Figure 2.1(b) illustrates the interaction model of the two particles shows the overlap of the two particles during collision. The resulting interparticle force is dependent on the magnitude and rate change of this overlap. If the particles are rotating relative to one another or even if the particles are not rotating but their centers are not moving directly toward one another (as in Figure 2.1 (a)), there is an effective tangential deformation (tangential overlap) as well. This may be thought of as a relative movement of the contact points between the particles (both points at the origin of the axes in Figure 2.1(b) before impending rotation).



(a)                                                           (b)
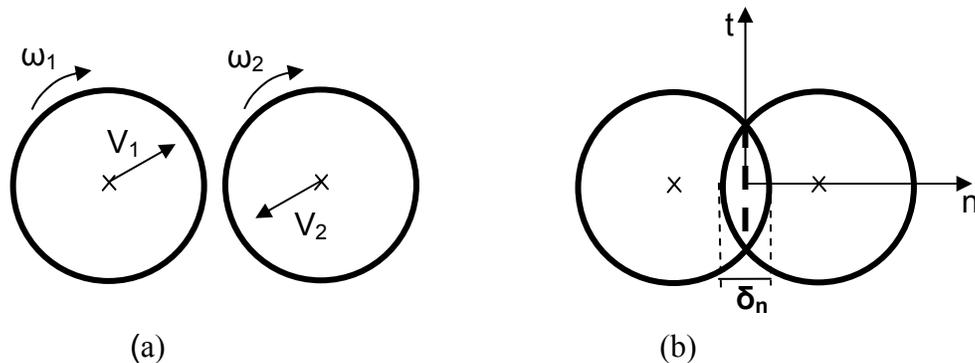
**Figure 2.1:** Illustration of the interaction of two particles in a soft sphere 2-D DEM model. (a) Two particles, particle 1 and particle 2, approach each other at a velocity of $V_1$ and $V_2$. The particles can also have a rotational speed of $\omega_1$ and $\omega_2$. (b) During collision the particles the deformation is represented by the normal overlap ($\delta_n$) between the two circular particles. The plane of contact is assumed to be flat and perpendicular to the line joining the centers of the two particles. n is the axis perpendicular (normal) to the contact plane and t is the axis parallel (tangential) to the contact plane.

In DEM model, the plane of interaction or plane of contact is defined as a plane that is perpendicular to the line that connects the centers of the two spherical particles whose location is a distance from each particle center of the radius of that particle minus $\delta_n/2$.

In terms of the plane of contact, the contact force on the two particles can be resolved into two components: the component normal to the plane (the *normal force*) and a component tangential

to the plane in the direction of relative movement of contact points (the *tangential force*). The general form of the force between the interacting particles can be described as,

$$\vec{F} = \vec{F}_n + \vec{F}_t \tag{2.1a}$$

$$\vec{F}_n = F_n \bullet \hat{e}_n \tag{2.1b}$$

$$\vec{F}_t = F_t \bullet \hat{e}_t \tag{2.1c}$$

where $\vec{F}$ is the total force on the particles, $\vec{F}_n$ and $\vec{F}_t$ are the normal and tangential components of the force, $\hat{e}_n$ and $\hat{e}_t$ are unit vectors in the normal and tangential directions respectively. $F_n$ represents the magnitude of the normal component of the force. $F_t$ is the magnitude of the tangential component of the force which acts parallel to the plane of contact.

The soft sphere model described above encompasses a class of models where the normal and tangential forces exerted by one particle on another are considered based on the effective deformation or overlap in the normal and tangential directions. There are several sub-categories where the details of this model differ. In the simplest form, the contact force between particles is modeled as a linear function of some measure of the particle stiffness and the amount of overlap [34]. The normal force is a linear function of the particle stiffness and the amount of overlap in the normal direction. The tangential force is the smaller of two calculated values: (1) a linear function of the particle stiffness and the overlap in the tangential direction (2) the product of the coefficient of material friction and the interparticle normal force. In other words, for small values, as is true for the normal force, the tangential force is modeled as linearly proportional to the tangential overlap with the maximum tangential force limited to the friction force. If the ratio of the interparticle tangential force and the interparticle normal force exceeds the coefficient of contact friction, the two particles start sliding relative to each. For this simple soft sphere model, friction is the only way that the energy is dissipated from the system. Slightly more complicated versions of what one might call this "elastic collision" model include an elastic contact interaction – no damping term – but the dependence on deformation of overlap between particles is some power other than one [31, 42].

Other models have described the contact forces in each direction based on two parts: one that is restorative, like a spring, dependent only on the amount of deformation or overlap, and the other, like a damping mechanism, that is dependent on the rate change of deformation or overlap. For these models, the damping part is also a way in which energy is dissipated from the system. The forms of the elastic part of the normal and tangential force components are similar to those of the simpler force models described in the previous paragraph; they are dependent on some measure of particle stiffness and overlap in the relevant direction, and the dependences are not necessarily linear. The damping part of the normal force component is generally modeled using the rate of change of the overlap in the normal direction, some damping constant dependent on measured particle behavior, and the overlap in the normal direction. Similarly, the damping part of the tangential force is some function of a measured damping factor, the rate of change of the overlap in the tangential direction. As described earlier, the maximum tangential force is limited by the

16

friction coefficient multiplied by the normal force. In these models the energy is dissipated due to both the damping factors in the forces and the contact frictions.

In general, the components of the contact force are given by

$$F_n = k_n \delta_n^a + \gamma_n \delta_n^b \dot{\delta}_n^c \qquad (2.2a)$$

$$F_t = \min \begin{cases} |k_t \delta_n^d \delta_t^e + \gamma_t \delta_n^f \dot{\delta}_t^g| \\ |\mu F_n| \end{cases} \qquad (2.2b)$$

Here $F_n$ and $F_t$ represent the normal and tangential components of the forces as previously described. $k_n$ and $k_t$ are the stiffness factors of particles, $\delta_n$ and $\delta_t$ are the overlaps between particles and $\gamma_n$ and $\gamma_t$ are the damping factors. The subscripts n and t indicate normal components and tangential components of each parameter respectively. $\dot{\delta}_n$ is the rate of overlap in the normal direction and $\dot{\delta}_t$ is the rate of tangential overlap. $\mu$ is the coefficient of friction between the interacting particles. a, b, c, d, e, f and g are parameters of the force model.

The force model in Equation 2.2 can be linear or nonlinear depending upon the coefficients a, b, c, d, e and f. If the components of the force have only the linear elastic part (function of only particle stiffness and overlap) a and e will be equal to 1 and b, c, d, f and g will be equal to 0. A linear force model can also have a damping factor in addition to the elastic part, where b and e are equal to 1 and c and f are equal to 0 or 1 [23, 24].


## 2.2    Nonlinear Force Model

For the work described in this report, realistic forces and kinematics were needed. Therefore a nonlinear forces model where each term is modeled as realistic as possible was required. The model used here was developed based on DEM model by Tsuji et al [43]. According to this model the values of a, b, c, d, e, f and g are 3/2, ¼, 1, 1/2, 1, ¼, and 1 respectively. As detailed presently, the value of "a" is obtained from the Hertizian contact theory and d and e are obtained from the Mindlin and Deresiewicz [44] theories, while the rest of the parameters are based on measurements of the particle behaviors and empirical fits.

The stiffness factors of particles which are used in the elastic part of the components of the force, $k_n$ and $k_t$, are determined based on Hertizian contact theory for the normal force and Mindlin and Deresiewicz [44] for the tangential force. The normal stiffness factor is a function of the effective radius and effective modulus of elasticity of the particles that are in contact.

$$k_n = \frac{4}{3} \sqrt{R_{eff}} E_{eff} \qquad (2.3)$$

17

where $R_{eff}$ is the effective radius and $E_{eff}$ is the effective modulus of elasticity. The effective radius for two interacting particles, particle 1 and particle 2, is given by

$$\frac{1}{R_{eff}} = \frac{1}{R_1} + \frac{1}{R_2} \qquad (2.4)$$

where $R_1$ and $R_2$ are the radius of particle1 and particle 2 respectively.

Similarly, for particle 1 and particle 2, the effective modulus of elasticity is give as a function of the modulus elasticity and the Poisson ratio of each particle.

$$\frac{1}{E_{eff}} = \frac{1-v_1^2}{E_1} + \frac{1-v_2^2}{E_2} \qquad (2.5)$$

where $E_1$ and $E_2$ are modulus of elasticity of particle 1 and 2, and $v_1$ and $v_2$ are Poisson's ratio of particle 1 and particle 2 respectively.

The tangential stiffness factor $k_t$ is derived from Mindlin contact theory [44]. It is a function of the effective radius and the effective shear modulus of the two interacting particles.

$$k_t = 8\sqrt{R_{eff}}\, G_{eff} \qquad (2.6)$$

where $G_{eff}$ is the effective shear modulus. The effective shear modulus is function of the modulus of elasticity and Poisson's ratio of the particles.

$$\frac{1}{G_{eff}} = \frac{2(1+v_1)(2-v_1)}{E_1} + \frac{2(1+v_2)(2-v_2)}{E_2} \qquad (2.7)$$

The damping forces are necessary for realistic behavior in the dense collisional systems modeled in this report: without damping factors particles will not ever stop moving. However, there is no simple theoretical description for the damping factor. The first DEM model by Cundall and Strack assumed that damping is the function of the mass and stiffness of the particles [23]. Later, Tsuji et al [43] showed the derivation of the damping factor as a function of the mass, the stiffness and the coefficient of restitution of the particles. The coefficient of restitution is defined as the ratio of the velocity of a particle after and before collision. The maximum value of the coefficient of restitution is one: when the particle bounces back with the same velocity before contact. Very low coefficient of restitution indicates that the velocity is reduced by significant amount after collision.

One general form of the damping factor for the normal component of the force in Equation 2.2 is given as:

$$\gamma_n = \alpha\sqrt{m_{eff} k_n} \qquad (2.8)$$

18

where $k_n$ is the stiffness factor for the normal direction described by Equation 2.3, $\alpha$ is a empirical constant and depends on the assumption of the factors that affect damping. $m_{eff}$ is the effective mass that is calculated from the masses of the two interacting particles:

$$\frac{1}{m_{eff}} = \frac{1}{m_1} + \frac{1}{m_2} \qquad (2.9)$$

m1 and m2 are masses of particle 1 and particle 2.

The same form of damping factor, as shown Equation 2.2(b), is used for the damping factor in the tangential direction, though $k_t$ replaces $k_n$ in this case. The first model by Cundall and Strack [23] used a value 2 for $\alpha$. This is a relatively high value, resulting in a large reduction of the magnitude of velocity of the particles after collision, and the particles will come to a rest quickly. The model developed by Tsuji et al [43] makes use of the measured coefficient of restitution of particles to determine $\alpha$. From their measurements, they plotted an empirical graph that relates the coefficient of restitution to $\alpha$. For this model the value of $\alpha$ was set to 0.7, which is based on coefficient of restitution of marble.

### 2.2.1    *Force Model: Particle Wall Interaction*

The force model for interactions between particles and other objects (such as container boundaries or walls) is similar to the inter-particle force model described by Equation 2.2. Historically, both linear models and nonlinear models have been used to model particle-wall interactions. For this report, nonlinear particle-wall interaction was used as described by Equations 2.2-2.8. The same physical parameters of the wall material are required to calculate the coefficients as indicated previously. The dimensions of the walls are usually much larger than the particle sizes, so details such as wall mass and radius are considered infinite. Therefore, the effective radius during a particle-wall contact is considered equal to the radius of the particle (see Equation 2.4). Similarly, the mass of walls is very large compared to the mass of particles, which gives an effective mass during contact that is equal to the mass of the particle. This assumption implies that there is no wall deformation during such collisions.

Once the contact forces between all objects are obtained the movement of, usually, thousands of particles must be calculated. The steps involved to model the evolution of these large systems are described in the next section.

## 2.3    General Procedure in the Distinct Element Method

The general procedure used for modeling granular materials using DEM technique is the same for all types of systems. Figure 2.2 shows a simplified flow chart of the DEM code. The simulation starts with defining the boundary conditions such as walls and the physical properties of the particles.  Then, the particles are "initialized" that is, given initial distinct positions, usually not touching one another and given initial velocities. Then all possible contacts between distinct objects are detected to determine the interaction force between the objects. The calculation of these forces was described in the previous section. The last step in the flow chart is

to calculate the kinematics of individual objects. This section describes the details of the kinematics involved in the DEM simulation.
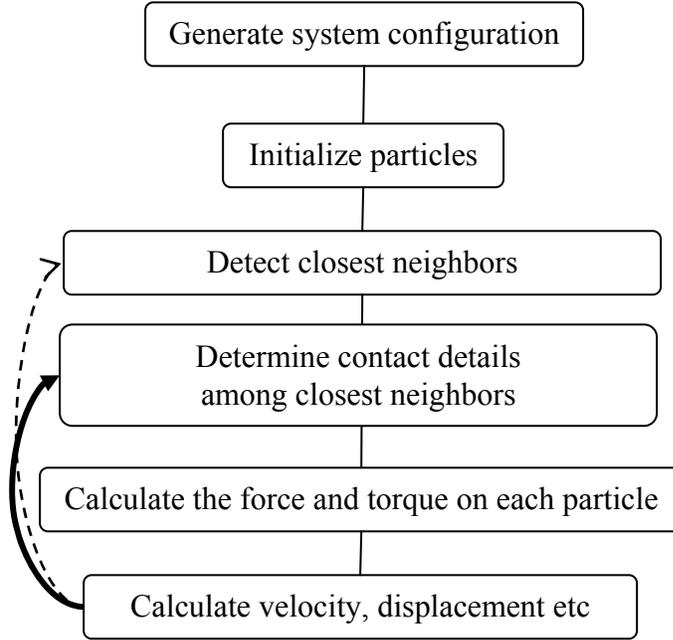


**Figure 2.2:** Flow chart for the DEM simulation. The simulation starts with generating system configuration and particle initialization. Possible contacts between particles are detected and the force between the particles is calculated based on effective overlap. Then displacement and velocity can be integrated from the acceleration of the particles. The solid arrow indicates that the explicit iteration for calculating the contact and forces. The broken line shows that nearest neighbor detection is not done for every iteration.

Once the forces between contacting particles are determined, the translational ($a$) and rotational ($\alpha$) acceleration can be calculated using Newton's and Euler's second laws. The translational acceleration of a particle is given as the quotient of the total force (normal and tangential) on the particle and the mass of the particle. The force moment on the spherical particles is determined by the sum of the tangential forces alone. The normal force doesn't affect the rotation of spherical particles as its vector passes through the center of the particle. Each tangential force from each contact produces a force moment equivalent to the product of the tangential force and the moment arm from the center of the particle (radius of the particle, R, for spherical particle). Similarly, the rotational acceleration of a particle is given by quotient of the total torque on the particle and the moment of inertia of the particle.

$$a = \Sigma F / m \qquad\qquad (2.10a)$$

$$\alpha = \tau / I \qquad\qquad (2.10b)$$

where, $\tau$ is the resultant force moment or torque and I is moment of inertia of the particles. For spherical particles the moment of inertia is given by $\frac{2}{5}mR^2$ .

### 2.3.1 Integration Scheme

The particle accelerations then can be integrated to determine the rotational and translational velocities and displacement of the particles. The kinematics of a particle is described, for each time step, as

$$\Delta v = a\Delta t \qquad (2.11a)$$
$$\Delta \omega = \alpha\Delta t \qquad (2.11b)$$
$$\Delta x = v\Delta t \qquad (2.11c)$$

where $\Delta$ indicates the change of each quantity during a time step; v is the velocity of the particle, $\omega$ is the rotation, x is the position of the particle and $\Delta t$ is the time step used in the integration. The Fourth Order Runge Kutta numerical scheme was used for the numerical integration. This scheme was preferred over other schemes because of its stability and accuracy. For central difference time integration scheme where the force is linearly proportional to the overlap and no damping is present, Munjiza have shown that the time step should be less than the maximum time step tmax [45]:

$$t_{max} = 2\sqrt{\frac{m}{k}} \qquad (2.12)$$

where $t_{max}$ is the maximum time step for stable central difference integration schemes, m is the mass of the smallest particle in the specimen and k is the normal or tangential stiffness factor, whichever is larger. For granular particles this limit is in the order of micro seconds. For many of the simulations in this research a time step of about 2.2 micro seconds was used for the integration steps.

### 2.3.2 Nearest Neighbor Algorithm

Processing contact interaction for all possible contacts would involve a total number of operations that scales as $N^2$, where N is the total number of particles. This would be computationally intensive and would limit application of the DEM to simulations of very few particles. To reduce the computational time requirements of processing contact interaction, it is helpful to eliminate couples of discrete elements or particles that are far from each other such that there is no chance that they will contact one another. This involves the use of a contact detection algorithm/nearest neighbor algorithm which can be done in different ways [45, 46]. In the computational simulations used for the research described in this report, the computational domain is divided into cells of the same size and the centers of the particles are mapped onto the cells based on their location. The size of the cells is determined such that the largest particle in the specimen fits into a single cell. This ensures that two particles can interact only if they lie in the same cell or adjacent cells. Therefore to search for particles that are interacting with a

particle it is enough to check those particles that are mapped to the same cell or adjacent cells. In 3-D space a cell can have up to 26 neighboring/adjacent cells. The neighbor list for every particle is built using these cells and these groups of cells. As the particles move, new contacts might be created and previous contacts might be lost. Therefore, the neighbor list must be updated repeatedly during the simulation. The frequency of updating is selected based on the relative displacement of particles. Simulations with highly flowing particles require more frequent updating than quasi-static systems. The dashed arrow in the flow chart [Figure 2.2] indicates that updating the neighbor list does not occur for every time step; this would be an unnecessary waste of computational time.

### 2.3.3 *Other Computational Issues*

Computational efficiency is one of the main challenges in DEM models. Compared to other types of modeling techniques the DEM requires more computation time. This is because the DEM tracks the displacement and interaction of every individual particle. The required computation time depends primarily on the number of particles. In bigger systems the simulations may involve hundreds of thousands of particles. The number of particles in this research was limited to less than 10,000 particles.

Another factor that affects the computation time is the efficiency of neighbor list reading. There are different algorithms that are used for different systems. The direct mapping technique, which is implemented in the DEM code for this research, works well for mono-sized samples or narrow range of size of particles.

The computational time also depends on the type of test. The boundary conditions, rate of deformation or speed of penetration and loading configurations are all major factors that contribute to the required computation time. As will be discussed, the simulations performed for the DCP tests described in this report take the least amount of time. For the DCP test, the primary factor that determines the computational time is the number of particles. More particles are used in the DCP than the other two tests described in this report, but the high speed penetration of the DCP makes it fast simulation. The DCP test, the placement and one hammer drop, as described in Chapter 1 and detailed more in Chapter 4, last only for around 0.4 or 0.5 seconds in real time. The simulation for a specimen comprising 5000 mono-sized particles might take about 5 hours on a personal computer Pentium IV 2.4 GHz processor. Of course, since the cost of the simulation depends primarily in the number of particles, these simulations could be quite expensive once a larger system size is tested, but for the sample sizes described here, the DCP simulations are the fastest.

The computation time requirement for the CBR simulation is slightly higher than computation time requirement for the DCP simulation. The maximum number of particles used in the CBR simulation is 3500. However, the plunger is penetrating the specimen at a very small velocity to the depth of 15 mm. Therefore, the CBR simulations described in this report takes two or three times longer time required for the DCP test simulation described in this report.

The MR test simulation is by far more computational intensive than the other tests. This is mainly due to the application of complicated boundary of the MR test. In other words, the

sample size is kept relatively small, but the complicated interactions between the particles and the hydrostatic boundary are sufficiently complex that a typical MR simulation is the most expensive of the three tests described in this report. Other complications of this test involve the long time to steady state and the requirement that the system attains steady state conditions before measurements are considered valid.

The computation time can be improved by using a parallel version of the DEM code [46]. For the purpose of the work described in this report, a parallel code using the message passing interface (MPI) was developed and tested for this research. The parallel code was tested for compacting 5000 particles of uniform size in a cylindrical container. The domain was divided into horizontal slices such that the dynamics and kinematics of the particles in each slice is computed by different processors. The ALTIX clusters at the Minnesota Supercomputing Institute were used to run this code. The simulation was repeated on the ALTIX cluster using single processor. Initial investigations showed a somewhat reduced computational time, but a completely useful parallelized code is still under development.

To this point, Chapter 2 has focused on the general formulation of DEM. As described, the general formulation was developed over the past three decades, starting with the original formulation of Cundall and Strack in 1979 [23]. Then, Zhang and Hill developed a code in Fortran to incorporate the DEM code into a form useful for simulating dense granular flow in chutes and drums. For the work described in this report, this code was modified for the particular boundary conditions and particle shapes required for tests of unbound materials. The sections that follow, 2.4-2.6, describe some modifications and additional subroutines developed specifically for this research by the author of this report.

## 2.4    Particle Shape

In reality, unlike the particles in the model described above, the particles that compromise the granular materials are, in general, aspherical. Often, for simplicity, spherical particles or circular disks are used in the DEM simulations. However, spherical or circular particles tend to roll and/or slide past other spherical or circular particles relatively easily. This difference leads to discrepancies in bulk macroscopic properties and is generally believed to cause an unphysically low stiffness in some DEM models [24, 28]. Several researchers have used different techniques to either reproduce certain details of granular materials comprised of aspherical particles or to implement asphericity into DEM models. Some of the most common techniques are described in this section.

Early solutions to the asphericity problem focused on the effect of asphericity in restricting particle rotation. In the case of aspherical particles, both the tangential and normal components of interparticle forces can provide impediments to the rotation of particles. For spherical particles, only the tangential force has a role in resisting the rotation. In light of this, some of the simpler models for aspherical particles involved artificially restricting the movement of the circular or spherical DEM particles [47]. Towards this, the rotational movement of the circular or spherical particles was inhibited and the particles were given higher shear strength. These specimens gave higher shear strength and greater stiffness. These specimens also experience less

volume change when subjected to external stresses (strong dilation). This model has also been used to investigate the effect of particle contact friction (or sometimes referred to as the microscopic friction) on specimen comprising circular or spherical particles where rotation is not prohibited. The contact friction was increased up to 0.5 (equivalent to $\tan^{-1} 26.5°$). It should be also noted that the contact friction is different from the bulk friction that is usually used to describe the shear strength of granular materials. The bulk friction (or sometimes referred to as macroscopic friction) is usually given in terms an angle that corresponds to the repose angle formed by cohesionless granular materials. On the other hand, the particle contact friction, which is used in Equation 2.2 (b), is the friction between two contacting particles. The particle contact friction is usually given in terms of dimensionless numbers. To maintain consistency, the particle contact friction is given in terms of dimensionless numbers throughout this report. Specimens with higher values of contact friction produced higher shear strength, higher initial modulus and strong dilation. However, there is some limit to the usefulness of this technique, as will be shown in Chapter 4.

More commonly, particle asphericity is directly incorporated into the DEM code by slightly changing the algorithm and force contact model described above. The most widely used aspherical particle shape for DEM simulations is an ellipse. For example, Ting et al [28] used a biaxial DEM model to study the effects of particle shape in the test results using elliptical particles of different aspect ratios. They found that the macroscopic friction angle, that is, the angle at which shear bands typically form, increases as the aspect ration of the particles is increased. This study indicated that the specimen stiffness increased with increasing aspect ratio of the elliptic particles. They also demonstrated that the orientation of particles has significant effect on the stiffness of the particles.

Other DEM models use regular polygons or slightly different polygons to generate rougher form of asphericity, such as those described in Ullditz [33]. These models mimic the real shape of particles better than the other methods described earlier. However, the singularity problem at the corners of the polygon makes this method difficult for efficient implementation into DEM models. Compared to the methods that use ellipsoid particles, the use of polygons require more computational time and the contact detection and related interactive force cannot be solved analytically. The models that use ellipsoidal particles do not have singularity problem, and the contact detection involves solving a fourth degree equation which can be done analytically. However, the DEM simulations using these elliptical particles take four to five times longer time than the time required for DEM simulations using spherical particles.

Another approach used for modeling non-spherical, irregularly shaped particles involves "computationally gluing" spherical particles together [27, 48]. In other words, aspherical computational particles are created using multiple spherical particles and fixing their positions relative to one another into a rigid-body cluster. Forces acting on any of the "mutually glued" particles affect the glued particles as a single cluster particle. Examples of the use of this technique for tests of unbound materials include those by Thomas and Bray [27] and Zeghal [48]. Thomas et al. [27] used clustered circular disks in a 2-D DEM model for a bi-axial test. Their model demonstrated that a system consisting of irregularly-shaped particles exhibits a higher global friction angle than does a system consisting of circular particles. Zeghal [48] used 2-D clustered disks in a DEM model for the resilient modulus test. He found that a granular

24

materials consisting of irregularly shaped particles resulted in a higher resilient modulus than for granular materials consisting of circular particles. Most such models created for tests of unbound materials were performed using 2-D systems which may provide qualitative trends but cannot approach good quantitative results.

For the work described in this report, 3-D aspherical particles are created by gluing spherical particles together. The force models that are derived from the Hertzian and Mindlin theories as well as Tsuji's model described above in section 2.2 [43, 44] are essentially the same for the aspherical particles created in this way. There is no force calculated between mutually clustered particles, but when a sphere in one cluster contacts a sphere in another cluster, the forces between them are calculated as if they were individual spheres. The coefficients in the force model are calculated based on the material and physical properties of each spherical particle alone, the radius, mass, etc. of an individual particle in the cluster. The primary difference between spherical and aspherical model arises from the calculation of the kinematics of the aspherical particle clusters. In this case, the forces for all particles in a cluster are calculated as one resultant force and one resultant force moment about the mass center of the cluster. In the case of aspherical particles, the center of mass and moment of inertia of each cluster particle is determined from the location of the mass centers and the masses of the spherical particles in each cluster particle in the following manner.

$$M = \sum_{1}^{n} m_i \qquad (2.13)$$

$M$ is the total mass of the cluster, $m_i$ is the mass of particle $i$ and $n$ is the total number of spherical particles in the cluster. The center of mass of a cluster, $C_m$, is determined as shown in equation 2.14.

$$C_m = \frac{1}{M} \sum_{i}^{n} m_i X_i \qquad (2.14)$$

$C_m$ is the center of mass, $m_i$ is the mass of the particle $i$ and $X_i$ represents the coordinates of the center of particle $i$. The moment of inertia, $I$, of the cluster about the center of mass in any given axis $j$ is calculated as

$$I_j = \sum_{i}^{n} (\frac{2}{5} m_i r_i^2 + m_i \Sigma (X_{ik} - C_{mk})^2) \qquad (2.15)$$

where $k$ represent the two axes that are orthogonal to the $j$ axis.

The movements of the individual particles is then determined from the position of the mass center of the clustered particle as well as its orientation.

There are several benefits to this last method of generating aspherical particles. Gluing spherical particles offers flexibility without significant additional computational cost. Any number spherical of particles with different sizes can be glued together to form a wide variety of particle shapes. (A few are illustrated in Figure 2.3). In addition, inter-particle contact detection can be performed easily, and interparticle forces can be calculated easily, both essentially the same as that performed on assemblies of spherical particles. In other words, the computational time requirement for models of aspherical particle clusters is nearly proportional to the total number of spherical particles in the system. In contrast, modeling shape using ellipsoids or polygons requires detecting intricate contacts between particles and keeping track of the orientation of individual particles, all of which require much more computational time [28].
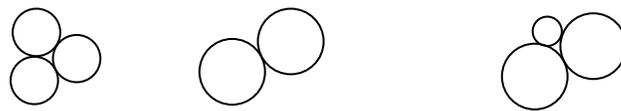


**Figure 2.3:** Gluing particles to form different particle shapes. The figure shows some ways of gluing particles together to form different shapes of particles. Any number of particles can be used to create any kind of shape of particle.


## 2.5    Generating System Configuration

Once all of the rules for the DEM simulations have been determined and the particle parameters set, a computational experiment can be performed. This section describes how the initial system configuration was developed for the tests performed for this report. The following section describes how the individual tests were setup.

### 2.5.1   Initiating System Configuration

To begin the simulations, the system must be "initiated". (This is the first step in the flow chart (Figure 2.2).) This step involves setting up the boundary wall and introducing the particles into the system for the initial configuration.

The boundaries for DEM simulations can be either periodic or fixed walls in any direction. For periodic boundaries, the particles at the edge of one side "see" the particles which are at the edge of the opposite side. Any particle that is pushed out of the system from on one side is added to the system on the opposite side. This kind of boundary is usually used to model large scale simulations where the behavior of the specimen is symmetric in a particular direction. The periodic boundary is defined parallel to the assumed plane of symmetry.

On the other hand, the boundaries could consist of predefined fixed walls. The fixed wall could have different geometries. Flat walls and cylindrical walls are the most common types of fixed

boundary walls. All the simulations reported in this report are performed for fixed boundaries. Test-specific boundary conditions will be discussed shortly.

Similar to the case of boundary walls, the geometry and physical properties of the particles need to be set prior to any simulation. Towards this, the particles are placed inside the container. For the simulations performed in this report, this was done by suspending the particles inside the boundary. Instead of suspending the particles initially at random locations in space such that no two particles are touching each other as performed in some simulations, [34], for the simulations performed in this report, particles are suspended inside the container in a hexagonal arrangement where the particles are not touching one other. Figure 2.4 shows 50 particles suspended in a rectangular container. The gradation – that is, the size distribution of the individual particles – is introduced at this point. The suspended particles are assigned a size based on the user-specified sizes and quantity of particles of each size. A random number generator distributes the different sizes of particles throughout the system.

To induce a random initial placement for these particles, the particles are given very small random initial velocities. The random initial velocity for every particle is kept below 0.04 m/s for these simulations. In the beginning the only force acting on the particles is gravity, as there is no contact between particles or between any particle and a wall. The particles will accelerate in the direction of gravity. After a while the particles start colliding with each other and the walls. For every contact between particles, the force exerted is determined using the force models discussed in the previous section. During collisions the particles lose energy and eventually reach a state of rest.
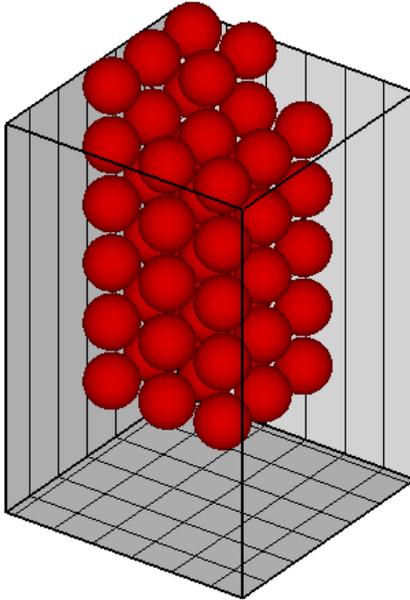
**Figure 2.4:** Suspended particles prior to drop. The figure shows 50 spherical particles suspended in a rectangular prism container. The base of the container is 150x150 mm. The size of the particles is 10 mm. The particles will be released at a very small random initial velocity.

### 2.5.2    Compact Sample

Usually, after the particles first come to rest the packing is very loose with an uneven top surface. An additional step is required to achieve denser packing and flat surface. Depending on the type of simulation compaction can be achieved via one of the two methods as described below. Method 1: The compaction is performed by applying load and at the same time adding some "computational lubrication". The load is applied by dropping a heavy weight on the top surface. The applied load depends on the amount of bulk density required and sample size. In practical experiments and construction procedures the soil is compacted to the desired level at the optimum moisture content. Since there is no moisture content in this simulation, a lubrication effect is added by reducing the coefficient of contact friction. Reduced contact friction allows particles to slide past each other very easily. The contact friction was reduced to 0.1 during compaction; the nominal value of contact friction for quartz is 0.5. Method 2: Compaction can also be done by squeezing the side walls while applying the load. The lubrication effect can also be added to this method if there is a need. This method usually gives a denser packing quickly than the first method. Most of the compactions for the simulations reported in this report were performed using the second method of compaction.

After compaction the density of the specimen is typically between 60% and 70%, similar to other previous research studies on packing of spherical particles [49]. While this is near maximum packing conditions for spherical particles, it is small compared to real well-graded materials. The difference is due largely to the absence of fine particles in the simulations which fill the gaps

28

between the 'large' granular particles. The packing achieved in the research described in this report is close to that of what is considered "open-graded" materials in real construction materials.

Though the general flow chart for the simulations of the three tests is the same, depending upon the type of test to be simulated there are some variations in technical details and type of loading configuration. The last part of this chapter discusses specific simulation details developed for this project for a relatively simple test to model, the California Bearing Ratio test.


## 2.6    California Bearing Ratio Test

The CBR test is a well controlled test where the dimensions of the container have a standard value.  Thus it works well as a basic test for calibrating the simulations for real granular materials with possible complicating factors such as aspherical and variably-sized particles.

### 2.6.1    Set-up for Computational CBR Test

The CBR model consists of a cylindrical container which is covered at the top and bottom. It has a diameter of 150 mm and height of 175 mm. The container is made of steel. The physical parameters of stainless steel are E=210 GPa, $\rho$= 7850 kg/m$^3$ and $\upsilon$=0.3.

As described in the previous section the particles are dropped from suspended positions inside the container. To achieve better packing or reduce the porosity the ensemble of particles is compacted by dropping a load on the surface of the specimen while squeezing the side wall at low contact coefficient of friction. Once the compaction has reached the desired level, the lid top cover is put in place and the simulation of the CBR can proceed.

During the CBR simulation a plunger, a narrow rod, is pushed through the lid into the granular materials.  The plunger typically has a diameter of 50 mm and is made of steel and weighs 1.6 kg. The plunger penetrates the sample at a constant speed of 1mm/min. The plunger is computationally represented by a cylindrical side wall and flat (circular) wall at the bottom. Detection of magnitude and direction of contact between a particle and the sharp edge of the plunger at the junction between the cylindrical side walls and flat circular bottom surface is not easy for computational purposes. Thus, tiny particles of diameter 2.5 mm were attached at the sharp edge of the plunger, as shown in Figure 2.5, to create a smooth and computationally easily manageable boundary. For the standard dimension of the plunger 60 tiny particles were required.

29
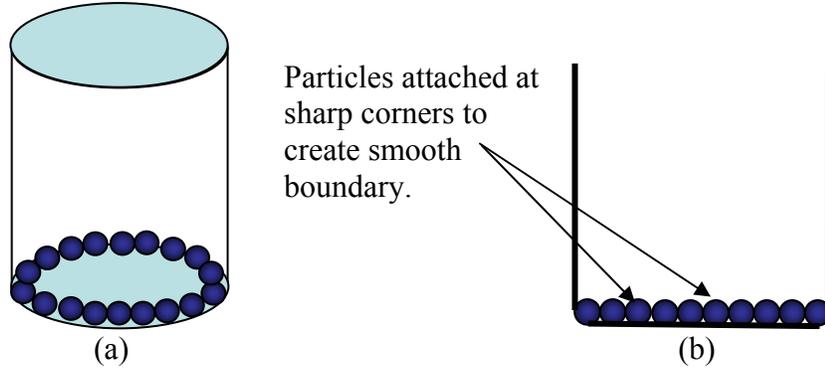
**Figure 2.5:** Schematic representation of the CBR plunger (not to scale). Spherical particles are glued at the joint of the circular wall and the cylindrical wall. a)3-D view of the plunger b) cross sectional view of the plunger.

As the plunger is pushed through the granular sample, the particles resist the motion via particle / plunger wall contact forces. As the DEM provides the magnitude of the forces for every contact, the resisting force can be determined easily: The resisting force on the plunger is the summation of all forces (normal on the bottom surface and tangential against the curved vertical surface) due to the particle-plunger contact. The resisting force is measured at frequent intervals, in this case at intervals of 0.125 mm.

Based on these, when one considers the forces between the particles and between particle and wall as described in Equation 2.2.

$$F_n = k_n \delta_n^a + \gamma_n \delta_n^b \dot{\delta}_n^c \qquad (2.2a)$$

$$F_t = \min \begin{cases} | k_t \delta_n^d \delta_t^e + \gamma_t \delta_n^f \dot{\delta}_t^g | \\ | \mu F_n | \end{cases} \qquad (2.2b)$$

Each coefficient is calculated for all possible contact between particles or particle and wall is calculated as described earlier in this chapter. The particles used have material properties similar to granite particles (where here we use particle properties reported in ref. [32] for granite: E = 29 GPa, μ= 0.5, ν = 0.15 and ρ = 2650 kg/m³) and have a diameter of 10 mm. The container wall is steel (E = 210 GPa, μ=0.3, ν =0.3 and ρ = 7850 kg/m³ [50]). Table 2.1 shows example of calculated contact coefficient for contact between two 10 mm particles and contact between 10 mm particle and steel wall.

**Table 2.1:** Contact coefficients. The table shows the normal and tangential stiffness and damping coefficients for particle-particle interaction and wall-particle interaction for the CBR test described in section 2.6. The material properties for the particles are similar to a type of granite (E = 29 GPa, $\mu$= 0.5, $\nu$ = 0.15 and $\rho$ = 2650 kg/m$^3$), and the container wall is stainless steel (E = 210 GPa, $\mu$=0.3, $\nu$ = 0.3 and $\rho$ = 7850 kg/m$^3$). The parameters shown here were calculated using Equations 2.2-2.8.

| Interaction | $K_n$ $(kg(m^{1/2}s^2)^{-1})$ | $K_t$ $(kg(m^{1/2}s^2)^{-1})$ | $\gamma_n$ $(kg\,(m^{1/4}s)^{-1})$ | $\gamma_t$ $(kg(m^{1/4}\,s)^{-1})$ |
|---|---|---|---|---|
| 10 mm & 10 mm particle | 3.07E+08 | 4.23E+08 | 3.23E+02 | 3.79E+02 |
| 10 mm & steel wall | 8.35E+08 | 1.15E+08 | 7.53E+02 | 8.83E+02 |

*2.6.2    CBR Computational Results*

Figure 2.6 shows measured resisting force vs. depth penetrated by the plunger from a DEM simulation for a specimen comprising 3500 spherical granite particles, material properties as detailed above, with a diameter of 10 mm. As typical for a physical experiment, the resistance increases as the plunger penetrates deeper. In this simulation the resistance increases as an exponential function of the penetration depth, though the details of this might vary from case to case and is not investigated further here. There is a sudden drop in the resisting force at the depth of 12.0 mm that is likely due to discrete and sudden relative particle movement. The resistance again increases continuously for the remaining depth of penetration.
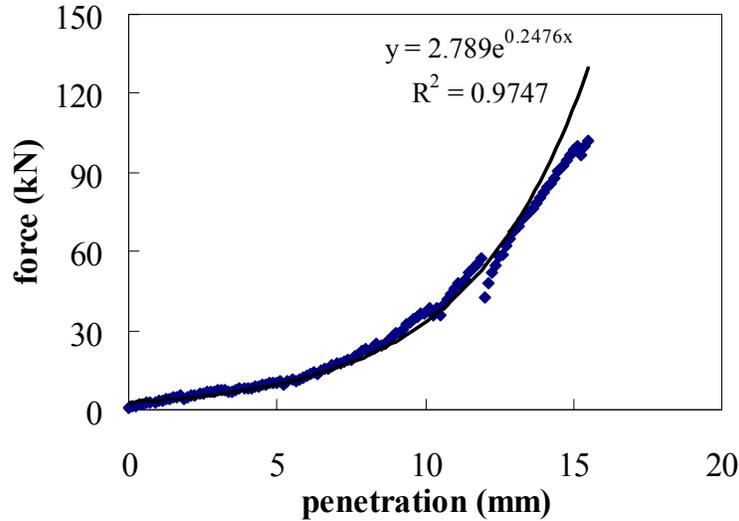
**Figure 2.6:** Resisting force vs. penetration for CBR test. The figure shows a plot of resisting force during plunger penetration in the CBR test. The force is measured at the intervals of 0.5 mm up to 15 mm. The resisting force increased continuously at as the penetration depth increased. The test is performed on specimen comprising 3500 particles with physical properties of d = 10 mm E = 29 GPa, $v$ = 0.15, $\mu$= 0.5 and $\rho$ = 2650 kg/ m3. The discrete points represent results from the code and the solid line is an exponential fit to the data.

The CBR(%) is determined as the ratio of the measured total resisting force and the standard load. The computed CBR (%) values at the penetration depths of 2.5 mm and 5 mm for the simulation of Figure 2.6 are shown in Table 2.2. The CBR(%) at the depth of 2.5 mm is slightly less than the CBR(%) at 5.0 mm. As discussed in Chapter 1, usually the CBR(%) at 2.5 mm is reported  as the CBR(%) of a given specimen.

**Table 2.2:**  CBR test results. The table shows the measured resistance force after the plunger penetrated 2.5 and 5.0 mm during a CBR test. The CBR(%) at every penetration depth is calculated as the ratio of the measured load and the standard load. This table is from the results shown in Figure 2.6.

| Depth (mm) | 2.50 | 5.00 |
|---|---|---|
| Load (kN) | 6.06 | 10.24 |
| Std. Load (kN) | 13.40 | 19.66 |
| CBR (%) | 45.26 | 52.11 |

According to soil type classification this CBR (%) value corresponds to a well graded granular material with less than 50% fine soil particles of size 4.75 mm [51]. From this baseline test, the computational DEM model appears to represent the behavior of granular bases well. Thus this system appears useful for modeling the more complex and also more common resilient modulus test and dynamic cone penetrometer test, as detailed in Chapters 3 and 4.

# Chapter 3
# Resilient Modulus Test Simulation

The resilient modulus test is considered by many researchers the most fundamentally important test for measuring certain material properties of unbound granular material [52]. It provides a direct way of measuring the bulk elastic properties of granular material, which are required by the MEPDG for pavement design. Additionally, this test is considered fairly representative of the dynamic traffic loading. That is, the range of applied stresses is intended to represent the range of traffic stresses.

As in the case of the CBR test, the MR test is also well controlled laboratory test. Unlike the CBR test, during the MR test the applied stresses are also well controlled in all directions. That is, during the CBR test, the velocity of the plunger into the granular material is controlled and a resulting force measured. During the MR test, the stress is controlled and the resulting deformation of the sample is measured. Results from this test are considered reproducible, as they are only taken after the specimen has reached an apparent steady-state value. The details of the DEM set-up for simulation of the MR test are described in this chapter along with results of simulations.`

## 3.1    Resilient Modulus Test DEM Set-up

The initial procedures for the simulation of MR test are similar to those of the CBR simulation. First, the dimensions and the physical parameters of the walls are defined. Both in real tests and in the computational simulations the top and lower "walls" of the container are made of stone and the cylindrical wall of the container is a flexible rubber membrane. However, during the sample preparation process, the material properties for the cylindrical side wall are those of steel as described above (E = 210 GPa, $\mu$=0.3, $\nu$ =0.3 and $\rho$ = 7850 kg/m$^3$). After the boundaries are defined the particles are suspended, dropped, and then compacted as described in Chapter 2.

Once the particles come to rest, properties of the side wall are changed from those of rigid steel to those of rubber with additional hydrostatic pressure considerations to more accurately represent the conditions of the resilient modulus test. This is not particularly straightforward, so before describing how this was achieved for the research described in this report, it is useful to consider how other researchers have modeled this flexible membrane subjected to hydrostatic pressure.

To develop the MR model for the work described in this report, several models for the rubber membrane were considered and tested. Many are similar to those described in literature for the triaxial compression test and resilient modulus test. The simplest way of modeling the flexible membrane is to use a rigid wall. The interaction between this membrane and the particles is treated in the same way as particle-particle interactions or the particle-wall interaction described for the CBR test in Chapter 2, thought the wall properties are somewhat different. For this

boundary model, the deformation associated with the rubber membrane and the hydrostatic pressure is essentially neglected. This type of model has been used by Ng and Wang [39]. Using this model they observed that the macroscopic friction angle is lower than compared with that of real triaxial tests on glass beads. Other researchers [42] have used variations of this model where, in addition to the simplified rigid wall assumption, they assumed that the tangential force between a particle contacting the boundary and the membrane is negligible and set these tangential forces equal to zero. The interaction force between the particles and the membrane is assumed to be only in the direction that is normal to the plane of contact (See Figure 2.1 (b)) and describable purely by Equation 2.2(a). This class of models for the rubber membrane has some obvious advantages. In particular, the required computational time is significantly less than other models that will be described shortly. However, the model lacks a clear definition of the confining pressure. As the confining pressure is an important component of the resilient modulus test, and the value of the resilient modulus has been shown to be dependent on the confining pressure (See, for example, Ref. [34]), ignoring it makes it less appropriate for even a qualitatively accurate model for the MR test. Therefore, this model was not used for the research described in this report.

Other models have used periodic boundary conditions to model triaxial compression test [23, 47]. In this model there is no physical boundary. The particles on one side of the system interact with particles that are on the opposite boundary, and those particles that are pushed out on one side are added to the system on the opposite side. Some researchers have used periodic boundaries only in the transverse direction. Others have used periodic boundary condition in every direction. There are two disadvantages for this type of boundary. The first is similar to the disadvantage of the rigid boundary: there is a lack of a clear definition for the confining pressure. The second disadvantage involves an unnatural effect resulting from a periodic boundary. If there is a localized deformation that runs diagonally across the sample, the periodic boundary conditions force this to result in several parallel deformations across the sample. This class of models was not used for the resilient modulus membrane for the work described in this report.

The most elaborate model for the confining pressure and the rubber membrane is developed by Bardet and Proubet [29] for biaxial compression test. This model represents both the flexibility of the rubber membrane and the applied confining pressure. Unlike the other models for the wall described to this point, the boundary wall is not predefined. Instead, the boundary wall is defined using the particles that exist along the edge of the system. Essentially, the centers of the particles are connected by straight lines. Then, the magnitude of the local force on the boundary is calculated for every pair of particles as the product of the length of the line connecting those particles and the confining pressure. The direction of the force is always perpendicular to the direction of the lines. The force is divided between the two particles based on the distance of the centers of the particles to the center of the line. The line that connects the centers of the two particles can be assumed as a beam and the two particles can be assumed as a simple support. The force/reaction on two particles is calculated by considering equilibrium of forces and moments. While physically, this seems the most complete model for the boundary, there is no consideration for the properties of the rubber membrane. Further, the three-dimensional realization of this model for the boundary is extremely computationally intense. In 3-D models, instead of connecting two particles at the edge with a line, three particles are connected to form a triangular plane (instead of a line as in the 2-D case). For a mixture of particles, deciding on

which particles relatively near to the outer boundary should be included is somewhat arbitrary. Then, the force on each triangular plate is calculated as the product of the confining pressure and the area of the triangle. This force can be divided among the three particles equally or, more accurately, proportional to their interior angles [30]. Again, there is no consideration of the material properties and the subsequent effect of the rubber membrane. As Kuhn [30], showed this model is a better representative of the effect of the confining stress and the flexible rubber membrane than the fixed boundary models. However, this model requires much more computation time than the other models. For these reasons its potential effective application of this model to DEM models for resilient modulus test is limited. So far this model has been used for rectangular 2-D prism samples only. It has not been used on cylindrical specimen and was not used for the work describe in this report.

Another simple model to represent the confining pressure is one that directly represents the hydrostatic pressure via what might be called a 'hydrostatic boundary' (without consideration of a flexible membrane as described above). This model was proposed by Ng [32] for use in the model for a triaxial compression test. In this model the boundary of the lateral walls is predefined. The force from confining pressure on the particles touching this boundary wall is calculated as the product of the so-called "contact area" and the confining pressure. To define the contact area it is helpful to note that, as in the case particle-particle or particle-wall contact, a particle is allowed to overlap with the boundary wall (Figure 3.1). The contact area is the cross-sectional area of contact between a particle and the boundary wall. The total force between all particles in contact with the wall and the wall itself may be normalized using the product of the wall area and the hydrostatic pressure.
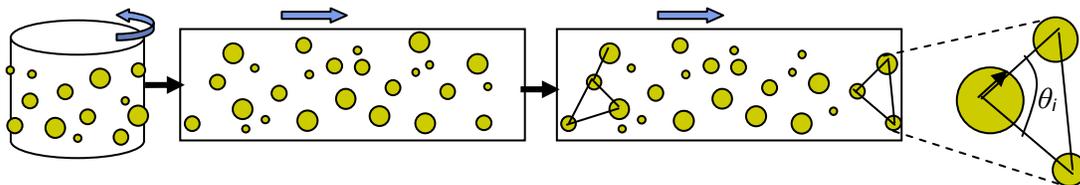


**Figure 3.1:** Illustration of force calculation due to the hydrostatic boundary. The figure shows how centers of particles touching the lateral boundary are mapped into a rectangular plane and the formation of the Delaunay Triangulation. The confining pressure is then applied on each triangle depending on the area of the triangle.

Although this model represents the confining pressure better than the first two models described previously, it neglects the local force imbalances due to the spaces between the particles on the flexible rubber membrane. In other words, this model only considers the local pressure in terms of a global force balance, not in terms of local force balance. Further, it does not consider the effect of the rubber membrane. While the computation requirement is comparable to the periodic and rigid boundary wall conditions, when it was tested for use with the resilient modulus model, it was found ineffective and sometimes unstable. Therefore, this model was not used for this report. Instead, a modification of this model was used as described below.

For this report a *modified* hydrostatic boundary which accounts for the pressure on the membrane between the regions into which the particles protrude is used as well as some effect of the rubber membrane. This method is relatively simple compared to the flexible boundary but more representative of the rubber boundary than the simple hydrostatic boundary. In this model, the force the particles encounter during contact with the wall is a combination of the force due to contact with a rigid wall with properties of rubber (E =103 MPa, v =0.1 and μ = 0.5) and the force associated with hydrostatic pressure at the boundary. The total force F on the particle touching the boundary is gives as

$$F = F_{wall} + F_{hydrostatic} \qquad (3.1)$$

$F_{wall}$ represents the interaction that involves the rigid boundary and it is calculated using Equation 2.2-2.8 with the properties of rubber. It involves a normal and tangential component, as in Equations 2.2(a) and (b).

The hydrostatic force ($F_{hydrostatic}$) is similar to that derived using the hydrostatic boundary method described above but modified to account for the pressure on the membrane between the regions into which the particles protrude. The centers of contact points between particles overlapping the predefined boundary are connected by triangles.

To make the triangulation procedure easier, the cylindrical boundary is unwrapped into a rectangular plane and the centers of the contact points, which are in 3-D coordinates, are mapped to the rectangular plane (2-D coordinate system). These mapped points are then connected by the Delaunay Triangulation (DT) method (see Figure 3.1) [53].

The DT for any N points in the 2-D plane is a triangulation such that no point in N is inside the circumcircle defined by a triangle connecting three points. The DT tends to avoid extremely small or extremely large angles. In other words, the DT maximizes the minimum angle of all the angles of the triangles. For example, for points A, B, C, and D representing the projected centers of four particles overlapping the boundary, one way of detecting if point D lies inside the circumscribing circle defined by points A, B and C is to solve the following determinant:

$$\begin{vmatrix} A_x & A_y & A_x^2 + A_y^2 & 1 \\ B_x & B_y & B_x^2 + B_y^2 & 1 \\ C_x & C_y & C_x^2 + C_y^2 & 1 \\ D_x & D_y & D_x^2 + D_y^2 & 1 \end{vmatrix} \qquad (3.2)$$

Here the subscripts x and y indicate the x and y coordinates of the projected center of the particles. If the determinant is positive then D lies inside the circle defined by points A, B and C, triangle ABC does not form a DT. Otherwise, points A, B and C form DT. All possible sets of three particles are examined in this way until the subset of triangles or triplets of particles are identified as the Delaunay Triangulation for a particular configuration.

After forming the triangulation, the load on each particle due to the hydrostatic pressure is calculated for each vertex and applied, normal to the membrane, at each vertex to the particle

37

whose cross-sectional area is centered at the vertex. The magnitude of the load is calculated using the area of the particle cross-section and a portion of the load on each triangle in contact with the associated vertex. The force of the load on particle $i$ may be expressed as

$$F_i = pA_{Pi} + p\sum_k A'_{k,i} \tag{3.3}$$

$A_{pi}$ is the contact area between particle $i$ and the membrane, $p$ is the hydrostatic pressure, $A'_{k,i}$ is a weighted area of triangle $k$ attached to vertex $i$ (associated with particle $i$) defined in more detail presently.

The first term in Equation 3.3 is the load applied directly to the particle from the hydrostatic pressure. The second term is due to the redistribution of the hydrostatic pressure applied to the membrane between the particles, redistributed among neighboring particles. The weighted area of triangle k attached to particle i whose pressure is redistributed to particle i is determined using the following equation:

$$A'_{k,i} = A'_k \left( \theta_j r_j^2 \Big/ \sum_m \theta_m r_m^2 \right) \tag{3.4}$$

$A'_k$ is the area of triangle $k$ from which the cross-sectional areas of the associated particles have been subtracted, $r_j$ is the radius of the circle that defines the cross-section of particle $j$ with the membrane and $\theta_j$ is the angle at the vertex $j$ of the triangle $k$

Every time step requires that the intersection of the particles with the boundary be determined, along with their cross-sectional areas, the configuration of the Delaunay Triangulation, and the associated calculations described above. The simulations are done based on this boundary configuration.

Once the initialization of the particle configuration is achieved, the modified hydrostatic boundary is used to apply the confining pressure in all directions (triaxial confining pressure) to consolidate the granular materials. In the axial direction of the cylinder the confining load is applied through the stone platen at the top surface. In the transverse direction the stress is applied as described above.

After the specimen is consolidated under the triaxial confining pressures, cyclic deviator load is applied in the axial direction: through the stone platen at the top surface. The cyclic load is applied according to the specification discussed in Chapter 1 (Figure 1.3). For every cycle the corresponding resilient modulus of the granular material is calculated as the ratio of the maximum deviator stress and the resilient (recovered) strain. For the first few cycles the MR values vary a lot. This is due to 'massive' particle rearrangements in response to the deviator stress. For subsequent cycles, this permanent deformation gets smaller and smaller, and the MR value stabilizes. The simulation is terminated after the MR approached a constant value. In real experiments, the deviator stress is applied for few hundreds of cycles. In the simulations, the MR converged somewhere between 30 to 150 applications of the deviator stress.

Figure 3.2 shows typical strain (%) incurred for a simulated MR test for the first nine cycles of deviator stress. This test is performed for a specimen comprised of 1500 particles, each with diameter d=10 mm. The diameter of the container is approximately D = 150 mm, the height of the sample is approximately H=80mm but slightly varies over the course of the experiment as the permanent deformation increases. The confining and maximum deviator stresses are 35 kPa and 70 kPa respectively. As shown in the figure the strain (%) is always very small. The permanent deformation for the first cycle is larger than for the remaining cycles and decreases over the course of the experiment. The MR calculated at the end of the simulation is 130 MPa.
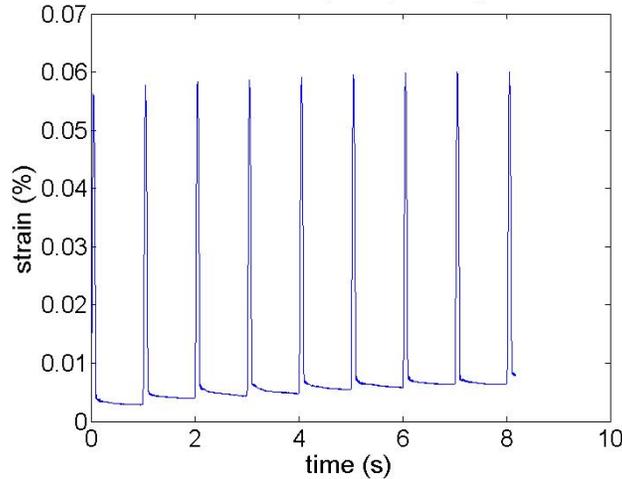


**Figure 3.2:**  Strain (%) vs. time curve. The graph shows strain (%) incurred during application of the first nine cycles of deviator load. The confining and maximum deviator stresses were 35 kPa and 70 kPa. These results are from a specimen comprising 1500 particles with physical properties of d = 10 mm E = 20 GPa, $v$ = 0.15, $\mu$= 0.5 and $\rho$ = 2650 kg/ m$^3$.

The next section shows the results of the MR test for a variety of system parameters.

### 3.2  Results from the Resilient Modulus Simulation

The resilient modulus (MR) can be affected by several factors. Well-known factors that affect the MR include the modulus of elasticity of particles and the applied stresses.  Also, the accuracy of the test is considered limited when the ratio of the particle diameter to the sample diameter (d/D) is too large.  Thus, there is some dependence of the results on this ratio, though the details are not known.  For this report, the dependence of the test results was investigated for three parameters. First, the dependence on modulus of elasticity was investigated; then the dependence of the results on the bulk and deviator stress was studied.  Here, these results are compared with results found from real physical tests to help validate the computational simulations.  All tests were performed with the same container size described in the previous section, diameter D = 150 mm and height H ~ 80 mm.  The small value for H was used to save computational time.  A larger value of H was used for a couple tests and found to produce the same trends, though the results are limited by small H in a similar manner in which they are limited by small D (see

section 3.2.3 for discussion of the latter). Finally the dependence of MR on the particle size is investigated; though there is no detailed quantitative measurements on the literature, there are some rules of thumb for choosing particle size and container size that will be discussed in this context.

### 3.2.1    *Modulus of Elasticity*

The particle modulus of elasticity, or Young's modulus, is seen as one of the most important factors in describing and predicting the behavior of materials in field applications. In this report the term modulus of elasticity refers to modulus of elasticity the material of individual particles, i.e., the Young's Modulus of material, not the 'bulk' modulus of elasticity (or the resilient modulus) of the granular sample as a whole. Wide ranges of modulus of elasticity are reported for different types of rock. For granite Young's modulus ranges from 3 GPa to 30 GPa, and may reach up to 70 GPa in extreme cases.  As demonstrated in Equations 2.2 – 2.6, the Young's modulus affects the interparticle forces in the DEM model.  The normal stiffness of the particles ($k_n$) is directly proportional to the effective modulus of elasticity, a function of Young's modulus and the Poisson's ratio of the two objects that are in contact, as described by Equation 2.5. The stiffness of the particles in the tangential direction ($k_t$) is related to the effective shear modulus, a function of Young's modulus and the Poisson's ratio of the two objects that are in contact, as described by Equation 2.7. The damping coefficients, $\eta_n$ and $\eta_t$ are both dependent on stiffness of the particle in the normal and tangential directions respectively.

The MR simulations are performed for specimen with different values of modulus of elasticity while keeping other physical parameters such as material density and Poisson's ratio for the particle material constant. Two examples are shown in Figure 3.3.

Figure 3.3 (a) shows the stress vs. strain (%) time curve for a specimen comprising 1500 particles of diameter 10 mm. The physical parameters of the particles are E =29 GPa, $\nu$ = 0.15, $\mu$= 0.5 and $\rho$ = 2650 kg/m$^3$.  The confining pressure and the deviator stress are 35 kPa and 70 kPa respectively. The strain approaches a constant value after 170 applications of cyclic deviator stress (Figure 3.3 (b)). Figure 3.3 (c) and (d) show results from MR test simulation for the similar setup as the previous one but with E = 2.9 GPa. The permanent deformation approaches a constant value after 30 application of deviator stress; fewer application of deviator load than the previous one.
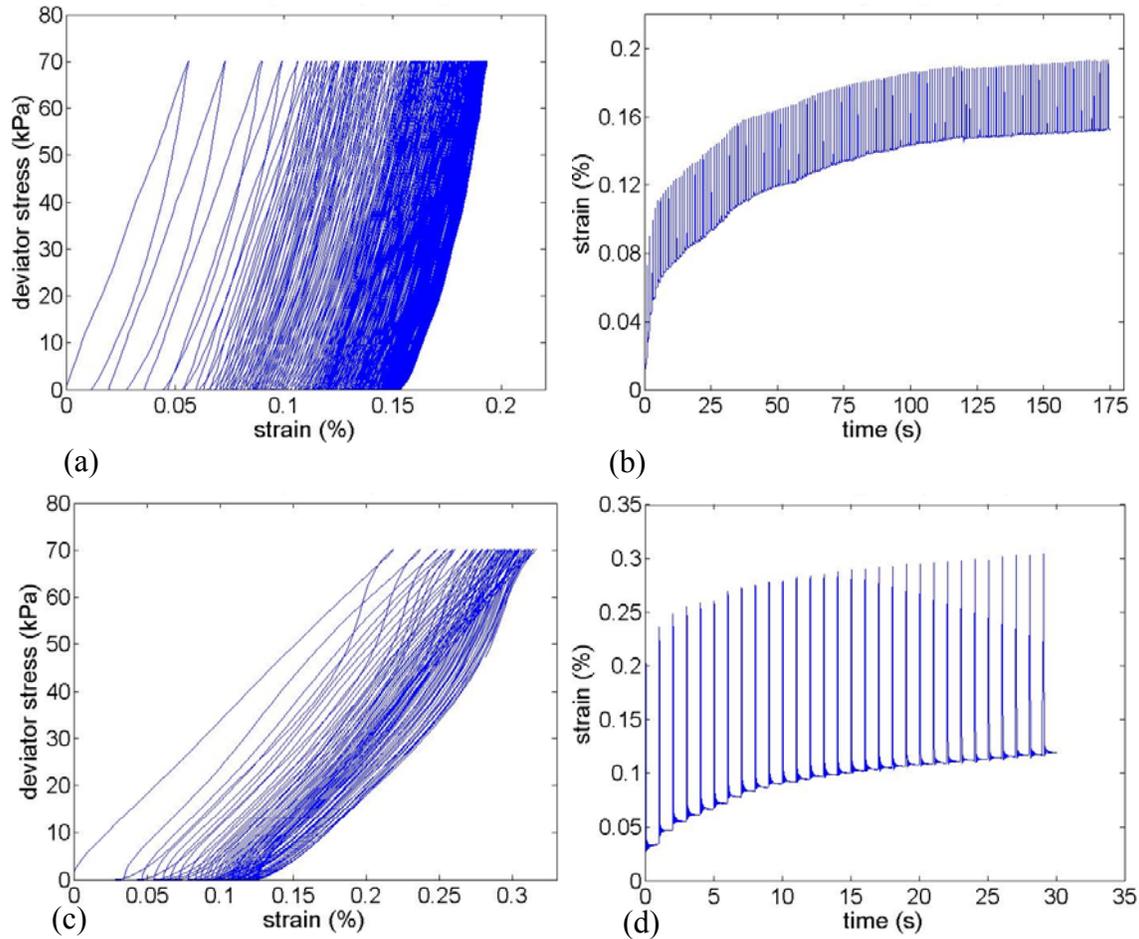
**Figure 3.3:** Typical results from MR simulation. (a) shows the stress-strain curve for specimen comprising 1500 spherical particles with physical properties d = 10 mm E = 29 GPa, ν = 0.15, μ= 0.5 and ρ = 2650 kg/ m³. (b) shows the strain incurred for the simulation as shown in a. The permanent deformation approaches a constant value after application of 170 cycles of deviator stress. (c) shows stress-strain curve for another specimen which is similar as described in (a) but with E = 2.9 GPa. (d) shows the strain incurred for the simulation shown in c. The permanent deformation approaches a constant value after application of 30 cycles of deviator stress.

Comparison of the strain-time curves for these two samples results shows that the specimen with lower modulus of elasticity deforms more during loading phase of the deviator stress. This specimen has also a larger resilient strain; large strain is recovered during the unloading phase of the deviator stress. Figure 3.4 the shows strain vs. time plots for the first 6 cycles from Figure 3.3 (b) and Figure 3.3 (d), clearly illustrating the difference in the amount of strains in the two cases.
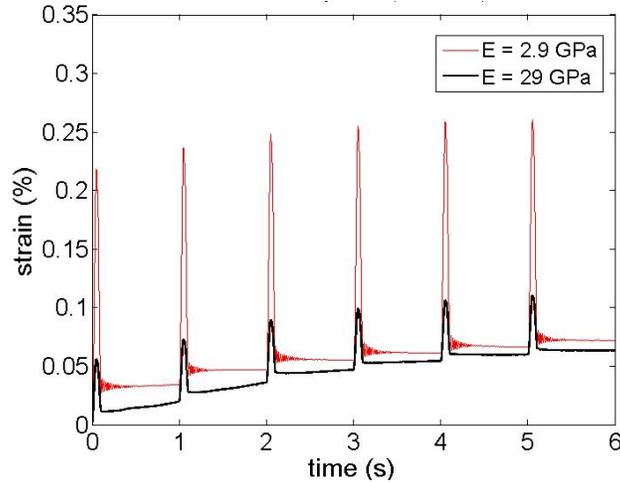
**Figure 3.4:** Strain(%) for different modulus elasticity. The figure shows comparison of strain for specimen comprising particles with modulus of elasticity of 2.9 GPa and 29 GPa. More strain is observed for the softer material.

During the simulation the MR (ratio of maximum applied stress to recovered strain) is calculated for each application of deviator load as in Equation 1.2. Figure 3.5 shows the calculated MR for every application of deviator load for the two specimens. The scatter plots in the figure indicate the MR for every application of deviator stress and the line plots indicate the average MR for three consecutive applications of deviator load. As mentioned previously, the simulation is terminated once the MR reaches a constant value. Since a steady state was reached quickly for the softer material, fewer cycles of deviator stress were applied for the softer material.

The MR calculated at the end of the simulation for the specimen with stiffer particles is 170 MPa and for the other specimen it is 37.5 MPa. These results cannot be considered exact representatives of real granular materials because the particles are spherical and unisized. However, the MR values are in a reasonable range for well compacted granular aggregates, a fact which lends confidence that the trends of the test results are representative of trends in real materials. MR values for real granular materials range from 150 MPa for sand to 250 MPa for crushed limestone [54].

In addition to the two simulations described above, the MR simulation is performed for particles with modulus of elasticity of 4, 7, 9, 15 and 20 GPa. The stress-strain and the strain-time curves for the simulations look very similar to those shown in Figure 3.3 with smaller deformations for the stiffer materials and larger deformation for the less stiff materials. The calculated MR for each specimen is plotted as a function of material modulus of elasticity of particles (E) in Figure 3.6. It is interesting to note that the MR increases linearly with the modulus of elasticity with a very small error associated with it. Similar trends have been noticed in 2-D DEM simulations for MR test [36].

42
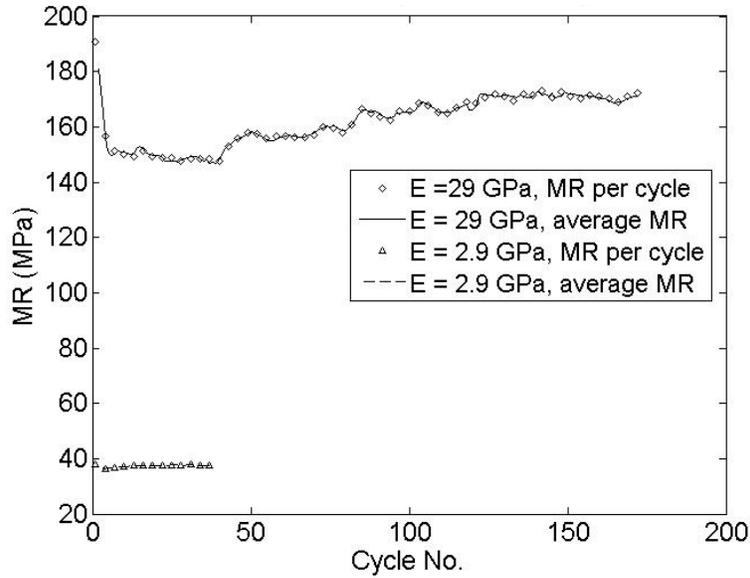
**Figure 3.5:** Calculated MR. The calculated MR from the simulation for two specimens with E = 2.9 GPa and E = 29 GPa. The symbols indicate the MR for every application of deviator load. The lines indicated the MR averaged over three consecutive MR values for every application of deviator stress.
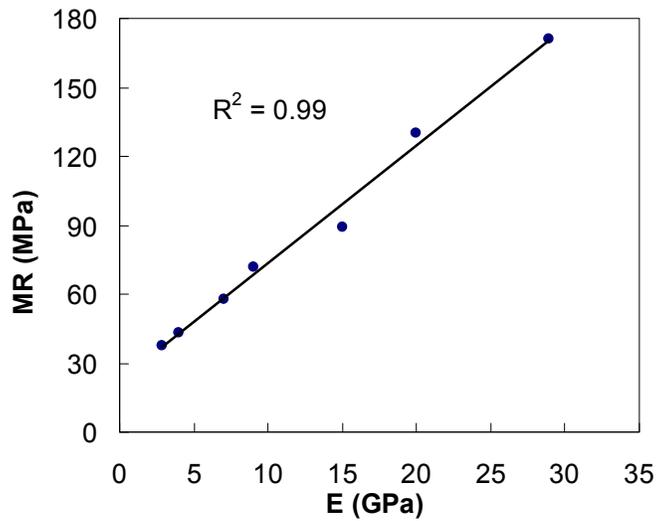


**Figure 3.6:** MR vs. E. The graph shows the calculated MR from simulations as a function of particle modulus of elasticity. The simulations are done for particle modulus of elasticity of 2.9, 4, 7, 9, 15, 20 and 29 GPa. The graph shows that the MR is a linear function of the particle modulus of elasticity.

43

### 3.2.2 *Applied Stress*

The effect of the applied stress on the MR test has received great attention in the geomechanics community [35]. Experiments on granular aggregates have shown that the MR increases with both the confining pressure and the deviator stress [35].The variability in test results as a function of applied stress has implications on how a test result must be interpreted. Experiments by Hicks [35] showed that the MR is highly dependent on the confining pressure and relatively less dependent on the deviator stress. Hicks used a bulk stress (θ) to define the combined effect of the confining pressure and the deviator stress as

$$\theta = 3\sigma_c + \sigma_d \tag{3.5}$$

Where $\sigma_c$ is the confining pressure and $\sigma_d$ is the deviator stress. The factor of three for confining pressure over deviator stress was justified physically by the tri-axial nature of the confining pressure.

Hicks demonstrated that the MR increases as power law function of the bulk stress.

$$MR = k_1 \theta^{k2} \tag{3.6}$$

Where $k_1$ and $k_2$ are constants that depend on the type of granular aggregates. DEM simulations for MR test by Zeghal [34] have shown similar trend.

The NCHRP I-28 [14] standard provides nonlinear regression equation similar to equation 3.6 but with more coefficients to account for pore water pressure and Octahedral shear stress $\tau_{oct}$ ( $\tau_{oct} = \frac{1}{3}\sqrt{(\sigma_1 - \sigma_2)^2 + (\sigma_1 - \sigma_3)^2 + (\sigma_2 - \sigma_3)^2}$ where $\sigma_1$ is the total stress applied in the axial direction and $\sigma_2$ and $\sigma_3$ are stresses applied in perpendicular directions along the horizontal plane. Since $\sigma_2 = \sigma_3 = \sigma_c$, and $\sigma_1 = \sigma_d + \sigma_c$, $\tau_{oct}$ reduces to $\tau_{oct} = \frac{\sqrt{2}}{3}\sigma_d$ for the setup described in this Chapter). In this case, the expression for MR becomes

$$MR = k_1 . Pa \left( \frac{\theta - 3k_6}{Pa} \right)^{k2} \left( \frac{\tau_{oct}}{Pa} + k_7 \right)^{k3} \tag{3.7}$$

where θ is the bulk stress as defined in equation 3.6, Pa is atmospheric pressure, $k_1$, $k_2$, $k_3$ and $k_7$ are regression constants related to material parameters and $k_6$ is related to the capillary suction. However, since Equation 3.6 works reasonably well for the cases described here, this is the expression used to relate the applied stresses to the resilient modulus values in this report.

In this research different combinations of confining pressure and deviator stress were used to investigate the effect of the stresses on the MR. NCHRP I-28 [10] standard procedure for the MR test specifies the magnitudes of the applied confining and deviator stresses. Confining and deviator stresses of 35, 70, 105 and 140 kPa are used in the simulations. These values are very

close to the standard values specified in the NCHRP I-28 procedure. The specimen used in this systematic investigation is comprised of 1500 particles of diameter 10 mm and modulus of elasticity of 9 GPa. Table 3.1 shows the calculated MR from the simulations for different combination of confining pressures and deviator stresses. The MR increased as either the confining pressure or the deviator load is increased. As was found by Hicks [35] and Zeghal [34], the value of MR increased more with increase in the confining pressure than it did with increase in the deviator stress.

**Table 3.1:** MR for different applied stresses. The table shows calculated MR values for specimen comprising 1500 spherical particles with modulus of elasticity of 9 GPa. The simulations were done for different combinations of confining pressure and deviator stresses. The MR increases with the increase of confining pressure and increase of deviator stress.

| Confining pressure(kPa) | Deviator stress(kPa) | MR (MPa) |
|---|---|---|
| 35 | 35 | 63 |
| 35 | 70 | 72 |
| 35 | 105 | 75 |
| 70 | 70 | 90 |
| 105 | 70 | 110 |
| 140 | 140 | 118 |

Figure 3.7 shows the MR as a function of the bulk stress. The MR can be described as a power law function of the bulk stress with high R-square value. The fitting parameters $k_1$ and $k_2$ in Equation 3.6 are 6.07 and 0.476 respectively. These parameters might change for other types of particles. For example, Gudishala [54] found $k_1$ and $k_2$ for sand to be 31.4 and 0.36 respectively.
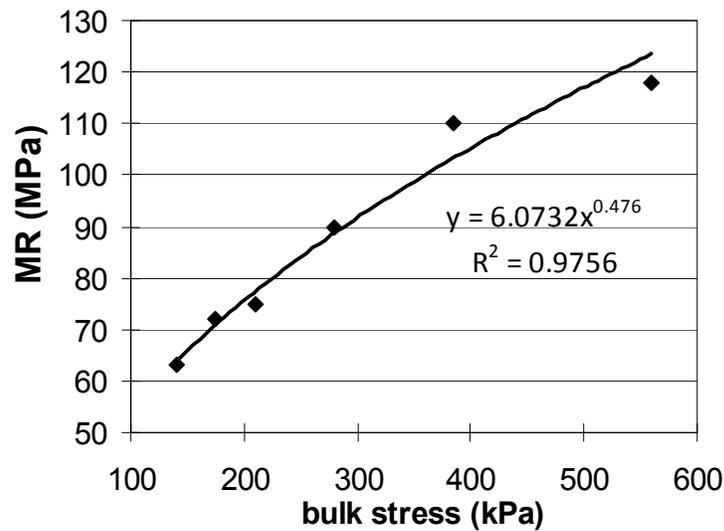
**Figure 3.7:** MR as a function of bulk stress. Calculated MR for specimen comprising particles of 10 mm diameter and 9 GPa of particle modulus of elasticity. MR increases as a power law function of the bulk stress. The constants $k_1$ and $k_2$ in Equation 3.5 are 6.07 and 0.476 respectively.

### 3.2.3    Size of Particles

Another important factor that could affect the MR results is size of particles in the specimen. For the tests described above, the diameter of the container was held constant and possible relationship between the MR results and the ratio of particle size to container size is investigated.

For physical MR experiments, it is recommended that the size of aggregates should be less than one fifth of the container size for reliable results [10]. For the two standard container diameters, 100 mm and 150 mm, the maximum sizes are, therefore, 20 mm and 30 mm respectively. It is commonly thought that the results from the MR test might not represent the true characteristics of the aggregates if larger particle sizes are present in the specimen, but there has been no systematic investigation of how the results might vary with the size ratio of the particles to either container diameter or container height.

To investigate this, a few simulations are run using particles of different sizes.  Six simulations are performed, for monosized particles of diameter 10, 12.5, 15, 17.5, 20 and 25 mm. The other physical properties of the particles are the similar (E = 9 GPa), except the size of the particles. A confining pressure and the deviator stress were 35 kPa and 70 kPa respectively.  Figure 3.8 shows the calculated MR as a function of the ratio of the particle diameter d and the container diameter D.

Somewhat surprisingly, there is no single trend in this relatively narrow range of size ratios.  For particle sizes which are less than 10% of the container diameter and less than 18.7% of the container height, the calculated MR varies slightly, though the value is close to 70 MPa. For particle sizes greater that 10% of the container diameter (and 18.7% of the container height) the

MR shows very large deviations. There is a sudden jump at 10% and then a gradual decrease. There could be several reasons for this, but clearly more computational experiments need to be performed to resolve the details. The jump in MR at $d/D \sim 0.1$ could indicate a significant change in something related to the particle packing such that the measured response below this value is something quite different than the results from above the ratio of d/D. This could be related to the recommendation that one chooses measurements only for particles of a smaller value of d/D. The change in packing could be due to the ratio of d/D or d/H or both. The jump in MR might even indicate a greater dependence of the results on d/D than would be expected, a variation that might even be seen for smaller values of d/D. Clearly, more tests need to be performed before anything can be said about any of this. One thing is clear from these results – at least in the range of tests performed, the reported MR value is highly dependent on ratio between particle size and container diameter d/D for values above $d/D \sim 0.1$ and this must be taken into account for any comparisons that are performed on different types of materials.

### 3.3  Summary of Resilient Modulus Simulation

The model developed for the MR test was able to demonstrate the dependence of the resilient modulus on different factors. The resilient modulus was noticed to increase linearly with the modulus of elasticity of particles. The resilient modulus also increases with the increase in bulk stress, as a power law function of the bulk stress. Since the DCP test configuration is different from the MR test, it will be important to understand how some of the dependence of test results on system parameters differs. The next Chapter presents the details of the simulation set-up and results for the DCP test.
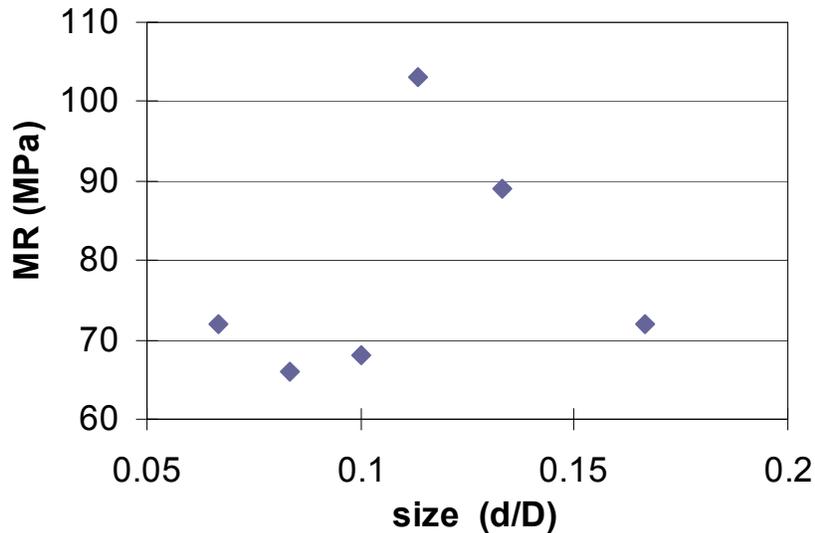


**Figure 3.8:** MR for different particle size. The graph shows calculated MR for different particle size. The x-axis is the size of particles normalized by the diameter of the cylindrical container (150 mm). The y-axis shows the MR in MPa. For d/D < 0.1, the MR value is relatively stationary, but for larger values of d/D the value for MR is significantly more variable.

# Chapter 4
# Dynamic Cone Penetrometer Simulation


The DCP test is a field test which is used to characterize granular materials. As described in Chapter 1, it is also one of the tests that may be used as input for the MEPDG design guide for appropriate choice of pavement materials. Unlike the CBR and MR tests, the DCP can be used to assess the stratification and stiffness of the layers *in situ*. The DCP test is also different from the other two tests in that it does not have a well defined boundary. This Chapter provides detailed information about the DCP simulation setup as well as some results. As will be shown, the DCP simulation was used to investigate the effects of different particle properties and boundary conditions. Some of the results from these sensitivity tests are also presented is this Chapter.


## 4.1    Dynamic Cone Penetrometer Simulation Setup

The DCP test, like the CBR test, is also a penetration test. However, the DCP test is a field test where wall boundaries do not exist. Ideally, a simulation would accommodate this through some sort of infinite domain. However, this is not possible. Instead, for the work described in this report, a cylindrical container is again used as the domain for the test in a similar manner as was used for the CBR test. To partly accommodate this discrepancy, the properties of the container are set as that of the particles and then the dependence of the results on the size of the container (height and diameter) is investigated. The tests that are shown are surely size-limited. That is, the results would likely be quantitatively different were an infinite system is used. However, there had to be some balance between computational time (to minimize it) and system size (to maximize it). Therefore, a system size was chosen that was big enough to exhibit results that resembled field test results. Then without too much worry about finite size effect, the particle properties were varied primarily to investigate qualitatively how the measured results vary with particle property.

Typically, as one would expect, there is no lid cover for the DCP test. However, a physical test involves several penetrating blows pushing the cone far beneath the surface before the displacements are considered. To mimic the resulting effect of the soil over the sample when the data is recorded, a movable "surcharge load" is added to the top that acts similar to the effect of a rather loose lid on the system. This will be discussed in detail below.

As in the case of the other two tests, the initial step of the simulations consists of the initial placement and release of the particles. Then, the granular material is compacted.

The apparatus used for the model DCP tests described here consists of a long rod with a cone at the tip, the anvil and the falling hammer. The cone and the rod are modeled as combination of conical and cylindrical wall. As in the CBR plunger, tiny particles are used at the joint of the conical and cylindrical wall to create smooth and computationally manageable boundary. Prior to

simulating the *full* DCP test with the hammer drop, some of the basic material properties were studied using the cone drop test as described presently.

### 4.1.1  Preliminary Development: Cone Drop Test

The cone drop test is another commonly used field tests. This test involves dropping a cone onto a specimen from near the top surface. The amount of penetration from this single drop is considered as a measure of the stiffness of the granular materials. This rather simple simulation was used as a first step to develop the final model for the DCP test. In this simulation, a cone that weighs 0.1 kg is dropped from a typical height of 5 mm above a bed of particles – the movement of the cone is restricted to the vertical direction. Figure 4.1 shows a sketch of this test as well as the penetration depth by a light weight cone during a typical cone drop test simulation. For the results shown in Figure 4.1, the specimen comprises spherical particles of d = 10 mm, E = 29 GPa, $v$ = 0.15, $\mu$= 0.5 and $\rho$ = 2650 kg/ m$^3$. The light weight cone penetrated more than 60 mm, rather large compared to realistic tests, but the results are not necessarily surprising, as will be discussed shortly.

### 4.1.2  Preliminary Development: DCP Details

To model the full DCP an anvil and a falling hammer were added to the cone drop model, as shown in Figure 4.2.  The anvil is connected the cylindrical rod. The hammer, which weighs 8 kg, is then dropped onto the anvil from standard height of 0.575 m.  Dropping the hammer from the standard height in the simulation takes long and unnecessary time. To create a more efficient, equivalent test, the hammer was given a downward velocity of 3.22 m/s just above the bed (from a height of 0.045 m), as it would have if it were released from rest at the standard height of 0.575 m. The penetration after the hammer drop is recorded as the Dynamic Cone Penetrometer Index (DPI).



(a)                                                                                  (b)
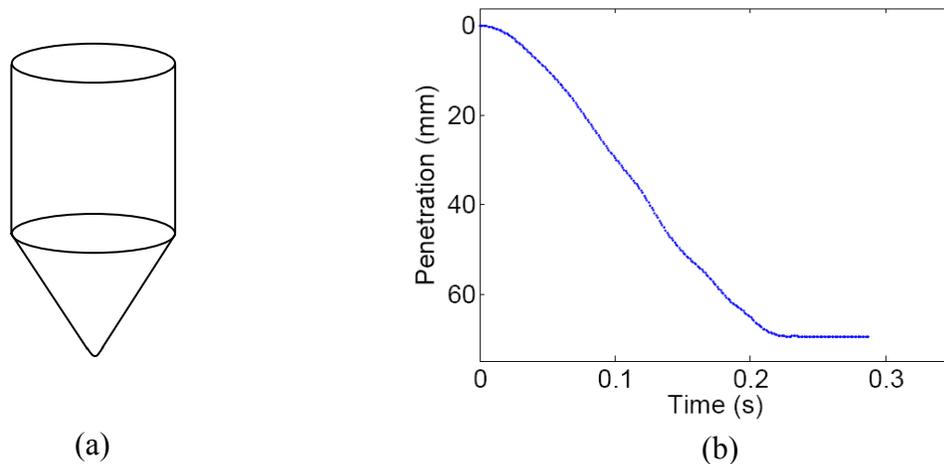
**Figure 4.1:**  (a) Schematics of 'light weight' cone. (b)Results from the light weight cone drop test described in the text: graph of the penetration of the cone as a function of time. The graph shows penetration depths of a cone dropped a granular material. The specimen comprises 5000 10 mm spherical particles. The material properties are E = 29 GPa, $v$ = 0.15, $\mu$= 0.5 and $\rho$ = 2650 kg/ m$^3$.

49
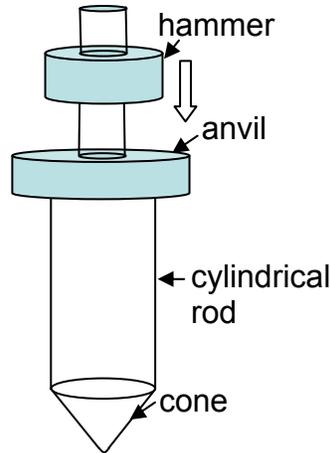
**Figure 4.2:** Schematics of DCP apparatus (not to scale). The cone is connected to the cylindrical rod. The hammer is dropped onto the anvil, which is attached to the cylindrical rod.

### 4.1.3 Surcharge Load

As discussed in Chapter 1, in real DCP tests the penetration for the first three hammer drops is not included in the DPI. In other words, test results are reported from hammer drops when the material that is being penetrated by the cone is covered and weighted down with several layers of particles from above. These layers act as a somewhat movable but heavy load and add effective stiffness to the material. This effect could be reproduced computationally by adding thousands of particles to the modeled particle system and repeating the drops several times, as in the field test. However, this would be computationally unmanageable.

To model the effect of these layers or material overload and yet minimize the additional computational time requirement, the overload is represented by a solid surcharge load. A solid block that has the same material properties as the particles, equivalent in weight to, depending on the test, - 1-3 feet of surcharge load, is placed on the top surface of the granular materials. This surcharge load is similar to the lid cover in the CBR model but different in that it is free to move in the vertical direction as particles push it up from below. Figure 4.3 (a) shows penetration of DCP vs. time for a system subjected to a 300 mm surcharge load during initial placement and the hammer drop. The DCP will penetrate some distance during placement due to its weight. This penetration is minor compared to the penetration due to the hammer drop. Figure 4.3 (b) is visualization from the simulation just before the DCP is placed on 5000 particles of size 10 mm. The surcharge load is not shown in this figure.

The results shown in Figure 4.3 (a) are quite reasonable compared with field DCP tests of open-graded materials as will be detailed shortly, so this is the method used for simulating the DCP tests described in this report.

(a)  (b)
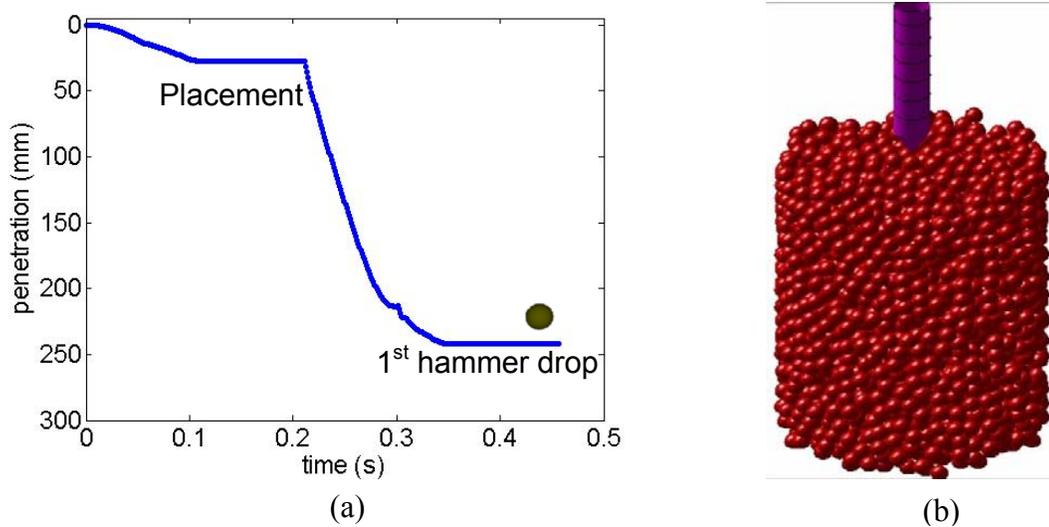
**Figure 4.3:** Typical result from DCP. (a) The graph shows the penetration incurred from a DCP test simulation during placement and first hammer drop. The penetration during the placement of the DCP is due to the weight of the apparatus. After the hammer is dropped the DCP penetrated larger depth. This test was performed for specimen comprising 5000 particles with physical properties of d = 10 mm, E = 29 GPa, ν = 0.15, μ= 0.5 and ρ = 2650 kg/ m³. The surcharge load used is equivalent to 300 mm of granular materials of material density 2650 kg/ m³ and solids fraction 0.60. b) Shows a snap shot from the DCP simulation: just before the DCP is placed on the surface of the sample.

## 4.2   Results from the Dynamic Cone Penetrometer Simulation

The penetration depth in the DCP test might be affected by several factors. Usually, higher penetration depths are observed for DCP test on open graded granular soil [14] than for well graded materials. For these tests, the typical solids fraction ranges from 55%-65%, which can be considered as open graded materials.  The DCP model was used to investigate some additional physical parameters that determine the depth of penetration to assess how they affect the penetration. The particle physical properties that are studied in the DCP test simulations include coefficient of contact friction, particle shape and modulus of elasticity.  Other parameters such as the porosity of the specimen, surcharge load and container size are also studied using the DCP simulation. The results from these simulations are presented in this section.

### 4.2.1   Coefficient of Friction

As described in Chapter 2, once the ratio of the tangential force and normal force between two contacting particles exceeds the material coefficient of friction, the particles will slide relative to one another. Sliding of particles causes deformation in the 'bulk' specimen.  This indicates that the higher the materials coefficient of friction the less the penetration but does not give a quantitative measure of that relationship.

The 'light weight cone drop' simulation was used to investigate the measurable effect of friction on the depth of penetration by changing the value of μ in Equation 2.2b. No surcharge load was used for these simulations. The light cone weighs 0.1 kg and was dropped on specimens, each comprising particles with different coefficients of contact friction. Each specimen comprises 5000 particles with gradation of 10%: 60%: 30% 19 mm: 9.5mm: 4.75 mm. Figure 4.4 shows penetration depths from 'light weight cone drop' test simulation for specimens with coefficient of contact frictions 0.5, 5, and 500. The value of 0.5 (equivalent to $\tan^{-1} 26.5°$) is the approximate value of the coefficient of friction for quartz. Again, as mentioned previously in Chapter 3, it should be also noted that the contact friction is different from the bulk friction that is usually used to describe the shear strength of granular materials. The bulk friction (or sometimes referred to as macroscopic friction) is usually given in terms an angle that corresponds to the repose angle formed by cohesionless granular materials. On the other hand, the particle contact friction, which is used in Equation 2.2 (b), is the friction between two contacting particles. The particle contact friction is usually given in terms of dimensionless numbers. To maintain consistency, the particle contact friction is given in terms of dimensionless numbers throughout this report. The container has the same physical properties as that of the particles. The diameter of the container is 90 mm.
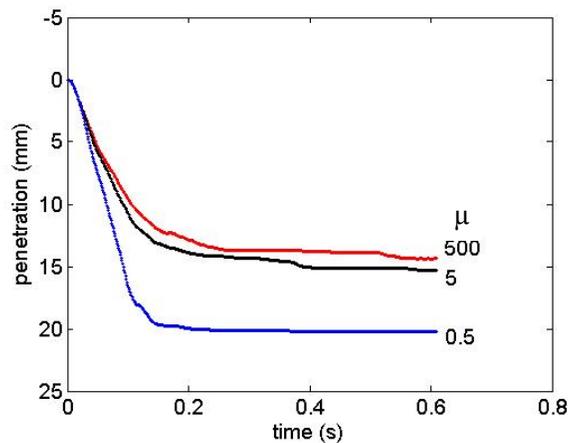


**Figure 4.4:** 'Cone Drop' test: coefficient of contact friction. The graph shows penetration depths of a cone dropped on specimens that have different coefficient of contact friction (0.5, 5 and 500). The tests were performed on a specimen that has gradation of 10%: 60%: 30% 19 mm: 9.5 mm: 4.75 mm. The difference between the penetrations for coefficients of friction of 0.5 and 5 is of the same order of the smallest particle size.

The cone penetrated 20 mm for the test on specimen with coefficient of friction 0.5 whereas the penetration was close to 15 mm for the specimens with coefficient of friction 5 and 500. Taking into account the smallest size of the specimen, 4.75 mm, the difference between the three penetration depths is essentially negligible. This shows that increasing the contact friction beyond 0.5 does not improve the stiffness of spherical ensembles.

More simulations were performed to investigate the effect of contact friction on the penetration depth of DCP. DCP placement simulation was performed on similar specimen as described in Figure 4.4, though a more realistic setup was attained through a surcharge load. A surcharge load

equivalent to 300 mm of granular material was applied on the top surface. The coefficients of friction of the particles were varied only between 0.2 and 0.5. In this case, slightly more significant differences were noticed. The DCP penetrations were 95 mm, 78 mm, 63 mm, 43 mm and 40 mm for specimen with coefficient of friction of 0.2, 0.25, 0.3, 0.4 and 0.5 respectively (Figure 4.5). This shows that the depth of penetration decreases significantly when the coefficient of friction is reduced below 0.4.
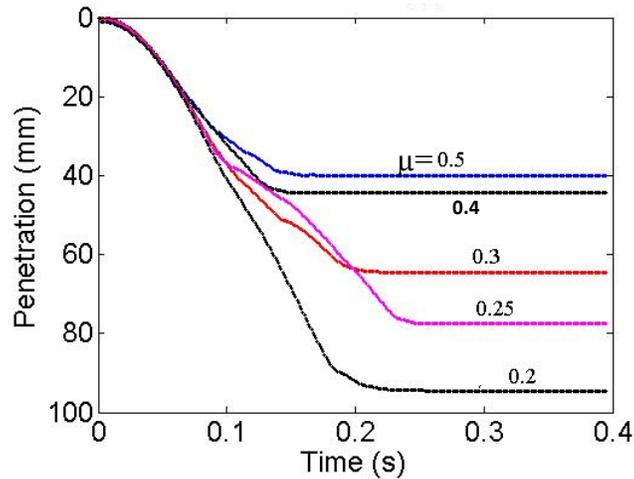


**Figure 4.5:** DCP test: coefficient of contact friction. The figure shows penetration depths incurred during placement of the DCP on specimens with different values of coefficient of contact friction (0.2, 0.25, 0.3, 0.4 and 0.5). The penetration decreases as the coefficient of contact friction increases. The difference in the penetration depths is larger for lower coefficients of friction. However, the penetration depths do not vary much after the coefficient of friction of 0.4. The particle material properties are as mentioned in Figure 4.3and the surcharge load is 300 mm thick.

Combining the observation from the two sets of simulations, the 'light weight cone' drop and the DCP placement, it can be concluded that increasing the coefficient of contact friction reduces the depth of penetration for very low values of the coefficient of friction. However, coefficient of friction that is more than 0.5 does not have significant effect on the penetration depth. The two sets of simulations on spherical particles with different contact coefficients are consistent with previous DEM based simulations for granular materials [47]. Increasing the contact friction above 0.5, which is the nominal value for quartz, have no significant effect on the behavior of the bulk specimen. However, lower contact friction values allow particles to slide past each other very easily.

The rest of this section deals with other factors that determine the depth of penetration. To investigate these factors the coefficient of contact friction of 0.5 was used in all the simulations.

*4.2.2   Shape of Particle*

Since true granular materials are aspherical particles that can interlock with one another, modeling granular aggregates using only spherical particles might not be adequate. In the DEM model, different shapes of particles can be formed by gluing spherical particles as described in Chapter 2. To investigate how particle shape affects the depth of penetration, three specimen comprising different particle shapes were used and their DPI's under identical test conditions were compared. The first specimen comprises 5000 spherical particles. The second specimen comprises 2500 'couple' particles. 'Couple' particles are particles formed by gluing two spherical particles. In this case two 10 mm spherical were glued together. The third specimen comprises 1667 'triplet' particles. 'Triplet' particles are formed by gluing three spherical particles. Again, the diameter of the spherical particles was 10 mm. The 'triplet' particles were formed such that the lines connecting the centers of the spheres form equilateral triangle. See insets in Figure 4.6for details.  Of course, natural sands and grains are likely closer to spherical than the shapes depicted in Figure 4.6.  On the other hand, these simulations offer a first test of the effect of shape on the relevant test results.  Future tests will involve aspherical grains consisting of multiple spheres with more overlap resulting in more realistic particles.  All spherical particles, of which the particles in the three specimens are comprised, have the same material properties ($E$ = 29 GPa, $v$ = 0.15, $\mu$= 0.5 and $\rho$ = 2650 kg/ m$^3$). In addition, the container has a diameter of 150 mm.  Prior to the cone drop, a surcharge load equivalent to 300 mm deep of granular material was placed at the surface of each specimen.

As shown in Figure 4.6 the initial penetration depths for the specimens with non-spherical particles were significantly less than that of the specimen with spherical particles. It is also interesting to note that the DCP penetration during placement was less for the 'couple' particles than the 'triplet' particles. This might be due to some local arrangement of particles near the top surface of the specimens. After the hammer drop the DCP penetrated the whole depth of the container to the bottom for the spherical particles. This was not true for the aspherical particles. The total penetration, the penetration during placement and hammer drop, for the 'couple' particles was close to 220 mm and it was 100 mm for the 'triplet' particles.
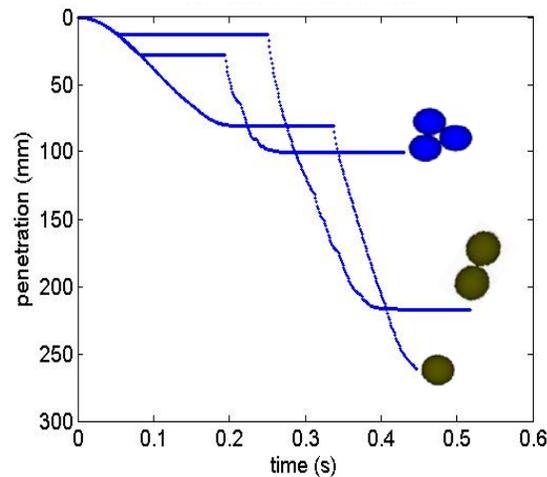
**Figure 4.6:** DCP test: particle shape. The figure shows penetration during placement of the DCP and during the first hammer drop. The test was performed on specimens that contain different particle shape. The first specimen comprises 5000 spherical particles of 10 mm diameter. The second sample comprises 2500 couples, each couple is made by gluing two 10 mm diameter spherical particles together. The third specimen comprises 1667 triplets, which are made by gluing three 10 mm spherical particles. The centers of the three glued particles form an equilateral triangle. The particles in the three cases have physical properties of E = 29 GPa, ν = 0.15, μ= 0.5 and ρ = 2650 kg/ m$^3$. The penetration is larger for the specimen with spherical particles. The penetration during the hammer drop decreases as more particles are glued together.

The reduced depth of penetration for the non-spherical particles is likely due to the interlocking of the 'irregularly' shaped. This is in contrast with the ease with which spherical particles may roll and slide past one another. This assertion also agrees with previous observation on other DEM models [28, 27]. To summarize, generally non-spherical particles give stiffer specimen than specimen made up of spherical particles.

In the past several attempts have been made to correlate the DCP penetration depth to other bulk properties such as the porosity of the specimen and 'bulk' modulus of elasticity [12]. However, as the particle shape plays major role in resisting the penetration, relating the DCP penetration only to porosity of specimen might not be enough. In fact, the porosities of the samples above were: 48%, 45% and 41% for spherical, 'couple' and 'triplet' particles respectively. If one were to make a prediction purely based on porosity, one would predict from this that large penetration would occur for the specimen comprising 'triplet' particles. Unfortunately, it is difficult to determine a manner in which the shape of the particle could be described through a quantitative measure, but this in addition to porosity would likely work together to create a better predictor for DPI of a material, independent of other factors.

*4.2.3   Surcharge Load*

As mentioned above, in field tests, the penetrations for the first three hammer drops are not included in the reported DPI. The effect of the overload of the soil on the reported penetration depth is modeled for the work described in this report by using a surcharge load applied at the surface of the specimen. The weight of surcharge load is described by the equivalent depth of granular particles with density of 2650 kg/m$^3$ and porosity of 40%. For example, a surcharge load of 300 mm is equivalent to pressure of 477 kg/m$^2$.

Figure 4.7 compares the depth of penetration for the DCP simulation during placement and single hammer drop for two different surcharge loads and three different sets of simulations. Three different particle shapes were used for this set of simulations. Otherwise, the simulation setups are exactly the same as the previous test. Figure 4.7(a) shows the results associated with a surcharge load of 300 mm and Figure 4.7(b) shows the results associated with a surcharge load of 600 mm.  There is a significant difference in depth of penetration for all the three types of specimen used. This shows that the depth of penetration for the DCP test highly depends on the surcharge load. In other words, the more the DCP penetrates the more resistance it encounters from the aggregates.

This is an important concept in DCP tests. Typically, the DCP is used to assess aggregate behaviors up to the depth of 10 to 30 cm. This is the main advantage of the DCP test over laboratory or other field tests which measure only a given sample size or the top surface. However, great care is required before comparing the results of DCP penetration at different depths. Usually, the DPI at each depth or for each blow is reported. Typical results indicate less DPI as the DCP penetrates more depth.



(a)                                        (b)
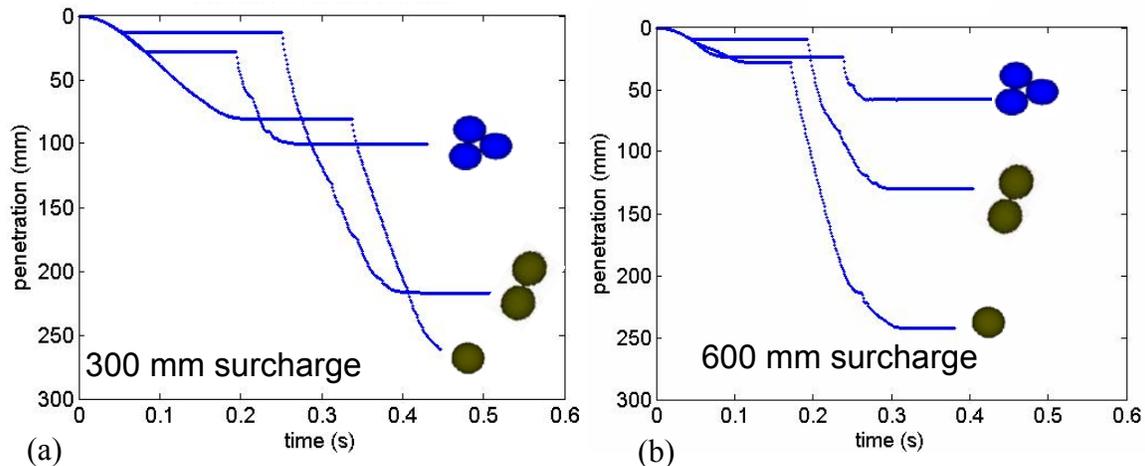
**Figure 4.7:**  DCP test: surcharge load. (a) shows the penetration of DCP for three specimens where a 300 mm surcharge load is applied at the surface. The specimens were made of different shape of particles (Figure 4.6).  (b) shows the penetration of DCP for three specimens where 600 mm surcharge load is applied. The shape of the particles is the same as in a. Increase in surcharge load decreased the penetration for the three specimens.

56

*4.2.4   Modulus of Elasticity*

Young's modulus, i.e. the modulus of elasticity, of the particles played a significant role in the determination of the measure of the resilient modulus.  Therefore, one would expect there to be similar dependence of the DCP test on Young's modulus.  To investigate this, three sets of simulations were performed to study the effect of modulus of elasticity on the depth of penetration for the DCP test.  For each set of three tests, 2500 'coupled' particles (particles comprised of two spheres glued together) were dropped once and allowed to come to rest. Most of the particle parameters were the same as those described above, specifically: $\rho = 2650$ kg/ m$^3$ and $\nu = 0.15$, $\mu = 0.5$. The particle modulus of elasticity, E, for the three sets of tests were 2.9 GPa, 9.0 GPa, and 29 GPa. Each specimen was compacted as described previously and covered with a 300 mm surcharge load.  For each run, the DCP apparatus was placed on each specimen and after the initial penetration the hammer is dropped on the anvil.

Figure 4.8 shows the results from these three different sets of DCP simulation for 'couple' particles with the three values of modulus of elasticity, grouped according to approximately the same porosities. The moduli of elasticity E and the porosities $\Phi$ of each test are noted in the legend.

Perhaps the most obvious and surprising result is the variation not only in the penetration with different initial conditions, but the apparent variation in the penetration as a function of modulus of elasticity E.  Figure 4.8 (a) shows the results from an initial condition that resulted in a relatively high porosity.  It also, on average, resulted in the largest penetration, particularly for the softer materials.  What looks at first as a clear systematic dependence of DPI (penetration due to the hammer drop) on E is somewhat reduced when one considers the difference in drops associated with initial penetration.  However, there is a somewhat lower penetration for the material specimen with the highest modulus of elasticity, E = 29 GPa. The plots in Figure 4.8 (b) and 4.7(c) are results for tests of somewhat lower porosities.  Not surprisingly, the penetration depth is somewhat less than in Figure 4.8 (a).  However, the trends for these similar systems as they vary with modulus of elasticity are exactly opposite.  For Figure 4.8 (b) the stiffest material allows the least penetration, and in Figure 4.8 (c), the stiffest material allows the most penetration.  Also, for these tests from the somewhat lower porosities, the penetration depths from the hammer drops for the specimen with 2.9 GPa and 9.0 GPa are almost similar. Table 4.1 summarizes these results.

From the simulations, the effect of the modulus of elasticity on the penetration depth is not very clear. In general it can be said that the effect of the modulus of elasticity on the penetration of DCP is not as significant as the surcharge load or particle shape. More simulations might be needed before getting well defined relationship between the penetration depth and the modulus of elasticity.
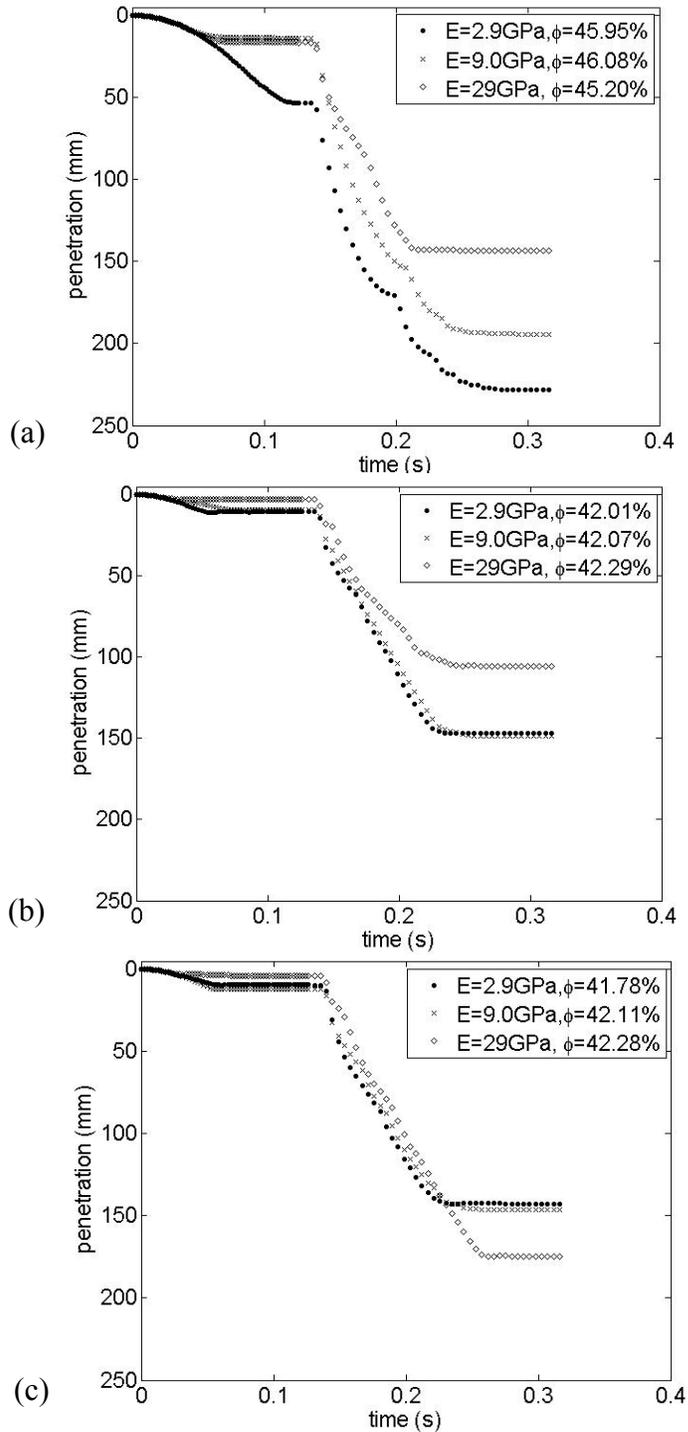
**Figure 4.8:** DCP test: modulus of elasticity. The three graphs show penetration of the DCP during placement and first hammer drop. The graphs show comparison of penetration depth for specimen with different modulus of elasticity (2.9, 9 and 29 GPa). The specimens comprise 2500 'couple' particles made by gluing 10 mm spheres. The porosity of each specimen is indicated in the legend.

58

**Table 4.1:** Results from multiple DCP tests for different moduli of elasticity and different porosities as shown. All results are for 2500 'couple' particles made by gluing 10 mm spheres. Results are shown graphically in Figure 4.8.

| Test Set | φ | E (GPa) | Penetration due to placement (mm) | Additional penetration due to hammer drop (mm) |
|---|---|---|---|---|
| 1 | 0.46 | 2.9 | 53.3 | 175.1 |
| 1 | 0.46 | 9 | 13.7 | 180.7 |
| 1 | 0.45 | 29 | 11.3 | 127.1 |
| 2 | 0.42 | 2.9 | 10.9 | 136.2 |
| 2 | 0.42 | 9 | 9.3 | 139.7 |
| 2 | 0.42 | 29 | 2.6 | 103.1 |
| 3 | 0.42 | 2.9 | 9.5 | 133.5 |
| 3 | 0.42 | 9 | 12.3 | 134.3 |
| 3 | 0.42 | 29 | 3.9 | 171.0 |

These results show that, for the DCP test, E seems to have less importance compared with the variation of either the porosity (investigated in the subsequent section) or some other detail of the system configuration. The modulus of elasticity describes how much a particular material deforms when subjected to stress, but apparently quantities like local packing and particle arrangement may be more relevant in determining resistance to penetration. This will be commented on in more detail in Chapter 6.

*4.2.5   Porosity*

The graphs in Figure 4.9 contain the same data as that of Figure 4.8 but rearranged to compare effect of porosity on DCP results for specimens with similar material property.
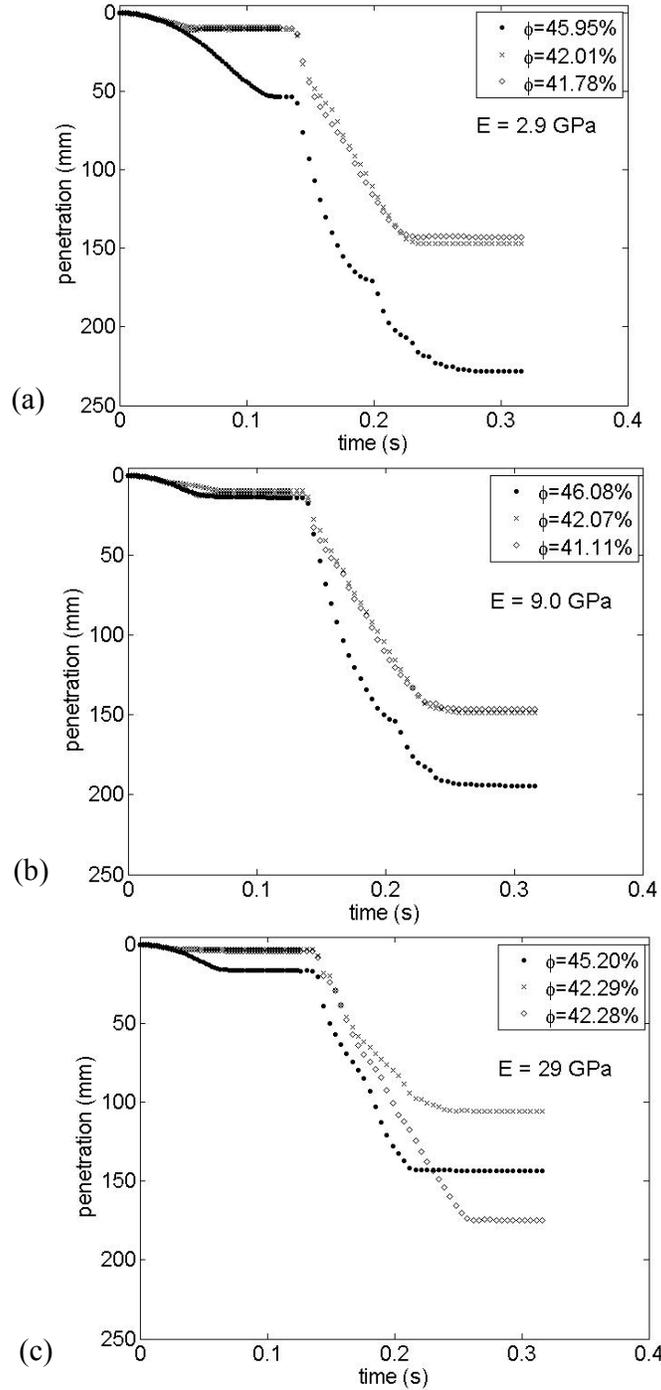
**Figure 4.9:** DCP simulation: porosity. The three graphs show penetration of the DCP during placement and first hammer drop. The specimens comprise 2500 'couple' particles made by gluing 10 mm spheres. (a) For E = 2.9 GPa. (b) For E = 9.0 GPa (c) For E = 29 GPa. The three curves on each graph represent specimen with different particle modulus of elasticity (2.9, 9 and 29 GPa). The porosities of the specimen are shown in the figures' legend.

60

For the specimens with particles moduli of elasticity of 2.9 and 9 GPa, shown in Figures 4.8(a) and 4.8(b) respectively, the DCP penetrated more for specimens with higher porosity. In other words, the depth of penetration increases with the porosity of the specimen; not surprising given that a higher porosity involves more openings for the cone to penetrate or to push interfering particles into as it drops down. However, the last graph, Figure 4.8(c), which contains results for particles with the modulus of elasticity of 29 GPa, shows somewhat different results. The penetration for the 42.28% porosity is greater than the penetration for the specimens with porosities of 42.29% and 45.20%. This deviates from the results for the other specimen. The large difference between the results of the specimen with 42.28% porosity and 42.29%might simply indicate an anomaly in how the specimen with 42.28% was prepared. Considering this, it would be useful to quantify initial preparation conditions beyond porosity, a task for the future.

*4.2.6   Container Size*

The DCP is a field test where there is no effective physical boundary. The test represents an 'infinite' or at least a very large number of particles. Performing an equivalently large-scale test computationally would be impractical due to the computational expense. Thus, for the tests described in this report, the number of particles used in the simulation was limited with the intent that the specimen size does not affect the qualitative test results so that computation can be done in a reasonable amount of time.

In this section, the effect of the size of the specimen on the penetration depth is discussed by comparing test results from different sizes of specimen. Both the height of the sample and the diameter of the container were considered. As discussed in Chapter 2 the container walls have the same physical property as the particles. DCP simulations were performed done for specimen with different filling heights and container diameters.

Figure 4.10 shows penetration during placement DCP for different sizes of the containers. The minimum container diameter was 90 mm and it was increased by a step size of 10 mm for the other tests. The simulations were performed for specimens with a size distribution of 10%: 60%: 30% 19 mm: 9.5mm: 4.75 mm. The material properties of the particles are E = 29 GPa, ν = 0.15, μ= 0.5 and ρ = 2650 kg/m$^3$. The table on the right shows the diameter of the container, the number of particles and the porosity for each specimen. It should be noted that the porosity was found to increase slightly as the diameter is increased; however, the differences in the porosity of the specimens were negligible as shown in Figure 4.10. More penetration depths were observed for bigger container diameter, though the difference appears negligible as the container diameter is increased from 100 mm to 110 mm. The speculation for this observation is that the side walls play role in resisting the penetration, but the importance decreases for larger system diameters. In all cases the depth of the system was approximately 175 mm.

| Spec | Dia. (mm) | No of particles | Porosity (%) |
|------|-----------|-----------------|--------------|
| 1 | 90 | 5000 | 37.89 |
| 2 | 100 | 5916 | 38.49 |
| 3 | 110 | 7106 | 38.60 |
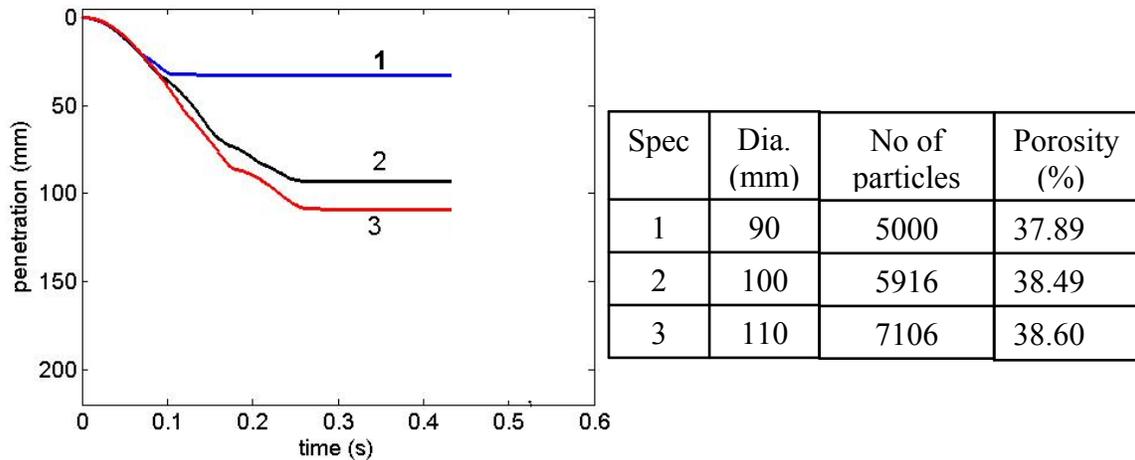
**Figure 4.10:** DCP test: container diameter. The figure shows the penetration depths for specimens in three different containers during placement of the DCP. The container size, the number of particles and the porosity of each test is shown in the table. The DCP penetrated more depth for the container with larger diameter. As described in the text, the specimens were comprised of 5000 particles with 10%: 60%: 30% 19 mm: 9.5 mm: 4.75 mm. The fill height was kept roughly constant, approximately 174 mm.

Figure 4.11 shows test results when the container diameter was kept constant at 90 mm, and filled with the same granular mixture as in Figure 4.10 for different fill heights of the container. This figure shows the penetration that occurred during the placement of the DCP cone for different filling heights. The table in Figure 4.11 shows the filling height, the number of particles and the porosity for each specimen. Again, the porosities for the specimens are almost equal. The number of particles for the first specimen was 5000. The number of particles was increased by 10% for consecutive simulations, and the fill height increased by approximately the same amount. The container for each simulation has a diameter of 90 mm. More penetration depths were observed as the filling height is increased. However, there is almost no difference in penetration depths for filling heights of 205 mm and 222 mm indicating this may be a sufficient depth for no size effects to be felt.

These results indicate a small exploration into the effects of the height and diameter of "container" on DCP test results, though more tests clearly need to be performed to determine whether these trends are completely reliable. In particular, additional tests need to be performed to see if the limiting depth (above which no size effects are observed) is dependent on the diameter of the container and the limiting diameter (above which no size effects are observed) is dependent on the depth of the sample.
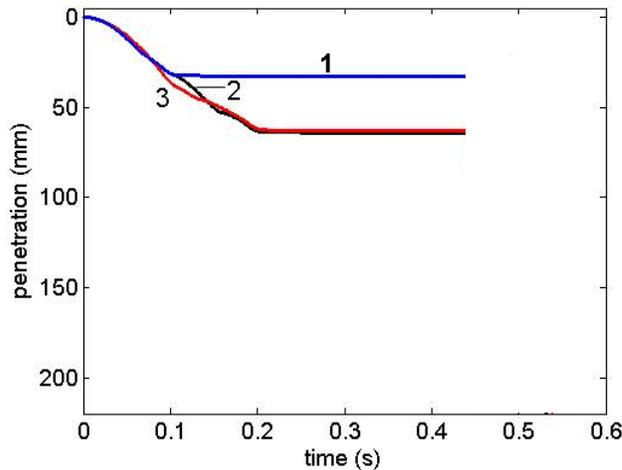
| Spec. | Height (mm) | No of Particle | Porosity (%) |
|-------|-------------|----------------|--------------|
| 1 | 182.0 | 5000 | 37.89 |
| 2 | 205.8 | 5500 | 39.61 |
| 3 | 222.0 | 6050 | 38.45 |

**Figure 4.11:** DCP test: height of specimen. The figure shows the penetration depths for specimen in three different specimens during placement of the DCP. The container size, the number of particles and the porosity of each test is shown in the table. The DCP penetrated more depth for the container with larger diameter.

### 4.2.7   Comparison with Field Test Results

For practitioners of typical materials used in pavements, the depth of penetration for the DCP simulation results presented above appears very large. This is mainly due to "open graded" nature of the material, that is, the presence of only large particle and lack of particles of smaller sizes in the granular mix.  Though the computational results cannot be compared directly to many of the field experiments, they can be qualitatively compared to experimental data from physical open graded systems. Experimental results by Ford and Eliason [14] for DCP test in narrow granular-backfilled trenches provide a good set for comparison.  These DCP field tests were performed to compare the depth of penetration for different level compaction of sand.

Table 4.2 shows depths of penetration of the DCP in millimeters during placement and first hammer drop for granular backfill material with different levels of compaction from Ford and Eliason [14].  The tests in this reference were not calibrated to give strength or density of the material, but rather to provide a relative indication of the compaction in the backfill sand. For this particular test, the specimen is a mix of particles with the size parameters $D_{50}$ of 1.2 mm and $D_{90}$ of 5 mm. The DCP penetrated the whole depth of the trench for the poorly compacted granular material during placement. The penetration decreased as the compaction level of the sand was increased. Though this cannot be compared directly to the results from the simulation, it indicates that the higher magnitudes of penetration are reasonable.

63

**Table 4.2:** DCP test for granular particle. The table shows penetration depths from a DCP test during placement and hammer drop from experiments conducted by Ford and Eliason [14]. The penetrations depths are given in mm. The test was conducted on granular materials, which have different compaction levels. The granular materials have a $D_{50}$ = 1.2 mm and $D_{90}$ = 5 mm. The trench has a depth of 300 mm

| Trench Depth (mm) | DCP Test | No Comp | Poorly Comp | Well Comp |
|---|---|---|---|---|
| 300 | Placement | 300 | 50 | 60 |
|  | 1st Drop | - | 300 | 100 |
| 600 | Placement | 600 | 50 | 60 |
|  | 1st Drop | - | 600 | 100 |
| 900 | Placement | 900 | 75 | 75 |
|  | 1st Drop | - | 900 | 110 |

### 4.2.8   Summary of Results from the DCP Simulations

The model described in this chapter, which was developed to simulate the physical DCP test, showed that several factors affect the depth of penetration of the DCP. Significant factors include the sphericity of the particles and the surcharge load. The penetration depth decreases significantly when aspherical particles are used and/or when the amount of surcharge load increases. The depth of penetration decreases as the coefficient of contact friction is increased. However, there is no significant change for coefficient of contact friction beyond 0.5. The effect of particle modulus of elasticity is not clear from the simulations but it seems that it is minor compared with other effects such as porosity and interparticle structure. The size of the "container" also has some effect on the results from the DCP simulation and needs to be investigated more thoroughly to fully quantify the possible interdependent effects of diameter of container and sample depth.

# Chapter 5
# Comparison of Tests

As discussed in Chapter 1, several researchers have attempted to develop direct correlations between results from different tests of unbound materials such as the MR test and the DCP tests. Verification of these empirical correlations or investigation of other possible relationship between different tests is still a major challenge for the pavement community. In order to correlate test results, the factors affecting each test should be identified carefully. This Chapter presents summary of the comparison of the numerical model results. Also included in this Chapter is a preliminary physics-based analysis of the force distribution in the granular ensembles.

## 5.1 Comparing the Sensitivity to Different Parameters

From the simulations presented in the previous chapters of this report it was observed that the depth of penetration per blow in the DCP test largely depends on the surcharge load and the shape of the particles. The surcharge load, which is the load at the top surface of the specimen, decreases the depth of penetration significantly. In addition, for aspherical shapes, formed by gluing spherical particles together, the depth of penetration is reduced by higher magnitude compared to specimen with spherical particles. The coefficient of contact friction plays an important role in reducing the depth of penetration. However, this is true up to contact friction value of 0.5; beyond this value the coefficient of friction has no noticeable effect on the depth of penetration. The effect of the modulus of elasticity of particles on the penetration depth is not clear from these simulations. The penetration depth tends to reduce as the modulus of elasticity is increased. But more simulations are required before asserting any conclusion.

On the other hand, the resilient modulus of granular materials depends on the modulus of elasticity of the particles. The MR increases linearly with the modulus of elasticity of particles. The MR also increases with increase in the applied stress. The MR increases more with increase in the confining pressure than it does with the increase of the deviator stress. The MR also increases as a power law function of the bulk stress, which is the sum of three times the confining pressure and the deviator stress. The size of the particles in the specimen is an important factor that will determine test results. As the size of the particles is increased the MR showed higher variations.

These results bring to question any single relationship designed to relate resilient modulus results to DCP results. For example, considering the effects of the Young's modulus on the DCP results and MR results yields very different conclusions. Changing the Young's modulus of the material has a very direct, systematic, measurable effect on the MR results. An analogous relationship does not appear to exist for the DCP results. This indicates that one might need different quantitative ways to relate the DCP and MR test results, depending on the type of material used.

While these results may have very practical implications on current pavement design practices, they also raise interesting scientific questions. Specifically, the different tests appear to represent fundamentally different loading conditions for the granular materials. The nature of these differences has not been investigated. In the next section, the interparticle forces for different tests and their apparent structure throughout the materials when subjected to the different types of loading are evaluated.


## 5.2 Quantitative Comparisons: Force Distributions

To understand the physics behind apparently different test results, some researchers have performed experiments to investigate the affect of different types of loading on the contact forces between particles. Towards this, special types of photo-elastic particles have been used to visualize the interparticle contact forces [55]. Some early research have tried to look into the formation of what was called 'force lines' inside granular ensembles – discrete connections by which forces are non-homogenously distributed in a granular material – by using photo-elastic disks. Drescher and De Jong [56] may have been the first to use photo-elastic cylindrical rods to analyze how the stress is transferred inside the ensemble when it is subject to external loading. They observed 'force lines' that might elongate (include more particles), thicken (carry more stress) or break (come apart) during the application of continuous loading. Others have tried to use these experimental results to develop a statistical description of the contact forces. Mueth et al [57] used photo-elastic particles to study the distribution of normal forces in a uni-axial compression test. They studied the contact forces at the bottom and top lid cover of the specimen. They found that the probability distribution function (PDF) for these normal forces followed an exponential decay at forces that were larger than the average force as in Figure 5.1(a). More recently, Majmudar and Behringer [55] have shown that the shape of the PDF of the interparticle contact forces varies for different loading conditions (Figure 5.1). Majmudar and Behringer [55] used photoelastic cylindrical rods in two different types of tests, an isotropic compression test and a simple sheared system. They found that the PDF of the normal force in pure shear system follows an exponential decay (Figure 5.1(a)). However, the PDF for isotropic compression tests is more rounded; i.e. the PDF is flat near the average normal force and decays quickly (Figure 5.1(b)).
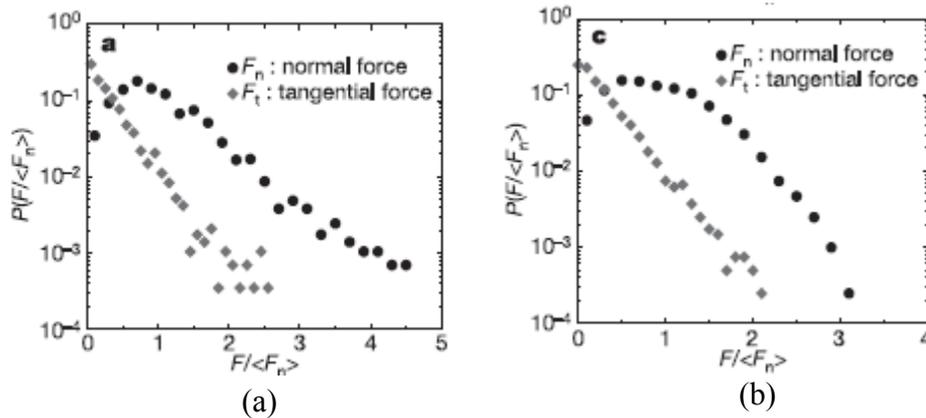
**Figure 5.1:** Force distribution [55]. (a) Probability distributions of the normal ($F_n$) and the tangential ($F_t$) forces for the sheared system on a semi-log scale. (b) Probability distributions of the normal and the tangential forces for the isotropically compressed system on a semi-log scale.

Even with these techniques complete analysis of the forces cannot be performed using experimental methods. The main draw back for these types of experiments is lack of efficient method to measure the contact forces that are 'buried' or covered by the other particles in a fully 3-D system. Many of the studies described above were limited to 2-D experiments using cylindrical rods or to the contact forces that are near the walls where measurements can be taken easily. DEM provides a perfect setting for determining more details of the contact forces in a fully 3-D system. The contact forces can be determined from the simulation independent of its location and magnitude. Majmudar and Behringer [55] also used DEM method to analyze the contact forces. The PDFs from the simulations and experiments are similar, although with the DEM it was possible to measure even small contact forces.

For this report, some statistical analysis of the contact forces were performed for the three types of tests described in Chapter 2-4. 'Instantaneous' probability distribution functions of the normal and tangential forces were computed for each test. The results are shown in Figure 5.2 -5.6. In these figures every contact force was normalized by the average of the normal forces. Then, the PDF's were prepared on a semi-log scale. In addition, images were prepared for each simulation that shows the magnitude of the summation of forces on each particle. This assists in qualitatively identifying those particles which bear most of the applied stresses. Figure 5.2 shows a picture prepared during the penetration of the plunger for the CBR test. The intensity of the color represents the sum of the normal forces on a particular particle. From this figure it is clear that the applied stress is distributed relatively inhomogeneously through the granular materials.

Figure 5.3 shows the PDF of normalized normal force for the CBR test. Figure 5.3(a) shows the normal force distribution after the plunger has penetrated 3 mm. Figure 5.3(b) shows the normal force distribution after the plunger penetrated 12.5 mm. In both cases the PDF follows exponential decay with longer tail. This is similar to the PDF of the simply sheared system from sheared system of Majmudar and Behringer [55].
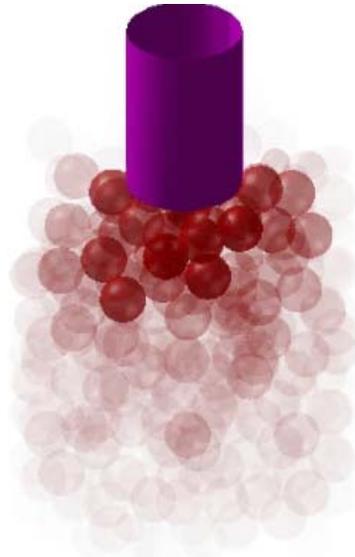
**Figure 5.2:** Inter-particle force distribution during a CBR test. The figure shows the summation of the normal forces on the each particle. The color intensity indicates the relative magnitude of the forces.



(a)                              (b)
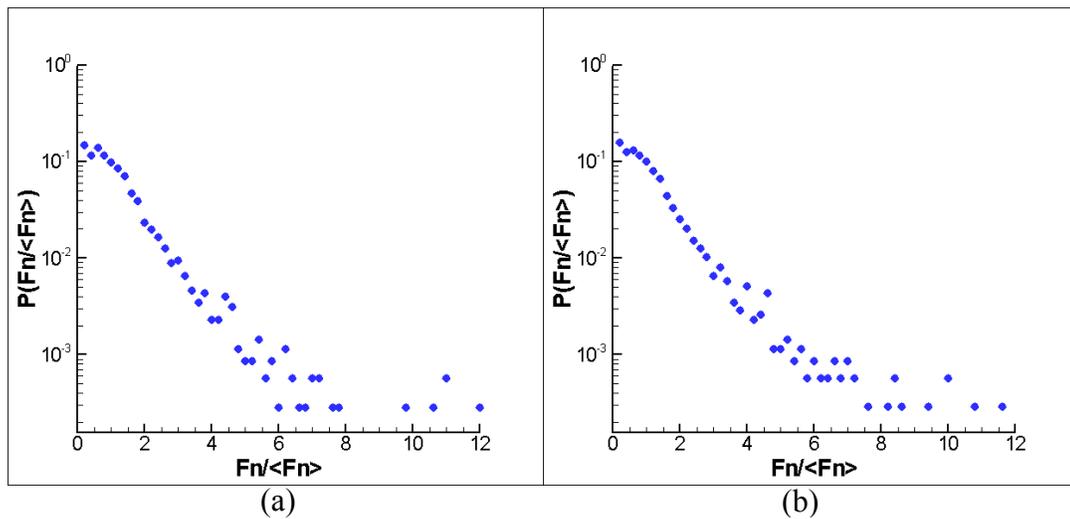
**Figure 5.3:** Normal force distribution CBR test. (a)Probability density function (PDF) of the normal forces $(F_n)$ for the CBR test at 3 mm of plunger penetration. The forces are normalized by the average normal force $<F_n>$. (b) PDF of $F_n$ at 12.5 mm of plunger penetration.

Figure 5.4 shows magnitude of all forces on the particles for the MR test. The intensity of the color of the particles in the figures indicates the magnitude the summation of the normal forces on the particles normalized by the maximum summation of the normal forces on a particle in the whole system during the maximum deviator load. Figure 5.4(a) shows the summation of forces

during the rest period, when there is no application of deviator load, and Figure 5.4(b) shows the summation of forces during the application of the maximum deviator stress. Though the magnitudes of the forces on the particles are noticeably higher during the application of the maximum deviator stress, they are more uniformly distributed in this test than the CBR test. This is also demonstrated by the PDF plot in Figure 5.5. The graphs show the PDF of normalized normal force for the MR test: (a) shows normal force distribution during rest period and (b) shows the PDF during the application of the maximum deviator load. In both cases, the contact forces are normalized by the average normal contact force. The PDFs are flat near the average force and converges to zero quickly. This indicates that the range of the magnitude of the normal forces is very narrow and most of the particles experience almost equal amount of stress. The force distribution for the MR test is similar to the isotropic compression tests in Majmudar and Behringer [55].



(a)                                                           (b)
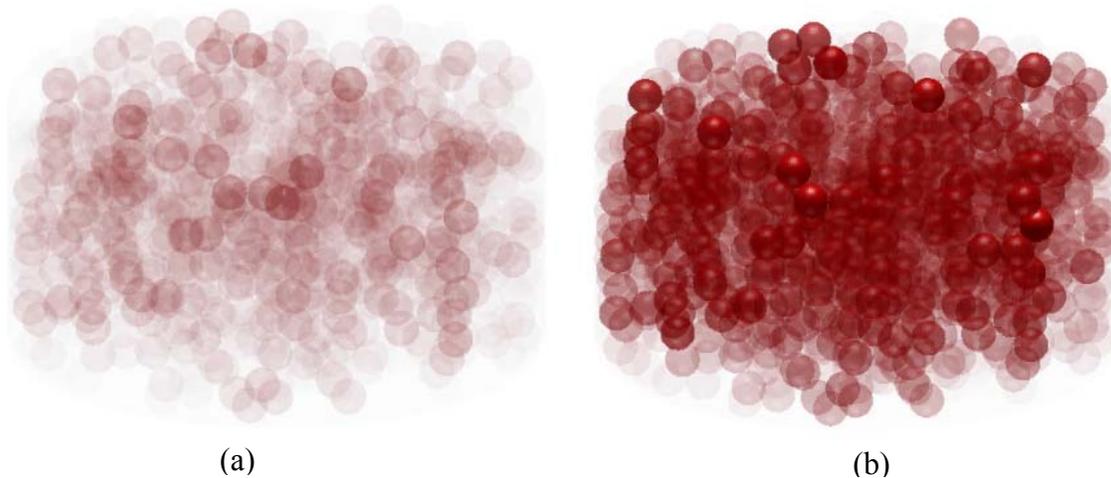
**Figure 5.4:** Inter-particle force distribution for MR test. The figure shows the summation of the normal forces on the each particle. The color intensity indicates the relative magnitude of the forces. (a) shows the magnitude of force during the rest period. (b) shows the magnitude of the force during the maximum deviator stress.
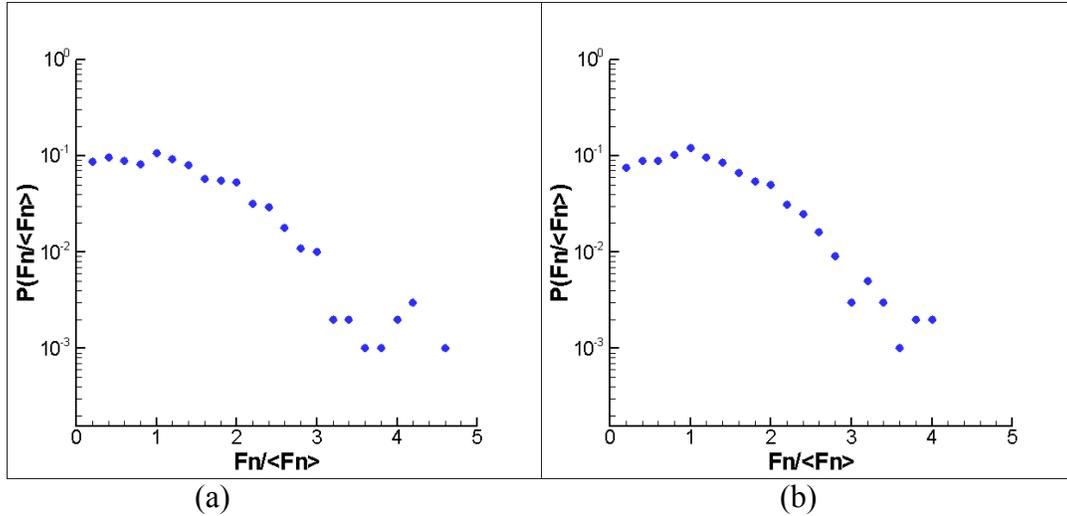
**Figure 5.5:** Normal force distribution for MR test. (a) Probability distributions (PDF) of the normal forces ($F_n$) during rest period. The forces are normalized by the average normal force $<F_n>$. (b) PDF of the $F_n$ during the maximum applied deviator stress.

Figure 5.6 shows the PDF of normalized normal force for the DCP test. The first graph shows the PDF during hammer drop and the second graph was produced by zooming in on the graph shown in Figure 5.6(a). As for the CBR test, the PDF follows an exponential decay. There are few contacts where the normal force is much higher than the average. In their DEM model for a static cone penetrometer, similar to the dynamic cone penetrometer except that the apparatus is pushed at a constant speed, Jiang and Yu [26] observed that the stress distribution in the area near the penetrometer is significantly different than that for the bulk of the material. The maximum stress occurs near the tip of the cone with the principal stress perpendicular to the tip. In the area far from the DCP, this effect is very small, and the principal stress is controlled by the gravity force.
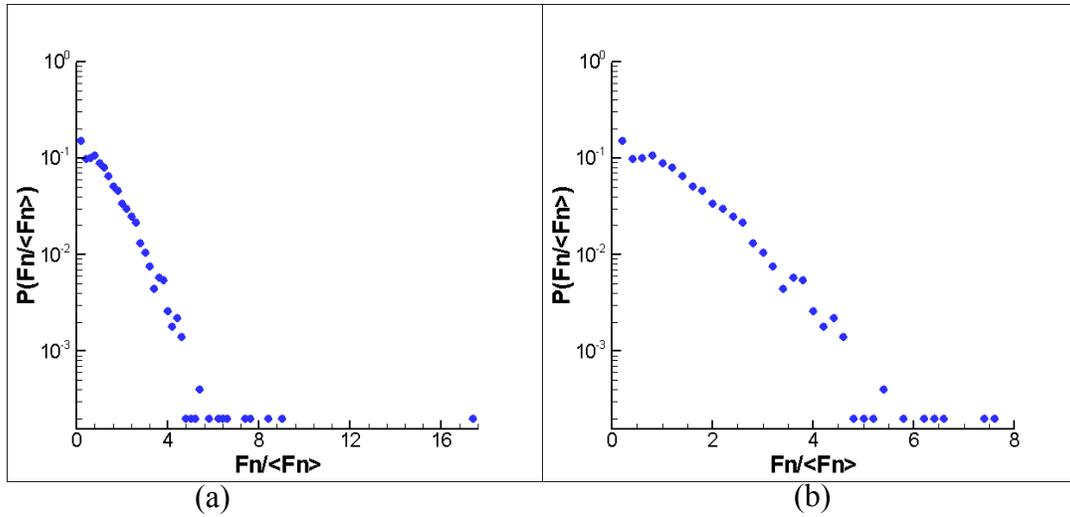
**Figure 5.6:** Normal force distribution DCP test. (a) Probability distributions of the normal ($F_n$) forces on a semi-log scale. The forces are normalized by the average normal force $\langle F_n \rangle$. (b) Zoom in of (a).

Figure 5.7- Figure 5.9 show the normalized tangential force distribution for the CBR, MR and DCP tests respectively. The tangential part of the interparticle forces is normalized by the average of the normal part of the interparticle forces as in Majmudar and Behringer [55]. This was done to compare the magnitudes of the normal and tangential forces in the same scale. The tangential force distributions also follow similar trend as the PDF of the normal force. However, the magnitude of the tangential force is lower than the magnitude normal forces. This is especially notable for the tangential forces in the MR test. The tangential forces for the MR test are about 5 times lower than the normal forces.
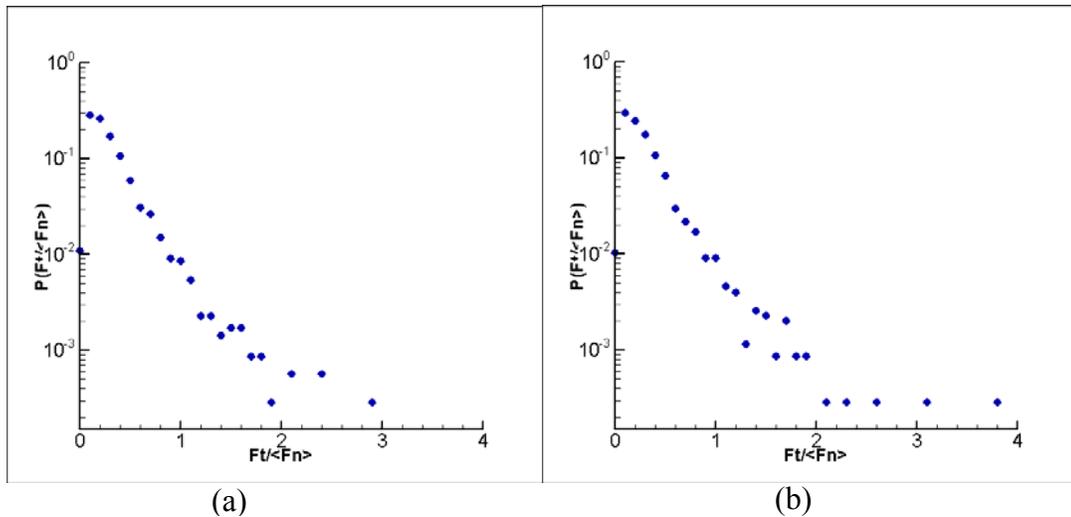


**Figure 5.7:** Tangential force distribution for CBR test. (a) Probability distributions of the tangential forces ($F_t$) at 3 mm of plunger penetration. The forces are normalized by the average normal force $\langle F_n \rangle$. (b) PDF of $F_t$ at 12 mm of plunger penetration.

71

(a)               (b)
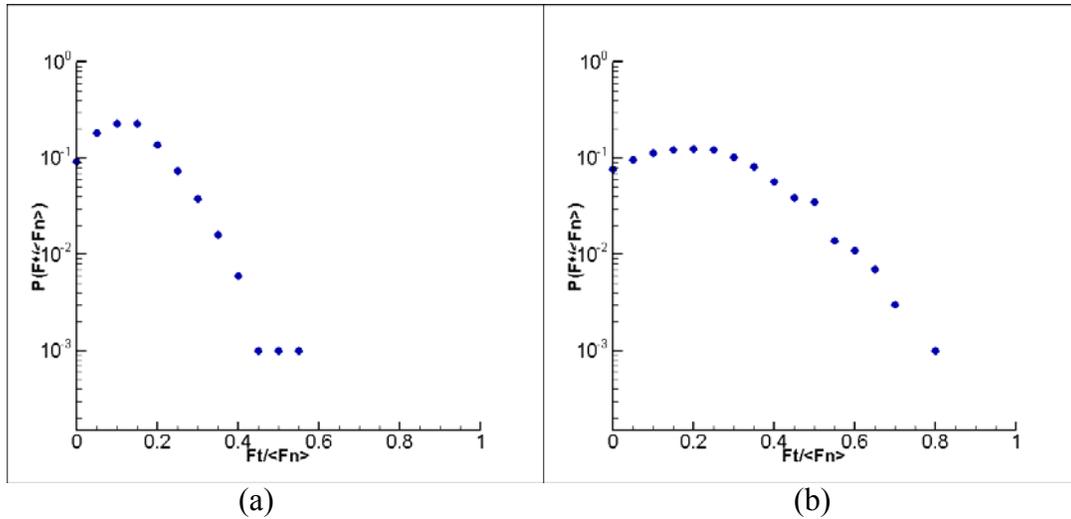
**Figure 5.8:** Tangential force distribution MR test. (a) Probability distributions (PDF) of the tangential force ($F_t$) during rest period. The forces are normalized by the average normal force $<F_n>$. (b) PDF of the $F_t$ during the maximum applied deviator stress.
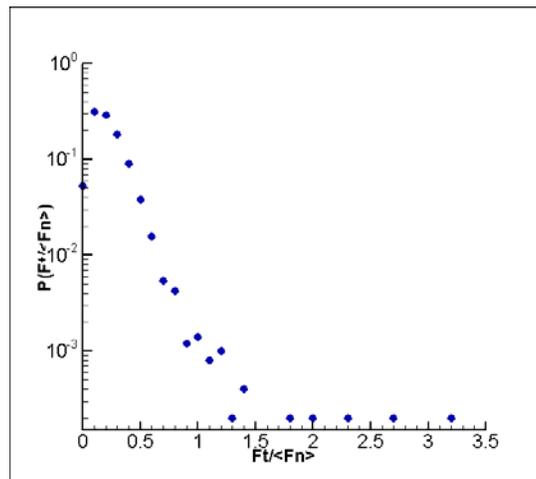


**Figure 5.9:** Tangential force distribution for the DCP test. The tangential force is normalized by the average normal force.

## 5.3 Summary: Test comparisons

In general, the models are capable of demonstrating key differences between the tests. Some of the factors that affect test results and the response of the granular material to these tests were identified. The factors that affect the test results include the particle physical properties such as modulus of elasticity, coefficient of friction, and shape. It is important to note that a physical

72

property that affects results of one test may not affect results from other tests in the same way. As noted, the penetration in the DCP test appears to depend most strongly on the shape of the particles and the coefficient of friction, while the MR test appears to depend most strongly on the modulus of elasticity of the particles. It should be noted, however, that no tests were performed using the MR test for aspherical particles. Finally, detailed statistical analysis of the contact forces reported in this chapter revealed somewhat different responses of the granular ensemble to different loading configurations.

# Chapter 6
# Summary

As described in Chapter 1, the aggregate base and granular subbase layers are important elements of a pavement system. Design of strong and economical roads requires good knowledge of the behavior of the materials used in these layers. This requires a good understanding of the granular materials. Towards this, DEM based models were developed and the existing models in the literature appear to well-represent real particles qualitatively.

The DEM code used in this study had the following features:
- Nonlinear particle interaction model for the contact forces. The coefficients of the interaction equations are linked to real physical properties as described by Tsuji et al. [44]
- Particle and wall properties that can be directly manipulated include the modulus of elasticity, Poisson's ratio, size of particles, and the coefficient of contact friction.
- Different shapes of non-spherical particles can be created using simple computational gluing of spherical particles.
- Particles were compacted by applying load at the surface, squeezing the lateral wall and reducing the contact friction simultaneously.

When this code was applied to a "base case" CBR test, the results were reasonably representative of a real physical test of granular materials. The following observations were made:
- The models demonstrated the resisting force on the penetration of the plunger increased as the penetration depth increased.
- The CBR(%) calculated from the CBR simulation on granular materials comprising 10 mm particles was within the expected range for granular particles in physical tests.

The DEM code was also used to model more complicated tests, namely the resilient modulus test and the Dynamic Cone Penetrometer (DCP) test. The resilient modulus test model has the following brief descriptors:
- The flexible rubber membrane was formed by connecting the centers of the particles that are touching it. Three centers of particles are connected such that a Delaunay Triangulation is formed.
- The container has a diameter of 150 mm and height of approximately 80 mm.

The results from the resilient modulus showed the following key dependencies:
- The resilient modulus (MR) increases linearly with the particle modulus of elasticity.
- The MR increases with the increase of the applied stresses. The increment is more for increase in the confining pressure than increase in the deviator load.
- The MR is almost constant for specimen comprising particle sizes lower than 10% of the container diameter. For particle sizes above 10% of the container diameter the MR significantly fluctuated.

Preliminary investigations show that the shape of particles does not have significant effect on the MR.

The DCP test had the following descriptors:
- The most important components of the DCP apparatus are
  - The cone which has base diameter of 20 mm and apex angle of $60^0$
  - The 8 kg hammer which is dropped onto the anvil from height of 575 mm.
- Surcharge load of specific amount was put on the top surface of the specimen to represent the depth the DCP had penetrated after seating drops and prior to the measurement drops.

The following particle properties were found to have influence on the DCP test results;
- The shape of the particles affects the depth of penetration per drop of the DCP. Less depth of penetration is observed for specimen composed of non-spherical particles.
- The depth of penetration also decreases with increase in the coefficient of contact friction. However increasing the coefficient of friction to more than 0.5 (or friction angle of 28.5°) has no effect on the depth of penetration.
- The modulus of elasticity of the particles has a minor effect on the depth of penetration, but the effect can not be well described as in the case of the MR test.
- Surcharge load, while not a property, is a significant factor that affects the depth of penetration per drop: more surcharge load results in lower penetration depth per drop.
- Size of the container or the specimen is another factor that affects the DCP test results.
  - The DCP penetrates more in larger diameter containers.
  - The DCP also penetrates more for a specimen with a greater height.
- As one might expect, the set-up of the specimen influences the outcome.
  - Porosity of the specimen controls the test result, such that more penetration per drop is incurred for higher porosity specimens.
  - Stiffness of particle during set-up influences the packing which ultimately influences the result of the tests.

With this in mind it is interesting to note some of the differences between the tests:
- DCP is highly dependent on shape of particles and surcharge and set-up
- MR is highly dependent on the modulus of elasticity of particles and applied stresses.

It was shown that some of these mechanical differences might be quantitatively illustrated using force distributions.
- The probability density functions (PDF) of the normal and tangential forces for the CBR test follow exponential function, which indicates that the stress from the plunger is carried mostly by the particles near the plunger.
- The PDF of the forces for the MR test is more rounded and converges very fast. This indicates that the force is carried more uniformly through the specimen.
- The PDF of the forces for the DCP test follows an exponential function, as in the CBR test.

Now, to put this in the context of some of the practical problems noted at the beginning of the report, it is helpful to consider the following limitations and challenges.

## 6.1 Limitations and Future Challenges

Although the test results and their predicted dependence on the particle properties show the potential of the DEM models, there are still many challenges that have to be overcome. One of the biggest challenges is the computation requirement for realistically bigger sample size. Some researchers have attempted to overcome this by reducing the dimension of the problem into 2-D systems [31, 33, 34]. However, 2-D systems do not produce quantitatively or qualitatively accurate results. Therefore, it is important to maintain the 3-D nature of the model. The best way to tackle computational time requirement is to develop an efficient parallel DEM code. As described in Chapter 2, the parallel code written using the MPI showed very good promise. With more efficient parallel codes, the computation time can be decreased significantly.

The models presented in the report are designed for drained samples, which do not contain free water on the surface. During actual construction projects, presence of free surface water has a significant impact on the behavior of the aggregates. The effect of moisture content becomes more essential to model cohesive and fine soil particles. Therefore, an important next step is to include moisture in DEM models as in Refs [12, 58]. The details of DEM models and initial investigation for granular material with moisture content are presented in Appendix B.

In addition to these challenges, some particle physical parameters and specimen preparation procedures need to be quantified. As mentioned in Chapter 4, though the effect of particle shape on the penetration of the DCP is quite clear, it has not been described quantitatively. More investigation should be done to quantify different particle shapes and their effect on the characteristics of granular material. During this research some variation on results were observed for specimens comprising the same type of granular particles but which are prepared using different techniques. The effect of the initial conditions and configurations on test results should be quantified as well.

The DEM models in this report were capable to demonstrate significant effects of basic particle material properties and boundary conditions on test results. While more work is needed to fully develop a mechanistic based model for tests of unbound material, the model described in this report serves as a strong foundation for future work in this field [59, 60].

# References

1. I. Jumo and J. Geldenhuys (2004). "Impact Compaction of Subgrades - Experience on the Trans-Kalahari Highway Including Continuous Impact Response (Cir) as a Method of Quality Control" Proceedings of the 8th Conference on Asphalt Pavements for Southern Africa, Sun City, South Africa.

2. Association of State Highway and Transportation Officials (1972). *AASHTO Interim Guide for Design of Pavement Structures*, American Association of State Highway and Transportation Officials, Washington, D.C.

3. Association of State Highway and Transportation Officials (1986). *Guide for Design of Pavement Structures*, American Association of State Highway and Transportation Officials, Washington, D.C.

4. Association of State Highway and Transportation Officials (1993). *Guide for Design of Pavement Structures,* American Association of State Highway and Transportation Officials, Washington, D.C.

5. Transportation Research Board (Internet), (2002). *Mechanistic Empirical Design Guide,* Accessed May 5 2008, www.trb.org/MEPDG.

6. W.R. Barker and C.R. Gonzalez (2006). "Renovation of the CBR Design Procedure," Second International Airports Conference: Planning, Infrastructure & Environment. São Paulo, Brazil.

7. American Society for Testing and Materials (2007). *Standard Test Method for CBR (California Bearing Ratio) of Laboratory-Compacted Soils, ASTM D1883-07*, American Society for Testing and Materials, West Conshohocken, PA.

8. S.S. Razouki and A.M. Al-Shefi (2002). "Effects and Observations of Surcharge Load on the Laboratory CBR and Resilient Modulus Values of Roadbed Soil," *Journal of Engineering Geology and Hydrogeology*, Vol. 35, 89–95

9. Association of State Highway and Transportation Officials (1999). *Standard Method of Test for Determining the Resilient Modulus of Soils and Aggregate Materials, AASHTO T307,* American Association of State Highway and Transportation Officials, Washington, D.C.

10. National Cooperative Highway Research Program (2002). *Recommended Standard Method for Routine Resilient Modulus Testing of Unbound Granular Base/Subbase Materials and Subgrade Soils, Protocol 1-28A*, National Cooperative Highway Research Program, Washington, D.C.

11. J.E. Herrick and T.L. Jones (2002). "A Dynamic Cone Penetrometer for Measuring Soil Penetration Resistance," *Soil Sci. Soc. Am. J.*, Vol. 66, 1320–1324.

12. P. Davich, F. Camargo, B. Larsen, R. Roberson, and J. Siekmeier (2006), *Validation of DCP and LWD Moisture Specifications for Granular Materials,* Minnesota Department of Transporation, St. Paul, Minnesota

13. American Society for Testing and Materials (2003). *Standard Test Methods for use of the Dynamic Cone Penetrometer in shallow pavement application, ASTM D6951-03,* American Society for Testing and Materials, West Conshohocken, PA.

14. G.R. Ford and B.E. Eliason (1991). *Comparison of Compaction Methods in Narrow Subsurface Drainage Trenches,* Minnesota Department of Transportation, St. Paul, MN.

15. W. Heukelom and A.J.G. Klomp (1962). "Dynamic Testing as a Means of Controlling Pavement during and after Construction," Proceedings of the 1st international conference on the structural design of asphalt pavement, University of Michigan, Ann Arbor, MI.

16. W.D. Powell, J.F. Potter, H.C. Mayhew and M.E. Nunn (1984). *The Structural Design of Bituminous Roads,* TRRL Laboratory Report LR 1132, Transport and Road Research Laboratory, Crowthorne, United Kingdom, 1984

17. Webster S. L., R. H. Grau, and R. P. Williams (1992). *Description and Application of Dual Mass Dynamic Cone Penetrometer,* Instruction Report GL-92-3, U.S. Army Corps of Engineers Waterways Experiment Station, Vicksburg, MS.

18. M. Livneh (1991). "Verification of CBR and Elastic Modulus Values from Local DCP Tests," Proc. 9th Asian Regional Conf. on Soil Mechanics & Foundation Engineering, Bangkok, Thailand, vol.125, no., 1, 45-50.

19. M.R. Thompson and Q.L Robnett (1979). "Resilient Properties of Subgrade Soils," *J. of Transportation Engineering*, vol. 105, no. 1, 71-89.

20. B. Sukumaran, V. Kyatham, A. Shah and D. Sheth (2002). "Suitability of Using California Bearing Ratio Test to Predict Resilient Modulus," Federal Aviation Administration Airport Technology Transfer Conference, Atlantic City, NJ.

21. D. Kim and N. Siddik (2005). *Simplification of Resilient Modulus Testing for Subgrades,* INDOT, Indianapolis, IN.

22. K. Hibbitt and I. Sorensen (2001). *ABAQUS User's Manual: Version 6.3*, Hibbitt, Karlsson & Sorensen Inc., Pawtucket, Rhode Island.

23. P.A. Cundall and O.D.L. Strack (1979). "A Discrete Numerical Model for Granular Assemblies," *Geotechnique,* vol. 29, no.1, 47-55.

24. H. Tanaka, M. Momuzu, A. Oida and M. Yamazaki (2001). "Simulation of Soil Deformation and Resistance at the Bar Penetration by the Distinct Element Method," *J. Terramechanics*, vol. 37, 41-56.

25. T.C. Ke and J.D. Bray (1995). "Modeling of Particulate Media using Discontinuous Deformation Analysis," *J. Eng. Mech*, vol. 121, no. 11, 1234-43.

26. M. Jiang and H. Yu (2006). "Application of Discrete Element Method to Geomechanics," *Modern Trends in Geomechanics*, vol. 106, 241-269.

27. P.A. Thomas and J.D. Bray (1999). "Capturing Nonspherical Shape of Granular Media with Disk Clusters," *J. Geotech. and Geoenv. Eng.*, vol. 125, no. 3, 169-178.

28. J.M. Ting, L. Meachum and J.D. Rowell (1995). "Effect of Particle Shape on the Strength and Deformation of Mechanism of Ellispse-Shaped Granular Assemblages," *Engineering Computations*, vol. 12, 99-108

29. J.P. Bardet and J.A. Proubet (1991). "A Numerical Investigation of the Structure of Persistent Shear Bands in Granular Media," *Geotechnique*, vol. 41, no. 4, 599-613.

30. M. Kuhn (1995). "A Flexible Boundary for the Three-Dimensional DEM Particle Assemblies," *Engineering Computations*, vol. 12 no. 2, 175-183.

31. J. Williams and R. Nabha (1997). "Granular Vortices and Shear Band Formation," *Mechanics of Deformation and Flow of Particulate Materials*, pp. 62-71.

32. T.T. Ng (2004). "Triaxial Test Simulation with Discrete Element Method and Hydrostatic Boundaries*," J. Eng. Mech*., vol. 130, no. 10, 1188-1194.

33. P. Ullidtz (2001). "Distinct Element Method for Study of Failure in Cohesive Particulate Media," *Transportation Research Record*, no. 1757, 127-133

34. M. Zeghal (2005). "Discrete-Element Method Investigation of the Resilient Behavior of Granular Materials," *J. Transportation Engineering*, vol. 130, no. 4, 503-509.

35. R. G. Hicks and C. L. Monismith (1971). "Factors Influencing the Resilient Response of Granular Material," *Highway Research Record*, No. 345, 15-31.

36. W. Khogali and M. Zeghal (2003). "A Comprehensive System for Characterizing Granular Materials: Providing Material Input for Pavement Design," Annual Conference of the Transportation Association of Canada, St. John's, Newfoundland and Labrador.

37. J**.** Zhang (2008). "Kinematics and Kinetics of Granular Mixture: Experimental and Numerical Studies," PhD Dissertation, University of Illinois at Urbana-Champaign, Urbana-Champaign, IL.

38. K.M. Hill and J. Zhang (2008). "Kinematics of Densely Flowing Granular Mixtures," *Physical Review E*, vol. 77, 061303.

39. T.T. Ng and C.W. Wang (2001). "Comparison of 3D DEM simulation with MRI data," *Int. J. for Numerical and Analytic Methods in Geomechanics*, Vol. 25, 497-507.

40. M. Allen (2004). "Introduction to Molecular Dynamics Simulation*," Computational Soft Matter: From Synthetic Polymers to Proteins, Lecture Notes,* vol. 23, 1-28.

41. A.B. Stevens and C.M. Hrenya (2005). "Comparison of Soft-sphere Models to Measurements of Collision Properties during Normal Impacts," *Powder Technology*, vol. 154, 99-109.

42. R. Garcia-Rojo, S. McNamara and H.J. Herrmann, (2008). "Influence of Contact Modeling on the Macroscopic Plastic Response of Granular Soils under Cyclic Loading," *Mathematical models of Granular matter,* 109-123.

43. Y. Tsuji, T. Tanka and T. Ishida (1992), "Lagrangian Numerical Simulation of Plug Flow of Cohesionless Particles in a Horizontal Pipe," *Powder Technology*, vol. 71, 239-250.

44. R.D. Mindlin and H. Deresiewicz (1953). "Elastic Spheres in Contact under Varying Oblique Forces," *J. Applied Mechanics*, vol. 20, no. 3, 327-44.

45. A. Munjiza (2004). *The Combined Finite-Discrete Element Method*, John Wiley & Sons Inc., West Sussex, England.

46. J.A. Ferrez and T.M. Liebling (2002). "Robust 3D Dynamic Triangulations for Collision Detection in DEM Simulations of Granular Materials," *Supercomputing Review*, No.13, 41-48.

47. T.T. Ng and R. Dobry (1992). "A Numerical Simulation of Monotonic and Cyclic Loading of Granular Soil," *J. Geotechnical Engineering*, vol. 120, no. 2, 388-403.

48. M. Zeghal (2001). "Effect of Particle Shapes on the Resilient Behavior of Aggregate Materials," Canadian Society of Civil Engineering Annual Conference, Victoria.

49. S.J. de Vet and J.R. de Bruyn (2007). "Shape of Impact Craters in Granular Media," *Physical Review E*, vol. 76, 041306.

50. F. Cardarelli, (2008). *Materials Handbook*, Springer Publishing Company, New York, NY.

51. Federal Aviation Administration (1995). *Airport Pavement Design and Evaluation,* Federal Aviation Administration, Washington D.C.

52. George, K. P. (2004). *Prediction of Resilient Modulus from Soil Index Properties,* Mississippi Department of Transportation, Jackson, MS.

53. G. Leach (1992). "Improving Worst-Case Optimal Delaunay Triangulation Algorithms," 4th Canadian Conference on Computational Geometry, St. John's, Newfoundland.

54. R. Gudishala (2004). "Development of Resilient Modulus Prediction Models for Base and Subgrade Pavement Layers from in Situ Devices Test Results," MS thesis, Louisiana State University Baton Rouge, LA.
.
55. T.S. Majmudar and R.P. Behringer (2005). "Contact Force Measurements and Stress-Induced Anisotropy in Granular Materials," *Nature*, vol. 435, 1079-82.

56. A. Drescher and G.J. De Jong (1972). "Photoelastic Verification of a Mechanical Model for the Flow of a Granular Material," *J. Mech. Phys. Solids*, vol. 20, 337-351.

57. D. Mueth, H. Jaeger and S. Nagel (1998). "Force Distribution in Granular Medium," *Physical Review E*, vol. 57, no. 3, pp. 3164-9.

58. S. Yang, W. Huang, and Y. Tai. (2005). "Variation of Resilient Modulus with Soil Suction for Compacted Subgrade Soils," *Transportation Research Record*, No. 1913, 99–106.

59. K.M. Hill, B. Yohannes and L. Khazanovich (2008). "Toward a Unified Mechanistic Approach for Modeling Tests of Unbound Materials," Transportation Research Board, 87th Annual Meeting, Washington D.C.

60. K.M. Hill, B. Yohannes, and L. Khazanovich "A Unified Mechanistic Approach for Modeling Tests of Unbound Pavement Materials" *J. Transportation Engineering*, Submitted.

61. J. Gan and  D. Fredlund (1996). "Shear Strength Characteristics of two Saprolitic Soils," *Canadian Geotechnical Journal*, vol. 33, 595-609.

62. P. Davich, J. Labuz,  B. Guzina, A. Drescher (2004). *Small Strain and Resilient Modulus Testing of Granular Soils,* Minnesota Department of Transportation, St. Paul, Minnesota.

63. C. Medina, M. Zeghal and. U. El Shamy (2007). "A Micro-Mechanical Study of the Dynamic Response of Unsaturated Sloping Deposits," 4th International Conference on Earthquake Geotechnical Engineering, Thessaloniki, Greece.

64. S.H. Liu and D.A. Sun (2002). "Simulating the collapse of unsaturated soil by DEM," *Int. Journal for Numerical and Analytical Methods in Geomechanics*, vol. 26, 633–646.

65. K. Ho'ita, K. Takeda and K. Iinoya (1974). "The Capillary Binding Force of a Liquid Bridge," *Powder Technology*, vol.10, 231-242.

66. G. Lian, C. Thornton, and M. Adams (1993). "A Theoretical Study of the Liquid Bridge Forces between Two Rigid Spherical Bodies," *Journal of Colloid and Interface Science*, vol. 61, 138-147.

# Appendix A

# User's Manual

A final product from the work described in this report is an executable code entitled DEMP-3D (a Distinct Element Method – based simulation for Unbound Pavement Materials Test Models in 3-D). This appendix serves as a user's manual from running the executable code. The executable code may be used to simulate – in 3 dimensions – the resilient modulus (MR), the dynamic cone penetrometer (DCP) and the California Bearing Ratio (CBR) tests. This manual describes the required inputs and commands to run the executable files. The manual also contains some description of the output files that are generated during the simulation.

To run the simulations the user is required to have some computer resources. DEMP-3D runs only on computers with a Linux Operating System. As the DEM code is written in FORTRAN 90 programming language, the user needs to install Fortran 90 compiler. Intel 9.0 FORTRAN Compiler for Linux is recommended for efficient use of the DEM code. Intel 9.1, Intel 10.1 or other recent FORTRAN Compilers also work very well to run the simulations.

DEMP-3D consists of three separate executable files, one for each type of test. Each executable file is stored in its own folder in the main 'DEMP-3D' folder. The three folders contained in DEMP-3D are entitled MR_DEM, DCP_DEM and CBR_DEM. Each folder contains the executable file as well as additional files and folder that are required for the simulation of each test. The content of each folder can be classified into three main groups: the executable file, the input files and folder that, once the executable is run, store the output files (locations and velocities of the particles at each time step, interparticle forces, and other details). In general, to run a particular test simulation, the user will edit the appropriate input files for the desired conditions, run the executable code and then read the output files for the outcome.

This appendix contains instructions as to how to do this for each particular test. Many of the files and folders have common features for all simulations. The appendix will describe how to use the model for the MR test in detail and then follow with somewhat briefer descriptions of the other tests, pointing out commonalities where appropriate.

A few general instructions for running each code should be noted:

***Input files:*** Three basic input files are required for each simulation. Two of the input files, 'particle.in' and 'container_property.in', are very similar for all simulations. In addition to these two files, each simulation requires another file which is specific to that simulation. The authors of the code have tried to keep the input files as simple as possible. The user does not need to know the details of the DEM simulations, except few material properties and boundary conditions of the tests.

All the input files can be edited using any text editor. The user should take caution not to change the format of the input files. The user can change any of the values in the input parameters as needed. The user can not add additional parameters or modify the order of the input values. All the comments in any input file should be preceded by the number sign ('#'). The values of the input parameters should be placed below the 'commented-description'. The order of the input parameters in each file should not be changed. If these rules are not followed, the code may not run properly or may not run at all.

***Executable files:*** One executable file is prepared for each simulation: MR.exe, DCP.exe and CBR.exe. These executable files are run from the command prompt window. To run an executable file, it is advisable to change the current directory to the folder that contains the desired executable file. Then type './' followed by the name of the executable file to run the simulation. For example, to run the simulation for the MR test, type './MR.exe' from the MR_DEM directory as shown below.

       **[MR_DEM]$** *./MR.exe*

***Output files:*** The DEM codes output some files which contain detailed information about the particles, the interaction between the particles and the interaction between the particles and walls. These files are generated at every time intervals. As in the case of the input files, most of the output files are of the same format.

The particles' positions, velocities and rotations are stored in the 'particle.out*' files. (The '*' in the file name extension represents a ten digit number. This number indicates the sequence of the output files.) The 'particle.out*' files are located in the 'particle' folder. If this folder does not exist, the user should create a folder named 'particle' within the appropriate model test folder before running the executable file. If this folder does not exist, the executable file cannot run and error message is displayed.

The 'particle.out*' files contain information about the particles. Each line in these files represents the information about one particle. Each line is composed of 14 columns of numbers. The first column is the particle 'id number'. Each particle is identified by this 'id number' throughout the simulation. The next three columns represent the position of the particle in terms of 3-D Cartesian coordinate system: x-axis, y-axis and z-axis. Columns 5-7 are the component of the velocity of the particle in x, y and z axes. Columns 8-10 are the components of the rotational speed of the particle in the three axes. Column 11 indicates the time elapsed in the simulation. Column 12 indicates the type of particle. Type of particle is represented by an integer number. For example, 1 indicates that the particle is of the first type of particles described in the 'particle.in' input file. The last column in the 'particle.out*' files represents the radius of the particle.

The codes also output information about the forces between the particles and the particles and the walls. The files which contain the force information are stored in the 'forces' folder. Four types of files are produced to store this information. The normal forces between the particles is stored in 'Nforce.out*' files. (The '*' in the file name extension represents ten digit numbers. These numbers indicate the sequence of the out put files.) The tangential forces between the particles is stored in 'Tforce.out*' files. The normal and tangential forces between particles and walls are stored in 'NforceWall.out*' and 'TforceWall.out*' files respectively.

The format of all the force output files is similar. The files contain the 'id_number' of the two interacting objects (particle-particle or wall-particle) and the contact force and the overlap between the interacting objects. The first two columns indicate the 'id_number' of the interacting particles: 'primary' and 'secondary' objects. Columns 3-5 represent the x, y and z components of the force exerted on the 'secondary' object by the 'primary' object. The last column/columns represent the overlap between the interacting objects. In the case of the normal force files, only

the magnitude of the normal overlap is provided in the last column. For the tangential force files, the tangential overlap vector is provided in the last three columns.

Each simulation has an additional output file which is specific to that simulation. These additional output files contain the summarized results of the simulations.

## A.1    DEMP-3D: MR-DEM

Figure A.1 shows the files associated with the executable MR test.  MR.exe is the executable file.  All files ending with ".in" are input files.  Most output files will automatically be put in the "forces" and "particles" folder shown.  A summary of certain details are contained in the "strain_stress.out" file.   Before the executable file is run, the user needs to choose their parameters in the input files described presently.

### MR-DEM Input Files
*'particle.in'*

 The 'particle.in' file contains information about the particles and the initial conditions of each simulation. Figure A.2 shows 'particle.in' file from the MR simulation). The file contains the total number and the types of particles that are used in the simulation. The type of particles refers to the different properties of the particles. The size, density, modulus of elasticity, Poisson's ratio and coefficient of friction of particles are properties that are required for the simulations.  These properties should be in terms of the units that are described for each parameter.

The last part of the 'particle.in' input file specifies the initial conditions for the simulations. There are two possible conditions in which the simulations can be started. The first option is to start the simulation from preparing the specimen. If the user wants to start from this option, the number sign ('#') at the beginning of 'prepare sample' should be removed and the 'already prepared sample' should be commented out. The second option is to start from 'already prepared sample'. In this case the 'prepare sample' line should be commented out and the number sign ('#') at the beginning of 'already prepared sample' should be removed. If the user wants to start from 'already prepared sample' some information about the particles is required. For example, in Figure D, the 'particle.out0000001600'is the file that contains the particles positions, velocities and rotations. The details of this type of files are described in the 'Output files' section.

In addition to the 'particle.out00000016000' input file, the user might choose to add contact force input files. In this case the 'no force files' line should be commented out and the number sign ('#') at the beginning of the 'force files' should be removed as shown in Figure A.2

The details of the force files are described later in the Output files section.
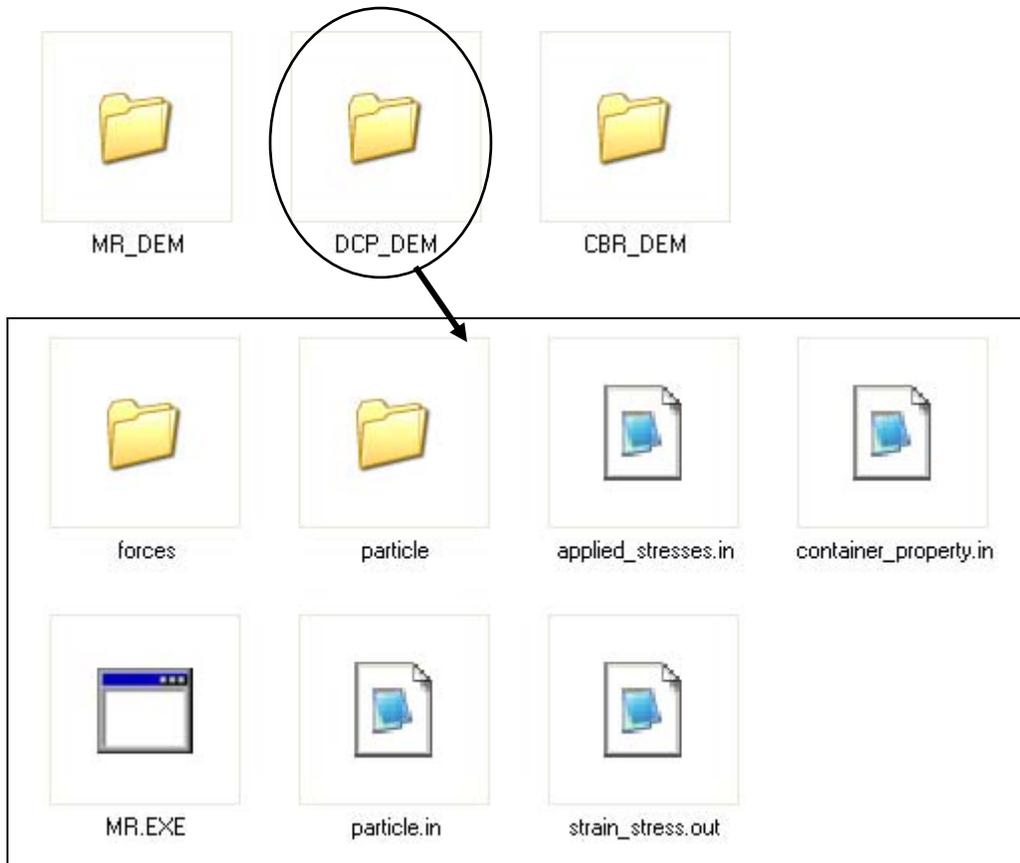
**Figure A.1:** Files and folders in the MR_DEM folder. MR.EXE file is the executable file. The 'particle.in', 'container_property.in' and the 'applied_stresses.in' files are the input files. The particle and forces folder contain the output files. The 'strain_stress.out' file is also an output file that contains the strain (%) and deviator stress (kPa) at frequent intervals.

A-4

```
# File name = 'particle.in'.
# This file is one of the input files for mr.exe.
# The file contains information about the particles and other input files.
# Take maximum caution not to corrupt file format.
# Use '#' (number sign) in the first column of a line to add any comment.

#*********************************************************

# Total number of particles in the simulation.
5000

# Number of types of particles used
4

# Size of particles (in mm)
4.75    8.0    10.0    12.0

# Density of particles (in kg/m^3)
2650.0   2650.0    2650.0    2650.0

# Percentage represented by each particle type
10.0    20.0    30.0    40.0

# Modulus of elasticity of particles(in GPa)
30.0    30.0    30.0    30.0

# Poisson's ratio
0.15    0.15    0.15    0.15

# Coefficient of friction between particles
0.5

# Choose from 'prepare sample' or 'already prepared sample'
# prepare sample
already prepared sample

# if already prepared sample add the 'particle position' file below
particle.out0000001600

# Choose from 'No force files' or 'force files'
# no force files
   force files

#if 'force files' are requried add the force files
Nforce.out0000001600
Tforce.out0000001600
Nforcewall.out0000001600
Tforcewall.out0000001600
```

**Figure A.2:** 'particle.in' input file for the MR simulation. The 'particle.in' input file contains important descriptions about the particle properties.


*'container_property.in'*

The 'container_property.in' file contains information about the properties of the container for the tests. (Figure A.3 shows the 'container_property.in' file for the MR test simulation). The size, modulus of elasticity, Poisson's ratio and the coefficient of friction of the container are the properties required for the simulations.

A-5

```
# File name = 'container_property.in'.
# This file is one of the input files for MR.exe.
# Take maximum caution not to corrupt file format.
# This file contains information about the walls.
# Use '#' (number sign) in the first column of a line to add any comment.

# *************************************************************************

# Diameter of sample (in cm)
15.0

# Modulus of elasticity of rubber membrane (GPa)
30.0

# Modulus of elasticity of rigid cover (GPa)
30.0

# Poisson's Ratio of rubber memebrane
0.15

# Poisson's Ratio of rigid cover
0.15

# Coefficient of friction between particle and rigid cover
0.5
```

**Figure A.3:** 'container.in' files for the MR simulation.


*'applied_stresses.in'*

The 'applied_stress.in' is one of the input files that are required for the MR test simulation (not shown). This file contains the magnitude of the deviator stress and the confining pressure. It also contains the number of user-required applications of the cyclic deviator stress. All may be changed by the user if desired. The MR simulation is terminated after the application of the specified number of cyclic deviator stress.

*Executable file:* As mentioned above, the executable file, MR.exe, should be run from the command prompt window; the current directory the same as that which contains MR.exe. The user should type './MR.exe'

*Output files:* In addition to the output files described in the general introduction, the MR simulation produces an additional output file entitled 'strain_stress.out'. This file will contain the strain incurred during the simulation and the magnitude of the applied deviator stress. The first column in the 'strain_stress.out' file is the strain (%) and the second column in the magnitude of the deviator stress (kPa). These values are output at every time step.

## A.2    DEMP-3D: DCP-DEM

Figure A.4 shows the files associated with the executable DCP test. DCP.exe is the executable file. All files ending with ".in" are input files. Most output files will automatically be put in the "forces" and "particles" folder shown. A summary of certain details are contained in the "dcp_penetration.out" file. Before the executable file is run, the user needs to choose their

parameters in the input files. Most of these are similar to those of the DEM_MR test. Some differences are described presently.

**DCP-DEM Input Files**
*'particle.in'*

The particle.in file for the DCP test is similar as that for the MR test with only one difference. For the DCP simulation the 'particle.in' file also contains the depth of the applied surcharge load. The depth of surcharge load should be in millimeters (mm). The surcharge is assumed to have the same material property as the particles and void fraction of 40%.

*'dcp_property.in'*

The 'dcp_property.in' is one of the input files required for the DCP test simulation. This file contains the properties of the DCP apparatus. These include the mass of the falling hammer, the mass of the DCP apparatus without the falling hammer and the dimension of the cone. This file also contains the material properties of the DCP apparatus: modulus of elasticity, the Poission's ratio and coefficient of contact friction. The numbers of hammer drops are also indicated in this file.
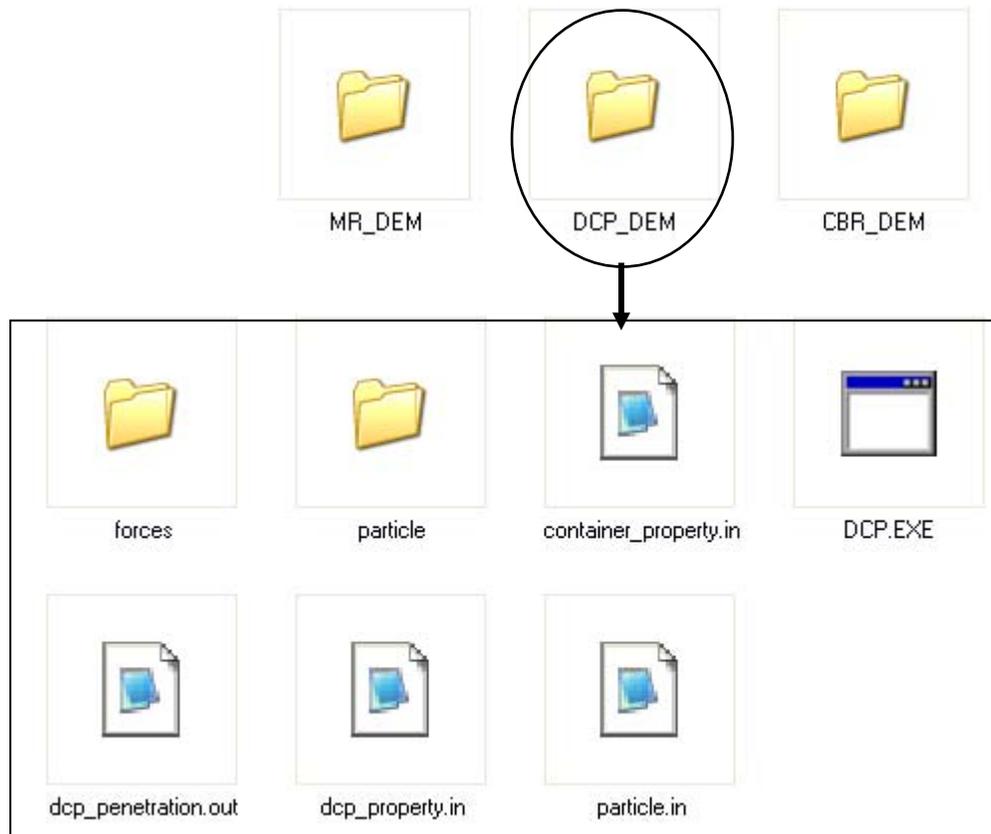
**Figure A.4:** Files and folders in the DCP_DEM folder. DCP.EXE file is the executable file. The 'particle.in', 'container_property.in' and the 'dcp_property.in' files are the input files. The particle and forces folder contain the output files. The 'dcp_penetration.out' file is also an output file that contains the time elapsed (s) in the simulation and the amount of penetration of the DCP (mm).

*'container property.in'*

The 'container_property.in' file for the DCP simulation is almost the same as that of the MR simulation (Figure A.5). But in the case of the DCP simulation the walls are all rigid: there is no rubber membrane.

```
# File name = 'conatiner_property.in'.
# This file is one of the input files for dcp.exe.
# This file contains information about the walls.
# Take maximum caution not to corrupt file format.
# use '#' (number sign) in the first column of a line to add any comment.

# ******************************************************************

# Diameter of sample (in cm)
15.0

# Modulus of elasticity of wall material(GPa)
30.0

# Poisson's Ratio of wall material
0.15
```

**Figure A.5:** *'container_property.in'* input file to the DCP simulation.


***Executable file:*** As mentioned above, the executable file, DCP.exe, should be run from the command prompt window; the current directory the same as that which contains DCP.exe. The user should type './DCP.exe'

***Output files:*** In addition to the output files described in the general introduction, the DCP simulation produces an additional output file entitled 'dcp_penetration.out' file which contains the position of the tip of the DCP apparatus with respect to the elapsed time. The first column in the 'dcp_penetration.out' is the time elapsed (s) and the second column is the depth of penetration of the DCP (mm).

## A.3    DEMP-3D: CBR-DEM

Figure A-6 shows the files associated with the executable CBR test. CBR.exe is the executable file. All files ending with ".in" are input files. Most output files will automatically be put in the "forces" and "particles" folder shown. A summary of certain details are contained in the "plunger_force.out" file. Before the executable file is run, the user needs to choose their parameters in the input files. Most of these are similar to those of the DEM_MR test. Some differences are described presently.

**CBR-DEM Input Files**
*'particle.in'*

The 'particle.in' file for the CBR test is exactly similar as that for the MR test (Figure A.2)

*'plunger_property.in'*

The 'plunger_property.in' is one of the input files required for the CBR test simulation. This file contains the mass and the diameter of the plunger in the CBR simulation. The file also contains the speed of penetration of the plunger. The CBR simulation is terminated after the plunger has penetrated 15 mm into the specimen.

*'container_property.in'*

The 'container_property.in' input file for the CBR simulation is similar to that of the DCP simulation (Figure A.5), except the height of the container should be specified in the case of CBR simulation.

***Executable file:*** As mentioned above, the executable file, CBR.exe, should be run from the command prompt window; the current directory the same as that which contains CBR.exe. The user should type './CBR.exe'

***Output files:*** In addition to the output files described in the general introduction, the CBR simulations produces an additional output file entitled 'plunger_force.out' file which contains the penetration depth of the plunger and the resisting force. The first column is the penetration depth (mm) and the second column is the resisting force (kN).
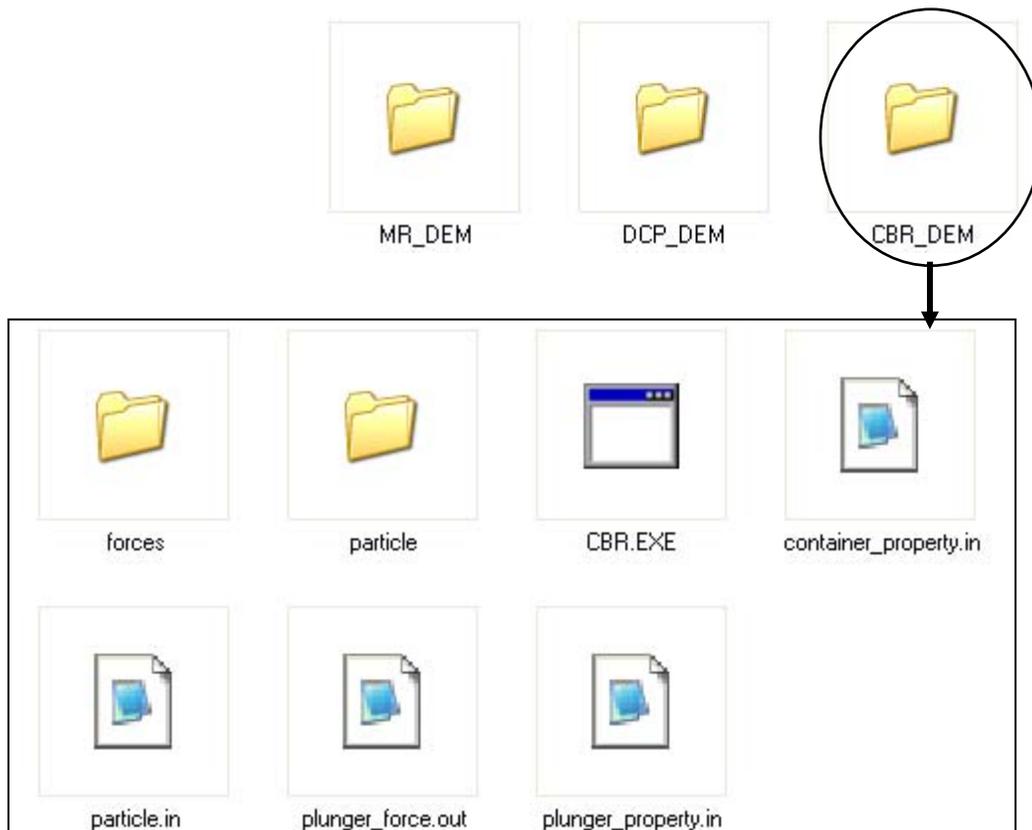


**Figure A-6**  Files and folders in the CBR_DEM folder. CBR.EXE file is the executable file. The 'particle.in', 'container_property.in' and the 'plunger_property.in' files are the input files. The particle and forces folder contain the output files. The 'plunger_force.out' file is also an out put file that contains the amount of penetration of the plunger (mm) and the measured resisting force (kN).

A-10

# Appendix B

# Modeling Unsaturated Granular Materials

The models presented in this report are designed for drained samples, which do not contain moisture. However, in real life, granular materials usually have some moisture content. The amount of water in the granular materials is highly variable and can be affected by the surrounding conditions such as groundwater level, infiltration rate and evaporation rate [58]. Based on the amount of water they contain, granular materials can be classified as saturated and unsaturated. The granular material is called saturated if all the void volume is completely filled with liquid such as water and unsaturated if some portion of the void volume is not occupied by liquid. The granular materials of the base and subgrade layers of pavements are typically unsaturated; that is, they are moist, but not completely submerged in water. Therefore it is very important to understand the behavior of granular materials which contain some moisture.

For unsaturated granular materials, the moisture causes an attraction between the particles. This attraction force is often described in terms of matric suction, essentially the negative pore pressures in the soil. The dependence of matric suction on volumetric moisture content is described qualitatively by the Soil Water Characteristic Curve (SWCC) [61] (Figure 1). The volumetric moisture content ($\omega$) is given as the ratio of the volume of water and bulk volume of the entire sample.

$$\omega(\%) = \frac{volume\ of\ water}{total\ volume\ of\ sample} x100\% \qquad \text{(B-1)}$$

The SWCC indicates the matric suction increases with decreasing moisture content. The matric suction increases the shear resistance of a soil [58, 61]. Yang et al. [58] have shown that the resilient modulus of a soil depends on the amount of moisture content. Specifically, they found that soil samples with optimum moisture content have higher resilient modulus than soil samples with moisture content higher than the optimum moisture content. The increase in resilient modulus is attributed to the soil suction generated by the presence of moisture. Gan and Fredlund [61] also observed increase in the resilient modulus with increasing matric suction. They reported that the increase in the resilient modulus was more significant for fine grained soils than for coarse grained ones. Davich et al. [12] used the DCP and Light Weight Deflectometer (LWD) tests to show that soils with higher moisture contents deform much more easily under loading than those with lower moisture contents. They hypothesized that in addition to suction, water adds a lubricating effect to the soil grains so that they slide past each other more easily. As a result, soils with large moisture contents may appear to have poor stiffness characteristics [62].
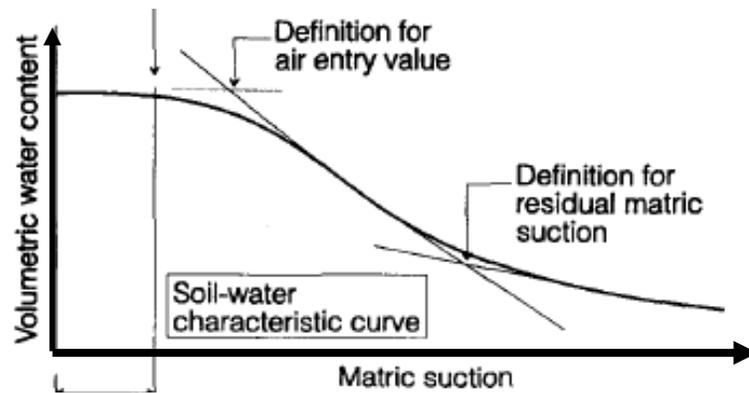
**Figure B.1:** Soil Water Characteristic Curve. The matric suction decreases with increasing water content (Gan and Fredlund [61]).

Recently, there have been a few attempts to model unsaturated granular materials with Discrete Element Models [63, 64]. In these models the moisture content is incorporated by modifying the form of the normal force (as in Equation 2.2(a)) between particles in contact by the addition of an attraction force between each pair of two particles in contact [65]. For preliminary investigations, the normal force in Equation 2.2(a) is modified by adding an attraction force between particles similar to that according to Lian et al [66] where surface tension in interparticle droplets as well as the matric suction are considered. The attraction force between the two particles exists until the separation between the particles reaches a maximum separation distance where the droplet breaks apart. The amount of liquid between two particles (liquid bridge) is determined by uniformly distributing the moisture content among all the neighboring particle pairs in the granular sample. These types of models work very well for very low moisture content where the attraction force between particles is due to the liquid bridge force.

This approach was used to compare the behaviors of granular materials at different moisture content. As an initial investigation, granular materials with moisture content ranging between 0 to 2% were modeled. Figure B.2 shows the how the slopes formed after collapse of granular materials differ according to different moisture content. The simulation was performed on granular materials that are composed of 2000 two millimeter spherical particles. Initially the granular material was put inside a box and supported by two vertical walls. During the test, the central vertical walls are removed. Figure B.2(a) shows the configuration for granular material with $\omega = 0\%$ (dry) after collapse and Figure B.2(b) shows configuration for granular material with $\omega = 0.2\%$. This simple simulation shows that the wet granular materials modeled in this way tend to form steeper slopes than dry ones as one might expect from field results. In other words, unsaturated granular materials have higher shear strength than the dry granular materials.
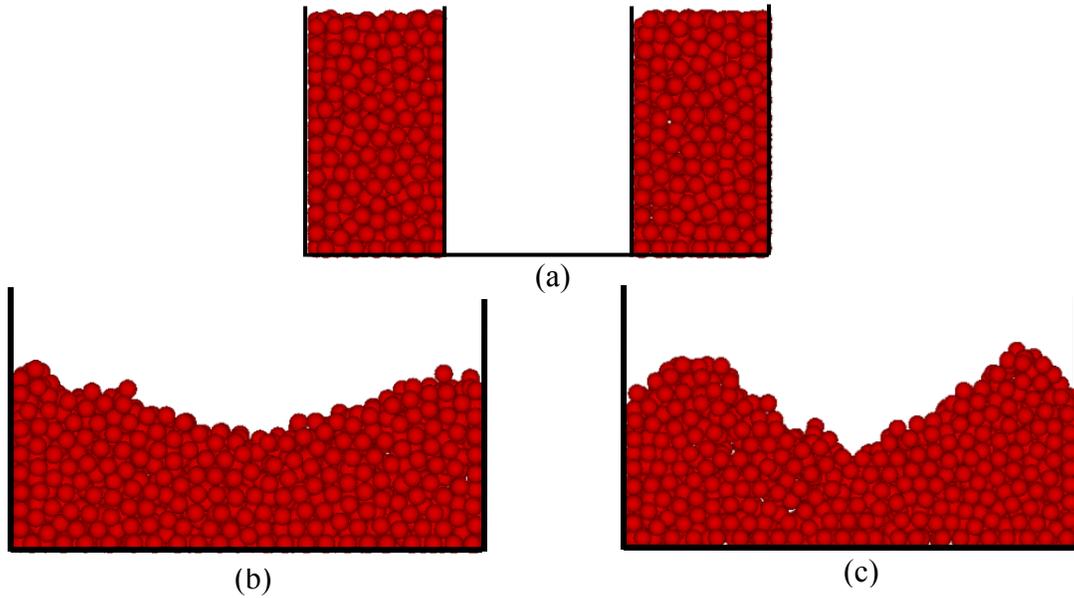
**Figure B.2:** Collapse of granular material. (a) Granular material in a rectangular container supported by vertical walls. (b) Collapse of dry granular material when the vertical supporting walls are removed. (c) Collapse of granular material with 0.2% moisture content. The slope is steeper for the wet granular material than the dry one.

Further, this model was used in preliminary investigations involving the depth of penetration of a DCP cone in granular materials that have different amount of moisture content. Figure B.3 shows depth of penetration of DCP in granular material composed of 5000 ten millimeter particles. The particles have E=29 GPa, $\rho$=2650 kg/m3, $\mu$ = 0.5 and $v$ = 0.15. Five moisture contents were used for these simulations: 0, 0.2, 0.6, 1.2 and 2%. The DCP penetration was higher for the dry granular materials. Generally, for the wet granular materials, the DCP penetration decreases with decreasing moisture content as indicated in previous studies (Figure B.1, for example). These preliminary results indicate the use of this model may be useful for understanding the effect of moisture content on the results of the tests of unbound materials described in this document.

.
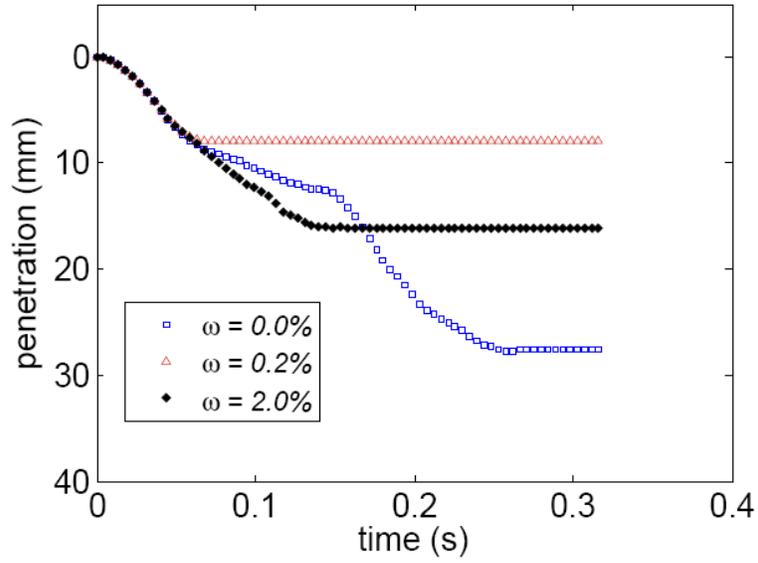
**Figure B.3:** DCP penetration for granular material with different moisture content as shown in the caption. The granular material was composed of 5000 ten millimeter particles (E=29 GPa, $\rho$=2650 kg/m3, $\mu = 0.5$ and $\nu = 0.15$).

# Appendix C

# List of Symbols

$a$     translational acceleration
$C_m$   center of mass of a cluster
$d$     size (diameter) of particles
$D$     diameter of cylindrical container
$e_n$   unit vector in the normal direction
$e_t$   unit vector in the tangential direction
$E$     modulus of elasticity of particles
$F_n$   normal component of force
$F_t$   tangential component of force
$G$     shear modulus of particles
$I$     moment of inertia
$k_n$   normal stiffness
$k_t$   tangential stiffness
$m$     mass of particle
$R$     radius of particle
$t$     time
$t_{max}$ size of time step for stable temporal integration
$v$     velocity
$\alpha$   rotational acceleration
$\gamma_n$   normal damping factor
$\gamma_t$   tangential damping factor
$\delta_n$   overlap in the normal direction
$\delta_t$   overlap in the tangential direction
$\mu$     coefficient of contact friction
$\nu$     Poisson's ratio
$\rho$     density of particles
$\tau$     torque
$\Phi$     porosity of specimen
$\omega$     rotational speed